

Spatially resolved Studies of the Leakage Current Behavior of Oxide Thin-films

DISSERTATION

zur Erlangung des akademischen Grades

doctor rerum naturalium

(Dr. rer. nat.)

im Fach Physik

eingereicht an der

Naturwissenschaftlichen Fakultät I
der
Humboldt Universität zu Berlin

von

Herrn Dipl.-Phys. Christian Dominik Martin

Präsident der Humboldt Universität zu Berlin
Prof. Dr. Jan-Hendrik Olbertz

Dekan der Mathematisch-Naturwissenschaftlichen Fakultät I
Prof. Dr. Stefan Hecht (PhD)

Gutachter: 1. Prof. Dr. Saskia F. Fischer
2. Prof. Dr. Recardo Manzke
3. Prof. Dr. Thomas Mikolajick

Eingereicht am: 13.6.2012
Tag der mündlichen Prüfung: 17.12.2012

Zusammenfassung

Im Laufe der fortwährenden Verkleinerungen integrierter Schaltungen, um *Moore's Gesetz* einzuhalten, ergab sich die Notwendigkeit der alternativen dielektrischen Materialien. Das Verständnis dieser neuen Materialien ist nicht so tief greifend wie das Verständnis für SiO_2 . Deswegen müssen diese neuen Materialien vor ihrer Integration in den Fertigungsprozess ausgiebig und gründlich untersucht werden. Während der Ablösung von HfO_2 durch die zweite Generation alternativer dielektrischer Materialien in der Fertigung von dynamic random access memory (DRAM) wie ZrO_2 haben sich weitergehende Anforderungen abgezeichnet. Da hohe Polarisierbarkeiten in diesen dielektrischen Dünnschichten erst in hoch gerichteten kristallinen Phasen auftreten, ist die Dielektrizitätskonstante der amorphen Schichten zu gering. Aufgrund der erschwerten Integrierbarkeit von epitaktischen, einkristallinen Oxidfilmen können nur poly- beziehungsweise nanokristalline Filme eingesetzt werden. Diese sind jedoch mit hohen Leckströmen behaftet.

Weil die Information in einer DRAM-Zelle als Ladung in einem Kondensator gespeichert wird ist der Verlust dieser Ladung durch Leckströme die Ursache für Informationsverluste. Somit wird die Frequenz der notwendigen Auffrischungszyklen einer DRAM-Zelle direkt durch die Leckströme bestimmt.

Notwendige Voraussetzungen für die Entwicklung jeder neuen Generation dielektrischer Materialien ist das Verständnis der zugrunde liegenden Ladungsträgertransportmechanismen und tiefe Einblicke in die strukturellen Schichteigenschaften, welche zu diesen Leckströmen führen. Das gilt nicht ausschließlich für die dielektrischen Dünnschichten in Kondensatoren sondern auch für alternative Gate Dielektrika in Feldeffekttransistoren. Zusätzlich zu neuen Materialien sind neue Charakterisierungswerkzeuge vonnöten, um nanokristalline Materialien mit ausreichend hohen Dielektrizitätskonstanten und vertretbaren Leckströmen zu entwickeln. Leitfähigkeitsrasterkraftmikroskopie (CAFM) ist eine solche Methode. CAFM ist eine Rastersondenmethode, die nicht nur wichtige strukturelle Informationen der Dünnschichten sammelt sondern diese auch mit Informationen über die lokale Leitfähigkeit dieser Nanostrukturen korreliert. Der Kern dieser Arbeit beschäftigt sich mit der

Anwendung dieser neuen Methode innerhalb eines Entwicklungszyklusses eines neuartigen dielektrischen Dünnsfilms.

In einer vergleichenden Studie wurde diese Methode benutzt um Leckströme und den Einfluss von Haftstellen in bekannten und etablierten dielektrischen Materialien zu identifizieren und zu charakterisieren. Hier wurden die Auswirkungen von unterschiedlichen Elektrodenmaterialien, in Kombination mit verschiedenen dem HfO_2 beigemischten Materialien, auf das Leckstromverhalten und bezüglich des Haftstellenverhaltens untersucht. Nach dieser Validierung von CAFM als zusätzliches Charakterisierungswerkzeug zu bereits etablierten Methoden, wurden damit die Effekte der Al_2O_3 -Beimischung in ZrO_2 untersucht. In einem ersten Schritt wurden die Auswirkungen der Beimischung von 20% Al_2O_3 in ZrO_2 durch Co-verdampfung mittels Molekularstrahlabscheidung bei hohen Temperaturen untersucht. In diesen Schichten bilden sich während der Abscheidung Kristallite, die von ihrem Nukleationszentren bis an die Oberflächen in einer ansonsten amorphen Matrix, wachsen. Mittels makroskopischer Strom-Spannungs Spektroskopie wurden an diesen Dünnsfilmen hohe Leckströme festgestellt. CAFM zeigte, dass die Kristallite für diese Leckströme verantwortlich sind und dass das elektrische Verhalten dieser Kristallite jenem Verhalten gleicht, das Stellen in der amorphen Matrix aufweisen die vorher einen dielektrischen Zusammenbruch erfahren haben. Hierzu wurde ein Ladungsträgertransportmodell entwickelt, das eine Mischung aus haftstellenunterstütztem Tunneln und dem thermochemischen Aufbrechen von Bindungen, entlang bestehender Defektpfade, vorschlägt.

Für eine weiterführende, vergleichende Studie wurden zwei Schichtdickenserien mittels Atomic Layer Deposition (ALD) abgeschieden. Die eine Serie besteht aus ZrO_2 und die andere aus $\text{ZrO}_2/\text{Al}_2\text{O}_3/\text{ZrO}_2$ (ZAZ) Nanolaminaten. Diese Schichten sollten während der Abscheidung bei 270°C amorph bleiben. Die Kristallisation sollte erst in einem späteren Tempersschritt erfolgen. Jedoch zeigte sich bei reinem ZrO_2 eine schichtdickenabhängige Kristallisation bei Schichtdicken größer als 5 nm. Diese führte zu einer überproportional großen Kapazität für größere Schichtdicken. Eine makroskopische Leckstromanalyse zeigte keine signifikanten Einfluss der Kristallisation auf die Leckströme. Eine mesoskopische Leckstromanalyse mittels CAFM zeigte jedoch erhöhte Ströme bei dickeren und weiter auskristallisierten Filmen.

Die ausgiebige strukturelle und elektrische Untersuchung dieser Schichten ergab, dass der Einschluss von nur zwei ALD Zyklen Al_2O_3 die kubisch/tetragonale Phase des ZrO_2 destabilisiert. Dieses

unterbricht die Ausbildung von Kristalliten während der Abscheidung was wiederum zu geringeren Leckströmen führt. Dabei bleibt der Grad der Kristallisation hoch genug um eine ausreichend hohe Dielektrizitätskonstante zu erhalten. CAFM wurde als örtlich hochaufgelöste Methode zur Leckstromanalyse validiert und erfolgreich in ein Materialuntersuchungs- und Entwicklungsschema integriert. Dieses konnte dazu beigetragen wichtige Erkenntnisse über die Materialeigenschaften von ZrO_2 zu gewinnen und ZAZ-Dünnschichten so zu modifizieren, dass ihre Eignung als Dielektrikum in DRAM Kondensatoren entscheidend verbessert wurden.

Darüberhinaus wurde ein CAFM modifiziert und benutzt um das Schaltverhalten eines Siliziumnanodrahtschottkybarrierenfeleffekttransistor in Abhängigkeit der Spitzenposition zu untersuchen. Es konnte experimentell bestätigt werden dass die Schottkybarrieren den Ladungstransport in diesen Bauteilen kontrollieren. Darüber hinaus wurde ein proof-of-concept für einen unprogrammierbaren nichtflüchtigen Speicher, der auf Ladungsakkumulation und der Bandverbiegung an den Schottkybarrieren basiert, gezeigt.

Abstract

In the course of the ongoing downscaling of integrated circuits, in the pursuit of *Moore's Law*, the need for alternative dielectric materials has arisen. These new materials are not as well understood as the established SiO_2 and must be studied extensively prior to integration into the fabrication process. As HfO_2 is replaced by the second generation of alternative dielectric materials for the fabrication of dynamic random access memory (DRAM) like ZrO_2 extended requirements for these novel materials appear. These dielectric thin-films do not have a sufficiently high dielectric constant when remaining amorphous because the polarizability of a dielectric is highest in highly directional crystalline phases. Since epitaxial single crystalline oxide films are very difficult to integrate into the complex DRAM fabrication process, poly- or nanocrystalline thin-films must be used. However these films are prone to very high leakage currents.

Since the information is stored as charge on a capacitor in the DRAM cell, the loss of this charge through leakage currents is the origin of information loss. The rate of the necessary refresh cycles is directly determined by these leakage currents.

A fundamental understanding of the underlying charge carrier transport mechanisms and deep insights into structural film properties leading to such leakage currents are essential to the development of each new generation of dielectric thin-film materials not only for the DRAM application. Additionally to new materials, new characterization techniques are necessary to develop nanocrystalline materials with sufficiently high dielectric constants while at the same time maintaining reasonably low leakage currents. Conductive Atomic Force Microscopy (CAFM) is such a tool. CAFM is a scanning probe microscopy method in which not only important information about the structure of dielectric thin-films is obtained but moreover this information can be correlated with information about the local conductivity of these nano-structures. The core of this work is a study on the application of this novel method in a development cycle of dielectric thin films.

In a comparative study this method was used to identify and characterize effects like leakage currents and charge trapping in estab-

lished and well known dielectric materials. The influence of the incorporation of additional materials into HfO_2 has been studied in combination with the effect of different material stacks on charge trapping and leakage current mechanisms.

After this validation of CAFM as an additional characterization tool to tools already in use, CAFM was used to characterize the effect of the incorporation of Al_2O_3 into ZrO_2 . In first step the effects of the incorporation of 20% of Al_3O_3 into ZrO_2 thin-films through co-evaporation by molecular beam deposition (MBD) at elevated temperatures of 500°C was examined. Crystallites form during the deposition, which extend from their nucleation sites to the surface of the film, in an otherwise amorphous matrix. Macroscopic current-voltage spectroscopy showed high leakage currents at those films. CAFM studies have shown these crystallites to be responsible for these high leakage currents and that the crystallites have similar electrical properties as locations in the amorphous matrix which have been subject to soft dielectric breakdown. To explain this effect a charge carrier transport model was developed that suggests a mixture of trap assisted tunneling and thermochemical bond breakage along percolation paths consisting of pre-existing defects.

For a further comparative study two thickness series were deposited by atomic layer deposition (ALD). One consisted of ZrO_2 -films the other of $\text{ZrO}_2/\text{Al}_2\text{O}_3/\text{ZrO}_2$ (ZAZ) nanolaminates. The layers were supposed to remain amorphous during deposition at 270°C . The crystallization was intended to be induced by a post deposition annealing step. However, a thickness dependent crystallization in films thicker than 5 nm was seen for ZrO_2 . This resulted in increased capacitance for thicker layer. Macroscopic I-V measurements show no significant effect of the crystallization on the leakage current density. Mesoscopic current analysis by CAFM however, reveals increased currents for thicker, more crystalline films.

The extensive structural and electrical investigations of these films show that the inclusion of only two ALD cycles of Al_2O_3 into the center of the ZrO_2 thin-film destabilizes the cubic/tetragonal phases. This effectively interrupts the formation of crystallite grain boundaries during deposition which in turn leads to less leakage currents. At the same time, the crystallization of the thin-films is sufficient to maintain a high dielectric constant. CAFM was validated as method for leakage current measurement with a high spatial resolution and was successfully introduced into a materials characterization and optimization scheme. Using this scheme it was possible gain substantial insight on the materials properties of

ZrO₂ and to modify ZAZ thin-films to significantly improve their suitability for the application in the DRAM capacitor.

Moreover, a CAFM was modified and used to examine the switching behavior of an silicon nanowire Schottky barrier field effect transistors in dependence of the probe position. It was proven experimentally that Schottky barriers control the charge carrier transport in these devices. In addition, a proof of concept for a reprogrammable nonvolatile memory device based on charge accumulation and band bending at the Schottky barriers will be shown.

Contents

1	Introduction	3
1.1	The Metal-Insulator-Metal Capacitor for Information Storage . .	4
1.2	High-k Dielectrics for the DRAM Capacitor	5
2	Fundamentals	9
2.1	Atomic and electronic Structure	9
2.2	Charge Carrier Transport in Oxides	14
2.2.1	Thermally activated Transport	15
2.2.2	Transport by quantum mechanical tunneling	16
3	Sample Preparation and Characterization	23
3.1	Deposition of dielectric Thin-films	23
3.1.1	Molecular Beam Deposition	23
3.1.2	Sputtering	24
3.1.3	Atomic Layer Deposition	24
3.2	Post-deposition Processing	26
3.2.1	Deposition of Top Electrodes	26
3.2.2	Rapid Thermal Annealing	26
3.3	Structural Characterization	27
3.3.1	Transmission Electron Microscopy and Electron Energy Loss Spectroscopy	27
3.3.2	Scanning Electron Microscopy	31
3.3.3	X-ray Reflectivity and Grazing Incidence X-ray Diffraction	32
3.3.4	X-ray Photoelectron Spectroscopy	33
3.4	Electrical Characterization	34
3.4.1	Capacitance Measurement	34
3.4.2	Current Measurement	36
3.4.3	Polarization Measurement	36
3.4.4	Simulation of Leakage Currents	37
3.5	Summary	37
4	Experimental Setup and Validation	39
4.1	The Conductive Atomic Force Microscope	39
4.1.1	The working Principle of the Atomic Force Microscope .	39
4.1.2	The Conductive Atomic Force Microscope	43
4.1.3	Experimental Limitations and external Influences	44

4.1.4	Experimental Setup	47
4.1.5	Local I-V Curves: Electrical Probing on the Nanoscale	47
4.2	Effect of the Bottom Electrode and Defects	54
4.3	Summary	61
5	High-k Materials	63
5.1	$(\text{ZrO}_2)_{0.8}(\text{Al}_2\text{O}_3)_{0.2}$ Nanocrystallites	63
5.1.1	Sample Preparation	63
5.1.2	Structural and electrical Characterization	64
5.1.3	Nanoscaled Carrier Transport Analysis	65
5.2	Zirconium Dioxide	72
5.2.1	Sample Preparation	72
5.2.2	Structural Characterization	73
5.2.3	Macroscopic electrical Characterization	78
5.2.4	Nanoscaled Carrier Transport Analysis	84
5.3	$\text{ZrO}_2/\text{Al}_2\text{O}_3/-\text{ZrO}_2$ -stacks	88
5.3.1	Sample Preparation	88
5.3.2	Structural Characterization	88
5.3.3	Macroscopic electrical Characterization	93
5.3.4	Nanoscaled Carrier Transport Analysis	99
5.4	Simulation of Leakage Currents	102
5.5	Discussion and Conclusion	104
6	Oxide Thin-films on 3D Structures	109
6.1	Introduction	109
6.2	Sample Preparation, mesoscopic and electrical Characterization	110
6.3	Results and Discussion	111
6.4	Conclusion	116
7	Summary and Outlook	117
8	Appendix	123
	Literature	135
	Table of Acronyms	138
	Acknowledgement	145
	List of Publications	144

1 Introduction

This work will start by motivating the need for novel dielectric materials for future Dynamic Random Access Memory (DRAM) technology nodes. The fundamental physical properties of dielectric thin films will be explained. It will continue by giving an insight in the standard methods used in advanced materials characterization. A special emphasis will be put on conductive atomic force microscopy (CAFM) as a method to characterize charge carrier transport locally on a mesoscopic scale. This method will be validated on established high dielectric constant, or *high-k*, insulators and used to characterize new high-k materials. In a further step it will be shown how the results of extensive materials characterization can be used to understand the effects of different processing steps on a nano-laminate insulator materials stack. In addition, the applicability of CAFM is demonstrated on three dimensional (3D) structures, silicon nanowire Schottky barrier field effect transistors (SiNWSBFET). The CAFM is modified to examine not only the switching behavior of these devices, in dependence of the probe position, but also the effects of charge trapping in the oxide surrounding the nanowire.

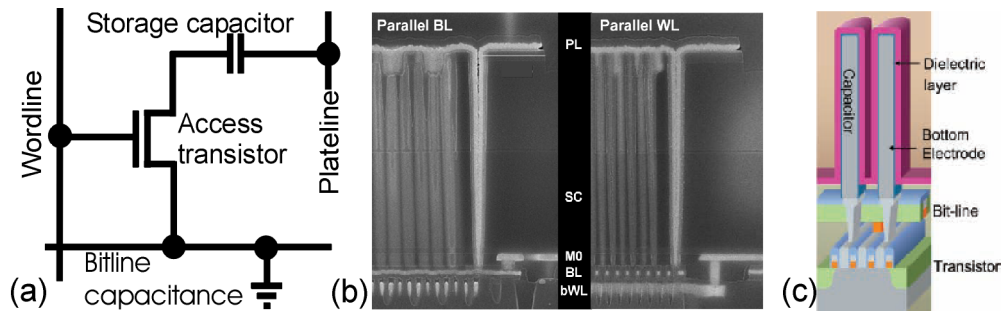


Figure 1.1: (a) Schematic of a DRAM cell after Waser [1]. (b) SEM micrograph of a buried word line (bWL) DRAM cell showing: Storage capacitor (SC), bit line (BL), Word line (WL) and plateline (PL) taken from Schlösser et al. [2] (c) Schematic of bWL DRAM cell taken from Kim et al. [3].

1.1 The Metal-Insulator-Metal Capacitor for Information Storage

The metal-insulator-metal (MIM) capacitor is the core element of the dynamic random access memory (DRAM). This is a volatile memory cell where charge is stored in a storage capacitor (SC), as depicted in Fig. 1.1. This charge represents the binary information 1 or 0. An access transistor acts as a switch connecting this capacitor to the bit line. The word line is connected to the transistor gate operating this switch. When closed a voltage is applied to the capacitor, charging it. The information is stored. After writing the switch is opened to retain the charge. In order to read out the information the switch is closed and the charge is redistributed between SC and the bit line capacitance (BC) leading to a voltage change in the bit line. This change is sensed by sense voltage amplifier. Since the read process deletes the information stored on the capacitor a re-write pulse is required to maintain the information.

After the supply voltage is cut all stored information is lost, making this memory volatile. In addition, the stored charges are lost due to leakage currents between the capacitor electrodes and within the transistor. The charge on the capacitor must be refreshed periodically. The magnitude of leakage currents determines the necessary refresh rate.

The capacity can be approximated very well by using the formula for the plate capacitor:

$$C_s = \varepsilon_0 \varepsilon_r \frac{A_S}{d} \quad (1.1)$$

Where ε_0 is the permittivity of vacuum, ε_r is the relative permittivity of the dielectric layer between the electrodes, A_S is the capacitor area and d is the distance between the electrodes and therefore the dielectric layer's physical thickness.

In the process of increasing the information density in memory products the number of transistors in an integrated circuit doubles every two years. This development is described by *Moore's Law*¹ [4]. Thus, the footprint of a single DRAM cell is continuously reduced. As 1.1 demonstrates, the capacitance of a plate capacitor shrinks with its area if the distance d between the electrodes is not reduced along with the area. As d approaches the range of only a few nanometers tunneling of charge carriers between the capacitor electrodes becomes the primary origin for information loss. In order to avoid this d can be held constant by using alternative capacitor design such as deep-trench (DT) or cup shaped capacitors increasing the capacitors area [5,6]. One kind of stack capacitor is shown in Fig. 1.1 [2]. But even in advanced 3D structures the ca-

¹Moore initially estimated the number of transistors to double every year but later corrected this to two years.

Table 1.1: The ITRS updated 2011 table of technology requirements for future technology nodes in DRAM technology [8].

Year of Production	2011	2012	2013	2014
DRAM Pitch [nm]	40	36	32	28
C_s per Cell [fF/cell]	25	20	20	20
t_{eq} (CET) [nm] at C_s	0.8	0.6	0.6	0.6
t_{phys} [nm]	8.21	7.69	7.69	7.69
Dielectric constant	40	50	50	50
$V_{Capacitor}$ [V]	1.1	1.1	1.1	1.0
J_{LC} [A/cm^2]	$1.1 \cdot 10^{-7}$	$1.5 \cdot 10^{-7}$	$1.5 \cdot 10^{-7}$	$1.3 \cdot 10^{-7}$
Deposition Temp. [$^{\circ}C$]	~ 500	~ 500	~ 500	~ 500
Anneal Temp. [$^{\circ}C$]	~ 650	~ 650	~ 650	< 650

capacitor area eventually has to decrease as the footprint is scaled to smaller and smaller areas. Another way of maintaining capacitance without increasing leakage current while reducing the area is changing the specific permittivity of the dielectric enclosed by the electrodes. This led to the replacement of the long established dielectric SiO_2 . SiO_2 was the natural choice in Si-based semiconductor industry due to its compatibility with Si. The development described above is also valid for the insulating layer separating the channel and the gate in a metal oxide field effect transistor (MOSFET). A revolutionary search for alternative gate and capacitor dielectrics has commenced as described by Bohr et al. [7]. Because of their higher dielectric permittivity ϵ_r (also referred to as κ or k) with respect to SiO_2 , these materials are called *High-k dielectrics*.

1.2 High-k Dielectrics for the DRAM Capacitor

The requirements for a alternative dielectric in the DRAM storage capacitor are in essence: A high dielectric constant and a reasonable leakage current density at the operating voltage. They can be found in the 2011 international technology roadmap for semiconductors (ITRS) an excerpt of which can be found in table 1.1 [8].

This roadmap summarizes the requirements for the DRAM capacitor of the 45 nm through 28 nm technology nodes. The capacitance requirement is 25 fF/cell until 2012, when it is reduced to 20 fF/cell. The other requirements are more variable. For the 40 nm node in 2011 the 8.21 nm thick dielectric thin-film is supposed to have a dielectric constant ϵ_r , or k-value, of 40. This means if this layer were made of SiO_2 it would have to be 0.8 nm thick to have the same capacitance at the applied voltage of $V_{Capacitor}=1.1$ V. This is defined as the capacitance equivalent thickness (CET) or t_{eq} in table 1.1. The leakage current

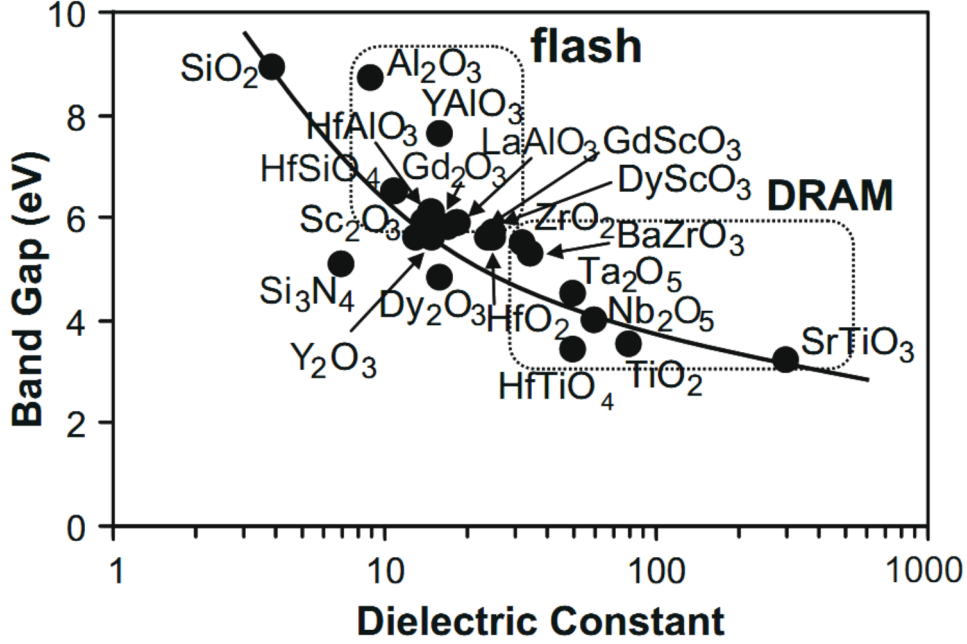


Figure 1.2: Overview of relevant candidates as a successor to SiO_2 , Band gap plotted over dielectric constant, taken from Kittl et al. [9].

density J_{LC} requirement is determined by the desired refresh rate and must not exceed $1.2 \cdot 10^{-7} \text{ A/cm}^2$ at 1.1 V in 2011. Other process parameters that must be taken into consideration are the thermal budgets for deposition and post deposition annealing. These are $\sim 500^\circ\text{C}$ and $\sim 650^\circ\text{C}$, respectively. These numerous and stringent constraints reduce the number of possible alternative dielectrics.

The key property of a dielectric thin-film for DRAM application is a sufficiently high dielectric constant. Fig. 1.2 illustrates that in order to reach the k values between 30 and 60 it is either necessary to use materials like amorphous LaAlO_3 , La_2O_3 or tetragonal ZrO_2 . The other option is to use amorphous Ti-based oxide compounds. However, Ti based oxides have a narrow band gap compared to SiO_2 or Al_2O_3 . This has implications on the leakage current density. The leakage current is highly dependent on the conduction band offset relative to the electrode materials, which in turn is dependent on the band gap. This is discussed in more detail in chapter 2.2. Lower band gap insulators require higher workfunction electrode metals. These are typically noble metals like Pt or rare metals like Ru [2, 3, 10]. Both are expensive and avoiding their use would be advantageous². An electrode metal which is already in broad use is TiN [9]. A suitable dielectric for TiN electrodes is ZrO_2 . ZrO_2 has a conduction band offset of 1.5 eV (relative to TiN), a band gap of 5.8 eV

²Quote of former Qimonda Executive regarding the use of Pt: "Oh god, we are broke already!".

and a dielectric constant of up to 47 in the a,b -plane [11, 12]. This value is only achieved in the tetragonal crystalline phase. However, the rather complex three dimensional architecture of the capacitor stack, depicted in Fig. 1.1 a) and b), requires the dielectric film to completely cover a vast array of steps. For reasons shown in chapter 3, atomic layer deposition (ALD) is a technique well suited for this purpose. Amorphous films have good step coverage but yield insufficient k-values. The compromise is a nanocrystalline film, where crystallinity is achieved by a post deposition anneal (PDA) or the deposition temperature is sufficiently high. Unfortunately, these films are prone to high leakage currents. Another compromise is necessary: A materials stack, consisting of electrodes and a dielectric, must be developed which has a sufficiently low CET and acceptable leakage currents. A powerful tool to assist with this task is CAFM, since it is able to characterize leakage currents in nanometer-scaled heterostructures with a high spatial resolution [13]. CAFM is especially well suited to identify crystallite grain boundaries or the crystallites themselves as the main contributor to leakage currents [14–16]. A significant success was achieved by depositing nanolaminate thin-films consisting of two thicker layers of ZrO_2 enclosing one much thinner layer of Al_2O_3 [10, 17–22]. These nanolaminates are called ZAZ-films.

This work employs CAFM and numerous other methods to clarify the role of crystallinity, the Al_2O_3 interlayer and crystallite grain boundaries in achieving a high dielectric constant while suppressing charge carrier transport in a comparative study of ZrO_2 - and ZAZ-films. This study demonstrates that the Al_2O_3 interlayer is not directly reducing charge carrier transport but indirectly influences charge carrier transport by stabilizing a strained monoclinic crystalline phase and suppressing the formation of nanocrystallites during deposition. In post deposition rapid thermal annealing steps this effect also suppresses the formation of large crystalline grains with grain boundaries extending throughout the entire film. Conductive atomic force microscopy demonstrates that these grain boundaries are indeed responsible for the majority of leakage currents. This work will also describe the integration of this technique into an established iterative advanced materials design scheme.

2 Fundamentals

This chapter will elucidate the fundamental issues of charge carrier transport in oxides. It will start by introducing their physical structure and continue by illustrating the electronic properties. Later, leakage current mechanisms and insulator degradation mechanisms will be introduced. It is a very brief summary of the explanations in contemporary textbooks like Waser, Huff, Sze and many more [1, 23–25]. This chapter is limited to the basic fundamental mechanisms that are essential to discuss the results obtained in chapter 4 and 5.

2.1 Atomic and electronic Structure

The oxides studied in this work are ZrO_2 , Al_2O_3 , and $(\text{ZrO}_2)_{1-x}(\text{Al}_2\text{O}_3)_x$. These are either amorphous or crystalline. The ZrO_2 thin films in this work are typically in the crystalline phases, monoclinic, cubic and/or tetragonal [26, 27]. The interatomic binding is of an ionic-covalent nature and a charge transfer from metal or transition metal ion to oxygen makes the material polarizable by electric fields. The polarization \vec{P} in an external electric field \vec{E} is ideally described by:

$$\vec{P} = \varepsilon_0 \chi_e \vec{E} = \varepsilon_0 (\varepsilon_r - 1) \vec{E} \quad (2.1)$$

where ε_0 is the dielectric permittivity of vacuum, $\varepsilon_r = 1 + \chi_e$ is the relative permittivity or dielectric constant of the material and χ_e is the electric susceptibility. The material term of the *Maxwell Equations* describes the dielectric displacement of a material as:

$$\vec{D} = \varepsilon_0 \vec{E} + \vec{P} \quad (2.2)$$

If the material is homogeneous, linear and isotropic equation 2.2 can be written as:

$$\vec{D} = \varepsilon_0 \varepsilon_r \vec{E} \quad (2.3)$$

However this only describes an ideal case. For truly amorphous films this is a reasonable approximation. For anisotropic inhomogeneous materials a more

detailed look into the microstructure is necessary as discribed by Waser et al. [1].

If the polarization is described as the vector sum of all dipole moments \vec{p} in the polarized material (polarized atoms, dipoles and ions) then the dipole moments are induced by the local electric field \vec{E}_{loc} , with N_a being the dipole density and α the polarizability of an atomic dipole.

$$\vec{P} = N_a \vec{p} = N_a \alpha \vec{E}_{loc} \quad (2.4)$$

In condensed matter, especially in inhomogeneous matter, the electrostatic interaction between local dipoles is quite high and \vec{E}_{loc} is given by:

$$\vec{E}_{loc} = \vec{E}_a + \sum \vec{E}_{dipole} \quad (2.5)$$

For the local field can be calculated. The relationship between the local polarizability and the macroscopic and measurable polarizability for cubic crystal structures is given by the *Claudius-Mossotti* equation [1, 28]:

$$\frac{N_a}{3\epsilon_0} \alpha = \frac{\epsilon_r - 1}{\epsilon_r + 2} \quad (2.6)$$

This equation is valid for ionic and electronic polarization. Ionic polarization means that in an ionic or partially ionic crystal one cationic sublattice is shifted against the anionic sublattice by an electric field. This effect is weakly temperature dependent. In electronic polarization the negatively charged electron shells are shifted against the positively charged atomic nucleus. The temperature dependence is negligible. The third form of polarization is orientation polarization. Here permanent dipoles are aligned in the electric field. This is a common effect in liquids where molecules or impurities carry a permanent dipole-moment. Another form of polarization is space charge polarization. This takes place in dielectric materials which exhibit inhomogeneities of charge carrier density.

All of the above contribute to the total polarization. Since nanocrystalline dielectric thin films are prone to carry large inhomogeneities of charge carrier density, for reasons explained later in this chapter, they are not expected to respond ideally to an external electric field. Moreover, polarization is typically of more than one type in such a film. To address this issue the complex relative dielectric permittivity is introduced:

$$\epsilon_r = \epsilon'_r + i\epsilon''_r \quad (2.7)$$

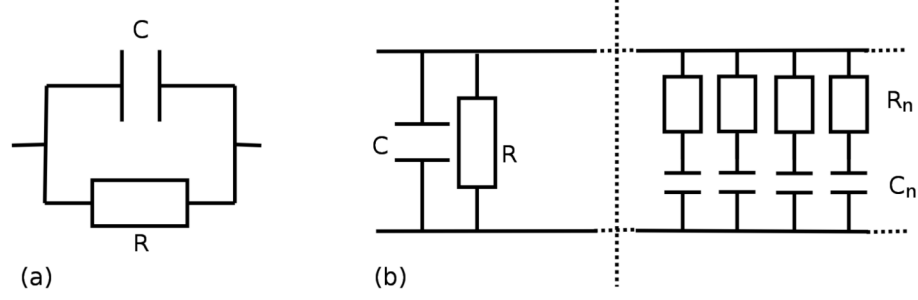


Figure 2.1: Equivalent circuit diagrams of the (a) *Debye* relaxation process and (b) the relaxation in a lossy material. R represents the leakage resistor, C the high frequency capacitor. R_n and C_n represent single relaxation elements with the relaxation time $\tau_n = R_n C_n$ after Waser [1].

The real part describes the displacement of the dipoles and the imaginary part the losses. The relationship between the two is the dielectric loss tangent [1, 23]:

$$\tan \theta := \frac{\varepsilon_r''}{\varepsilon_r'} \quad (2.8)$$

The charges responsible for space charge polarization are electrons and ions which drift within the dielectric layer according to the local electric field. These can be confined by an interface or grain boundaries but do not have to be. This makes the dielectric function dependent on the frequency of the external electric field. The dispersion relation is derived from the *Claudius-Mossotti* equation (2.6) and the solution of the equation of motion for charges species being displaced by a periodic electric field, after Waser et al. is [1]:

$$\varepsilon_r = \varepsilon'(\omega_{0+}) + \frac{\varepsilon_r'(\omega_{0-}) - \varepsilon_r'(\omega_{0+})}{1 - (\frac{\omega}{\omega_0})^2 + i\gamma\frac{\omega}{\omega_0^2}} \quad (2.9)$$

Where $\varepsilon'(\omega_{0-})$ and $\varepsilon'(\omega_{0+})$ are values of relative permittivity significantly above and below the resonance frequency ω_0 . γ is the attenuation. In addition to the frequency dependency there is a time delay of the polarization with respect to the electric field. This is called dielectric relaxation. In the case of the *Debye* relaxation process, which denotes a material with one type of dipole that has a distinct relaxation time $\tau = \frac{\gamma}{\omega_0^2}$, the displacement D and the relaxation current density j_R are, according to the equivalent circuit diagram depicted in Fig. 2.1 a):

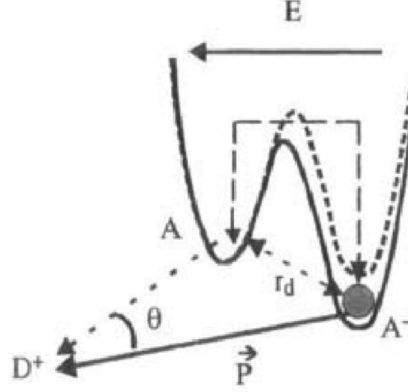


Figure 2.2: Dipole orientation between localized extrinsic or intrinsic acceptor or donor defect pairs. Taken from Schumacher et al. [29].

$$D(t) = \varepsilon_0 \varepsilon'_r(\omega_{0+}) E + \varepsilon_0 (\varepsilon'_r(\omega_{0-}) - \varepsilon'_r(\omega_{0+})) E (1 - e^{-\frac{t}{\tau}}) \quad (2.10)$$

$$j_R(t) = \dot{D} = \varepsilon_0 (\varepsilon'_r(\omega_{0-}) - \varepsilon'_r(\omega_{0+})) \frac{1}{\tau} E e^{-\frac{t}{\tau}}. \quad (2.11)$$

However, in an inhomogeneous material, like a poly- or nano-crystalline film an entire range of relaxation currents must be taken into account. In these films the conductivity is not homogeneous and the relaxation current density is calculated by superposition of exponential decays which in turn are *Debye* type processes. The resulting current density can be described by the *Curie-von-Schweidler* relation.

$$j_R(t) = \beta t^{-\alpha} + \delta(t) \quad (2.12)$$

If the distribution of the relaxation time τ is sufficiently broad the superposition of all relaxation currents $j_R(t)$ is not inversely exponentially dependent of t anymore. Here the δ -function denotes the high frequency polarization processes and α is determined by the dielectric loss tangent $\tan \theta$ and is typically $\alpha \approx 1$. β describes the charge loss of a dielectric with time. Schumacher and Waser have summarized a variety of loss mechanisms that may lead to a *Curie-von-Schweidler* behavior [29]. In addition to the one mentioned above there is also charge carrier injection by tunneling and hopping conduction, which must also be taken into account. Dissado et al. supplied a relaxation model that is based on the correlated properties of a two level system containing two types of decay mechanisms [30]. This model is depicted schematically in Fig. 2.2. The observed relaxation effect is due to a charge transfer between a charged and a neutral acceptor state. After this initial transfer an additional electron

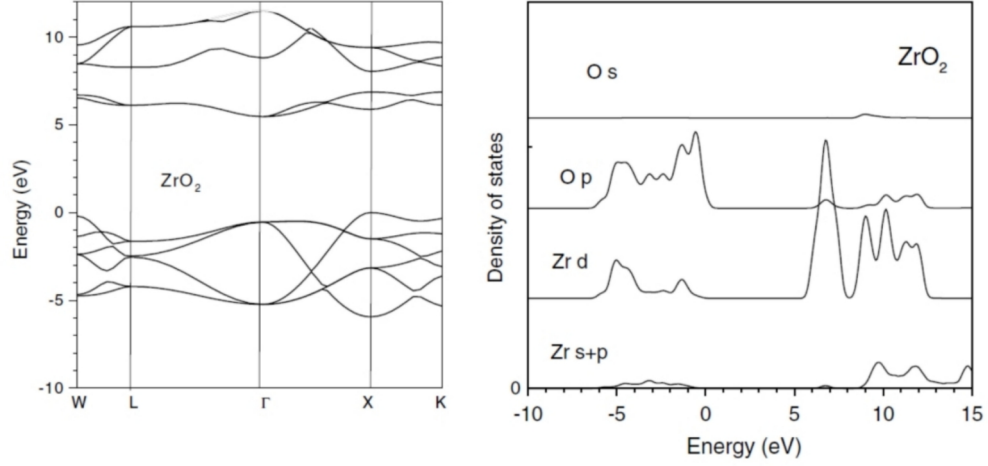


Figure 2.3: Bands and density of states of cubic ZrO_2 . Band gap is corrected to experimental value taken from Robertson [31].

is transferred to the ionized acceptor state from a third acceptor. This behavior is possible when there are additional states within the band gap. These states are due to intrinsic and extrinsic defects usually associated with grain boundaries and contamination.

In order to understand the role of defects it is necessary to elucidate the electronic properties of intrinsic crystalline ZrO_2 . ZrO_2 films are amorphous at lower temperatures. Monoclinic ZrO_2 is stable at room temperature and transforms into the tetragonal structure above 1170°C . Pies et al. report the cubic phase to be also metastable at room temperature in thin crystalline films [26]. The lattice constant of cubic ZrO_2 is 0.525 nm . In the cubic and tetragonal phase, Zr has 8 oxygen neighbors and each oxygen atom has four Zr neighbors. In the monoclinic phase each Zr atom has 7 oxygen neighbors. The transformation from cubic to tetragonal ZrO_2 occurs by displacement of oxygen atoms along the z-axis toward the 4 Zr atoms. The cubic phase can also be stabilized by a variety of ions, for example by the incorporation of Yttrium.

Robertson discusses the electronic properties of ZrO_2 in detail [31]. Fig. 2.3 depicts the band structure of cubic ZrO_2 . It has an indirect band gap of 5.8 eV (value corrected to experimental value [32]). The density of states (DOS) diagram in Fig. 2.3 elucidates how the oxygen states contribute mainly to the valence band whereas the zirconium states contribute mainly to the conduction band. The valence band is 6 eV wide and has a maximum at X formed from Op states. The conduction band minimum is a Γ_{12} state of Zr 4d orbitals.

Since this work also discusses the admixture of Al_2O_3 into ZrO_2 the electronic structure of Al_2O_3 shall also be discussed. It has a band gap of 8.8 eV and the valence band consists mainly of O p states and the conduction band mainly of Al s, p states, which are also discussed in Robertson [31].

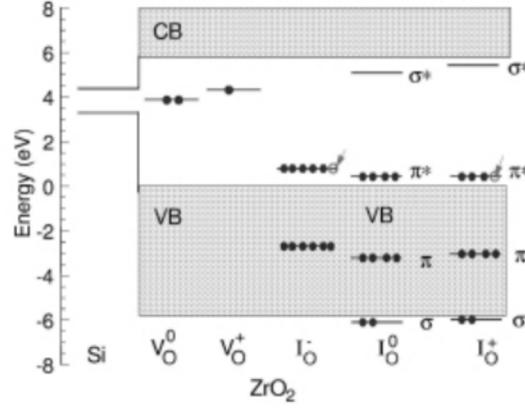


Figure 2.4: Defect states in ZrO_2 taken from Robertson [33]. Schematic molecular orbital diagram of V_O^0 the neutral oxygen vacancy, V_O^+ positive O vacancy, I_O^- negative O interstitial, I_O^0 neutral O interstitial, and I_O^+ positively charged O interstitial in ZrO_2 , showing energy levels and electron occupancies. Partially filled states are marked by arrows.

Typical defects in ZrO_2 are oxygen interstitials and oxygen vacancies [31]. Fig. 2.4 shows the molecular orbit diagram shows the energetic location and charge occupation of the oxygen interstitials and oxgen vacancies. Lucovsky et al. also describe how the energetic location of oxygen vacancies and oxygen interstitials are below the conduction band in ZrO_2 [34]. Moreover, Lucovsky et al. explore the band gap reduction due to removal of d-State degeneracies by the *Jahn-Teller* effect. These defects are not only of importance for the dielectric response of an AC-signal but they also play vital role in the charge carrier transport in oxides. The interplay of dielectric polarization in an external field, dielectric relaxation, and charge carrier transport across a dielectric thin film must be taken into consideration in the interpretation of current measurements on a dielectric material.

2.2 Charge Carrier Transport in Oxides

This section discusses the local charge carrier transport across dielectric thin films. The dielectric thin films are enclosed by either two metals or a metal and a semiconductor. These structures are called metal-insulator-metal(MIM)- or metal-insulator-semiconductor (MIS)-structures. Since the majority of structures discussed are MIM-structures this section shall concentrate on the transport mechanism across these. It is intended to be a concise summary of the transport mechanisms involved, a more detailed explanation can by found in the thesis of Blank or Jegert [35,36].

Because the MIM-Structures discussed consist of a dielectric thin film enclosed

by two metallic electrodes the charge carriers in the metal face a barrier at the metal insulator interface. The barrier height is determined by the work functions of the metal and the electron affinity and the band gap of the oxide, as depicted in Fig. 2.5 a). The basic charge carrier transport processes involved are depicted in Fig. 2.5 b).

2.2.1 Thermally activated Transport

The Schottky Emission

Schottky emission is the thermal emission of charge carriers electrons over a potential barrier of the height $e\phi_B$. The influence of the image potential on the barrier is taken into consideration. Here the effective barrier height is reduced as shown in Fig. 2.6.

The term is well known from a wide range of literature, for example Sze [25].

$$J_S = A^* T^2 e^{-\frac{e\phi_B - e\sqrt{\frac{eF}{4\pi\epsilon_0\epsilon_r}}}{kT}} \quad (2.13)$$

Where A^* is the *Richardson* constant, which contains material and elementary constants, T is the temperature and F is the electric field.

Poole-Frenkel Conduction

Pool-Frenkel is the thermionic emission out of a defect state into the conduction band of the dielectric. If an external electric field is applied, the potential bar-

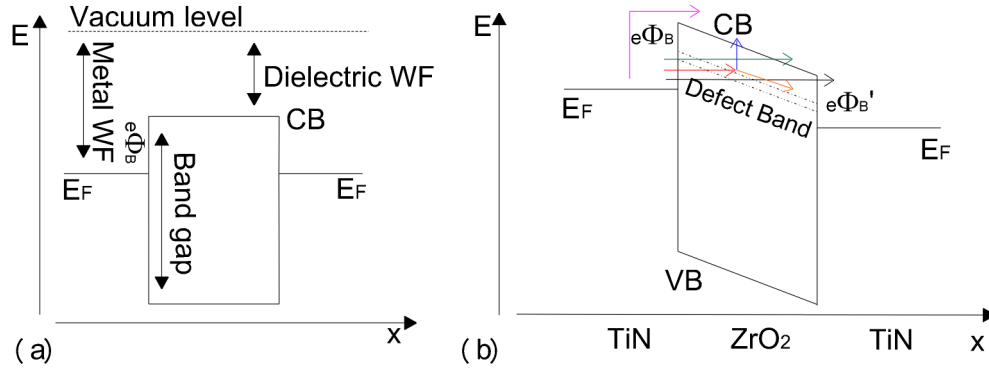


Figure 2.5: (a) Band diagram schematic of a MIM-structure. The barrier height for electron and holes is determined by the workfunctions of the metals, electron affinity and band gap of the oxide. (b) Typical charge carrier transport mechanisms in MIM structures. Black: Direct tunneling. Red: Tunneling into defect states(traps). Orange: Trap hopping. Blue: Poole-Frenkel emission from trap states. Green: Fowler-Nordheim tunneling Pink: Schottky emission.

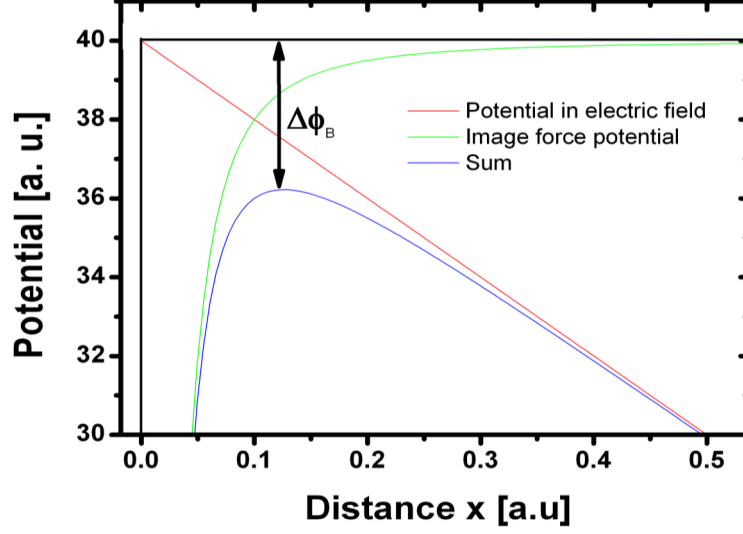


Figure 2.6: A rectangular potential barrier is denoted by thick black lines. The image force induces a "rounder" barrier, the image force potential (green). If an electric field is applied (red) this, in sum (blue), leads to an effective barrier lowering $\Delta\phi_B$.

rier of the trap state is reduced, analogous to the barrier reduction in Schottky emission. The potential of the trap state is assumed to be a *Coulomb* potential. The probability for emission out of the trap state is:

$$D_{PF} = e^{-\frac{e\phi_T - e\sqrt{\frac{eF}{4\pi\epsilon_0\epsilon_r}}}{kT}} \quad (2.14)$$

In order to obtain the current, tunneling into this trap state has to be considered. This is discussed in the following section.

2.2.2 Transport by quantum mechanical tunneling

To demonstrate direct tunneling the one dimensional tunneling model is used. This is depicted in Fig. 2.7. Here, an electron traversing a box shaped potential well has the total energy $E = \frac{p^2}{2m} + V(x)$, where p is the momentum and m electron mass. If this total energy is smaller than the barrier height $V(x)$ the electron cannot overcome the barrier. The time invariant *Schrödinger* equation describes the situation:

$$-\frac{\hbar^2}{2m} \frac{d^2}{dx^2} \Psi(x) + V(x)\Psi(x) = E\Psi(x) \quad (2.15)$$

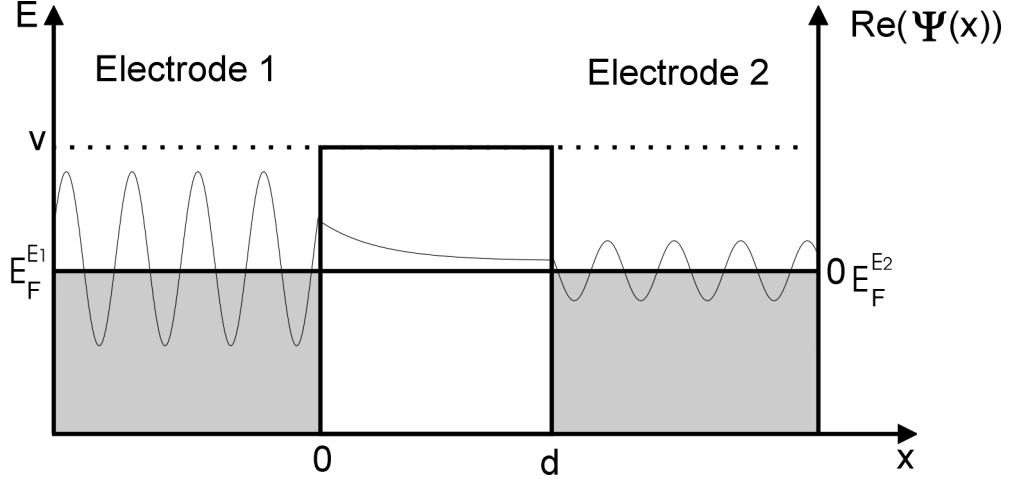


Figure 2.7: Model for one dimensional tunneling from one metallic Electrode to another via an insulating layer.

Where h is *Planck's constant* and $\hbar = \frac{h}{2\pi}$. This equation has two solutions. One for $E > V$:

$$\Psi(x) = \Psi(0)e^{\pm ikx} \quad \text{where} \quad k = \sqrt{\frac{2m(E - V)}{\hbar}} \quad \text{is the wave vector.} \quad (2.16)$$

The electron has the momentum $p = \hbar k = \sqrt{2m(E - V)}$, with is equivalent to the classical momentum. The second solution is valid for $E < V$:

$$\Psi(x) = \Psi(0)e^{-\kappa x} \quad \text{with} \quad \kappa = \frac{\sqrt{2m(V - E)}}{\hbar} \quad \text{is the decay constant.} \quad (2.17)$$

This solution is for an electron moving in the positive x -direction. The probability of an electron to be located at the location x is:

$$|\Psi(x)|^2 \propto |\Psi(0)|^2 e^{-2\kappa x} \quad (2.18)$$

Despite of not having the energy to overcome the potential barrier there is a certain probability of electrons being located inside the potential barrier. The electrons can traverse the barrier. This process is called tunneling. If we apply this on two metal electrodes being separated by an insulator this tunneling is a transition from one possible state μ in one electrode E_1 to another possible state ν in the second electrode E_2 . These states have the Fermi energies E_μ^1 and E_ν^2 , respectively. To calculate the tunneling current *Bardeen* applied quantum mechanical perturbation theory to this problem [37]. This formalism is analogous to the derivation of *Fermi's Golden Rule* [38]. The unperturbed systems is described by

$$\left(-\frac{\hbar^2}{2m} \frac{d^2}{dx^2} + U_{E_1}\right) \Psi_\mu^{E_1} = E_\mu^{E_1} \Psi_\mu^{E_1} \quad (2.19)$$

$$\left(-\frac{\hbar^2}{2m} \frac{d^2}{dx^2} + U_{E_2}\right) \Psi_\nu^{E_2} = E_\nu^{E_2} \Psi_\nu^{E_2} \quad (2.20)$$

$\Psi_\mu^{E_1}$ and $\Psi_\nu^{E_2}$ are the unperturbed states in E_1 and E_2 , respectively. The Eigenvectors of the separate systems deliver the combined system. The states of this system satisfy the Hamiltonian:

$$H = H_{E_1} + U_{E_2} = -\frac{\hbar^2}{2m} \Delta + U_{E_1} + U_{E_2} \quad (2.21)$$

The gradual adiabatic application of a potential on one electrode is equivalent to one electrode E_2 approaching the other electrode E_1 . This may be viewed as a time dependent potential.

$$U_{E_2}(t) = U_{E_2} e^{\frac{\eta t}{\hbar}} \text{ with } \eta > 0 \text{ constant} \quad (2.22)$$

U_{E_2} is constant and η small. At the time $t \rightarrow -\infty$ $\Psi_\mu^{E_1}(\vec{r})$ is an eigenstate of E_1 . If the system is perturbed the states in E_2 are filled. The tunneling current is directly proportional to the probability of transition per time, from one occupied state μ in E_1 in an empty state ν in E_2 . The time dependent wave function $\Psi_\mu(\vec{r}, t)$ is described by the time dependent *Schrödinger* equation:

$$i\hbar \frac{\partial}{\partial t} \Psi_\mu = (T + U_{E_1} + e^{\frac{\eta t}{\hbar}} U_{E_2}) \Psi_\mu \quad (2.23)$$

The ansatz for the electron wave function at the time t in the state μ is

$$\Psi(\vec{r}, t) = a_\mu(t) \Psi_\mu^{E_1}(\vec{r}) e^{-\frac{i}{\hbar} E_\mu^{E_1} t} + \sum_\nu c_\nu(t) \Psi_\nu^{E_2}(\vec{r}) e^{-\frac{i}{\hbar} E_\nu^{E_2} t} \quad (2.24)$$

with the initial conditions $a_\mu(-\infty) = 1$ und $c_\mu(-\infty) = 0$. If the ansatz is inserted into (2.23) the differential equation is:

$$\begin{aligned} i\hbar \frac{\partial}{\partial t}(t) &= \langle \Psi_\nu^{E_2} | U_{E_2} | \Psi_\mu^{E_1} \rangle e^{-\frac{i}{\hbar} (E_\mu^{E_1} - E_\nu^{E_2} + i\eta)t} \\ &+ \sum_\lambda c_\lambda(t) \langle \Psi_\nu^{E_2} | U_{E_2} | \Psi_\lambda^{E_2} \rangle e^{-\frac{i}{\hbar} (E_\lambda^{E_2} - E_\nu^{E_2})t} \end{aligned} \quad (2.25)$$

First order perturbation theory delivers the solution to the problem, with respect to the fact that all initial values are $c_\nu(-\infty) = 0$. Integration from $-\infty$ to t returns the probability for an electron, that has been in the state $\Psi_\mu^{E_1}$ at the time $t = -\infty$, to be in the state $\Psi_\nu^{E_2}$ at the time t :

$$|c_\nu(t)|^2 = \frac{e^{2\eta t/\hbar}}{(E_\mu^{E_1} - E_\nu^{E_2})^2 + \eta^2} \left| \langle \Psi_\nu^{E_2} | U_{E_2} | \Psi_\mu^{E_1} \rangle \right|^2 \quad (2.26)$$

The transition rate is the time derivative:

$$w_{\mu\nu} = \frac{2\eta}{(E_\mu^{E_1} - E_\nu^{E_2})^2 + \eta^2} e^{\frac{2\eta t}{\hbar}} \left| \langle \Psi_\nu^{E_2} | U_{E_2} | \Psi_\mu^{E_1} \rangle \right|^2 \quad (2.27)$$

As η approaches 0 the transition probability consists of the transition matrix element and a δ -function. The δ -function describes the conservation of energy. It is an elastic tunneling process.

$$w_{\mu\nu} = \frac{2\pi}{\hbar} \delta(E_\nu^{E_2} - E_\mu^{E_1}) |M_{\mu\nu}|^2 \quad (2.28)$$

$$M_{\mu\nu} = \langle \Psi_\nu^{E_2} | U_{E_2} | \Psi_\mu^{E_1} \rangle \quad (2.29)$$

This describes the transition from one state into another. Such states are numerous in both electrodes. Moreover, tunneling is only possible if the initial state is filled and the destination state is empty. In thermal equilibrium and if no bias voltage is applied the sum of electrons transmitted from $\Psi_\mu^{E_1}$ to $\Psi_\nu^{E_2}$ equals the sum of electrons transmitted from $\Psi_\nu^{E_2}$ to $\Psi_\mu^{E_1}$. The net current is zero. Now a voltage is applied and the integration over energy delivers the net tunneling current:

$$I = e \int_0^E N(\epsilon) |M(\epsilon)|^2 d\epsilon \quad (2.30)$$

Where $N(E)$ is the supply function, which is determined out of the difference in charge carrier distributions in the electrodes:

$$N(E) = \frac{4\pi m_{el}}{h^3} \int_0^\infty (f_1(\epsilon) - f_2(\epsilon)) d\epsilon \quad (2.31)$$

This can be described by the Fermi-Dirac distribution:

$$f_i(E) = \frac{1}{1 + e^{\frac{E - E_F^i}{kT}}} \quad (2.32)$$

The supply function is:

$$N(E) = \frac{4\pi m_{el}}{h^3} kT \ln \left(\frac{1 + e^{-\frac{E-E_F^1}{kT}}}{1 + e^{-\frac{E-E_F^2}{kT}}} \right) \quad (2.33)$$

Until now the tunnel matrix element in equation 2.30 was neglected. It's calculation is quite difficult, a less complex approach is the semi-classical *Wigner-Kramers-Brillouin* (WKB) approximation, which is also valid for arbitrary potential barriers $V(x)$ [35]. This is essential if the image force potential is also taken into account. Here, the matrix element can be replaced by a transmission coefficient $D(E)$.

$$I(E) = e \int_0^E N(\epsilon) D(\epsilon) d\epsilon \quad (2.34)$$

$$D(E) = e^{\left[-\frac{2\sqrt{2m_d}}{\hbar} \int_{x_2}^{x_1} \sqrt{eV_d(x) - E} dx \right]} \quad (2.35)$$

Where m_d is the electron effective mass in the dielectric and $eV_d(x)$ is the effective barrier height for the dielectric with respect to the influence of the image force potential on the barrier height (see Section 2.2.1).

Direct tunneling

Direct tunneling is tunneling where $eV < \phi'_B$, with V as the applied voltage and ϕ'_B is the height of the barrier between the destination electrode and the dielectric, see Fig. 2.5 a). Tunneling occurs between the conduction bands of the electrodes. The tunneling current is in close approximation made under the assumption of identical electrodes, $T=0$, and a trapezoidal energy barrier:

$$J_{DT} = \frac{e^3 m_e F^2}{8\pi \hbar m_d (\sqrt{e\phi_B} - \sqrt{e\phi_B - eV})^2} e^{-\frac{4\sqrt{2m_d}}{3ehF} (e\phi_B)^{\frac{3}{2}} - (e\phi_B - eV)^{\frac{3}{2}}} \quad (2.36)$$

F is the electric field in the dielectric. An analytical calculation involving the influence of image force potential and temperature is not possible anymore. For this a numerical approach is necessary.

Fowler-Nordheim tunneling

Fowler-Nordheim tunneling occurs when $eV > \phi'_B$ and electrons are transmitted from the conduction band of the metal to the conduction band of the

dielectric.

$$J_{FN} = \frac{e^2 m_e F^2}{8\pi \hbar m_d \phi_B} e^{-\frac{4\sqrt{2m_d}}{3e\hbar F} (e\phi_B)^{\frac{3}{2}}} \quad (2.37)$$

Trap assisted tunneling

Trap assisted tunneling is tunneling from one electrode into an empty defect state within the band gap and one or multiple tunneling processes from this defect state to the other electrode. The energetic positions of these defect states can be assumed to be either discrete or distributed over an energy interval [39, 40]. This work follows the assumption of Specht et al. and assumes the trap distribution to be a gaussian curve around a (trap) level below the conduction band edge [40]. Since the films are very thin a simplified model is considered in which only one trap state is involved in the transport through the entire layer. Blank calculated the tunneling rate for the two processes R_1 , tunneling from electrode into the trap state and R_2 tunneling from the trap state to the second electrode [35]. The total transmission coefficient is determined by the partial coefficients:

$$R_1 \propto (1 - f)D_1, D_1 = e^{-\frac{2\sqrt{2m_d}}{\hbar} \int_0^{x_T} \sqrt{eV_d(x) - E_x} dx} \quad (2.38)$$

$$R_1 \propto fD_2, D_2 = e^{-\frac{2\sqrt{2m_d}}{\hbar} \int_{x_T}^0 Re\sqrt{eV_d(x) - E_x} dx} \quad (2.39)$$

Where f is occupation probability of a trap state in the dielectric. For D_2 the upper boundary is the film thickness d for $V - V_{FB} < \phi_B$ and ϕ_B/F for $V - V_{FB} > \phi_B$. The flatband voltage V_{FB} is the bias voltage which equals the difference of work functions of the electrodes. The equilibrium condition $R_1 = R_2 = R$ determines the occupation probability and the total transmission coefficient can be determined with (2.38) and (2.39).

$$f = \frac{D_1}{D_1 + D_2} \Rightarrow D_{total} = \frac{D_1}{D_1 + D_2} \quad (2.40)$$

If the capture cross section is constant the total current is:

$$J_{TAT} = e\sigma_T \int_{-\infty}^{\infty} N_T(E_x) N(E_x) D_{total}(E_x) dE_x \quad (2.41)$$

The probability of trapping charge carriers is reflected in

$$P_{Trap} = \sigma_T \int_{-\infty}^{\infty} N_T(E_x) dE_x \quad (2.42)$$

A variant of this process is if the second step is not tunneling but Pool-Frenkel emission out of a defect state. In this case D_2 is replaced by (2.14) in (2.40).

3 Sample Preparation and Characterization

This chapter will introduce the techniques used to prepare and characterize the oxide thin-films discussed in this work and is intended as basis for discussion rather than a detailed description of all methods used for dielectric thin-film characterization. A complete overview of all sample preparation and characterization techniques is beyond the scope of this work. But a broad range of textbooks are available on these subjects [1, 23, 24, 41]. The deposition techniques can be separated into the physical vapor deposition (PVD) techniques, where material from solid sources is deposited and chemical vapor deposition (CVD) where precursors in the gas phase react on the substrate surface to form the deposited film and a by-product. Molecular beam deposition and sputtering are PVD techniques, atomic layer deposition (ALD), that will be discussed here, is a CVD technique. Another method to influence film properties is post deposition treatment. Rapid thermal annealing (RTA) is such a treatment.

3.1 Deposition of dielectric Thin-films

3.1.1 Molecular Beam Deposition

Molecular beam deposition (MBD) is a variation of molecular beam epitaxy (MBE) where the desired material is deposited in an amorphous or nanocrystalline phase and not epitaxially as single crystal. In MBE material is either evaporated thermally in an effusion cell or by an electron gun evaporator. This can be combined with direct gas injection. These gases can either be injected in the form of molecules or free radicals, via a radio frequency plasma cell. In order to co-evaporate from several sources these are oriented confocal to a heatable rotating substrate [23, 24]. In order to have the necessary mean free path for the evaporated molecules to reach the substrate the base pressure in the evaporation chamber must be well within the high vacuum (HV) range $10^{-3} \dots 10^{-7}$ mbar. To ensure a very high purity of the deposited films the chamber is evacuated into the ultra high vacuum (UHV) range of $10^{-7} \dots 10^{-12}$ mbar. Thus, given sufficiently pure source materials¹ deposition in UHV also assures

¹The source materials are typically of a purity much better than 99.95%

highly pure films. The heatable substrate holder typically has a range from room temperature to 1000°C. As substrate temperature is increased, so is the mobility of the adsorbate molecules on the substrate surface. Thus, the adsorbed molecules are given more energy and consequently more opportunity to find the energetically most suitable position. At sufficiently high substrate temperatures the deposited layers are grown epitaxially as one crystal. This is the typical temperature range of MBE. At lower substrate temperatures the films are deposited in an amorphous or polycrystalline phase. This is the temperature regime of MBD. By selecting a certain substrate temperature it is possible to adjust the crystallinity of the deposited film. Nominally, the higher the temperature the higher the grade of crystallinity [1, 14, 23, 42, 43]. The structure, composition and morphology of the bottom electrode also has a large influence on the structure of the oxide thin film.

3.1.2 Sputtering

Sputter deposition of oxides is achieved by the bombardment of a metal oxide target by an inert plasma, for example argon or by a metal target being bombarded by an oxidizing discharge, usually free radicals generated by a plasma. The substrate is placed inside the resulting plume to collect the sputter product on the substrate surface. For example, HfO_2 can be deposited by reactive sputtering of a hafnium metal target in an oxygen plasma or by directly sputtering a HfO_2 target with an Ar plasma [1, 23, 44]. To ensure a sufficient mean free path for the sputtered molecules sputtering must be carried out in a vacuum environment. These films can be amorphous or nanocrystalline depending on the substrate temperature during deposition and bottom electrode properties. Krause et al. have shown preferential cube-on-cube crystallization of sputtered CaTiO_3 on [011] Pt [45].

3.1.3 Atomic Layer Deposition

Atomic layer deposition is a CVD technique where the deposition process consists of a sequence of discrete self-limiting process steps. Each self-limiting step is dominant and leads to a layer saturation. Using the example of ZrO_2 the zirconium is delivered by a precursor material, for example tetrakis[ethylmethylamino]zirconium (TEMAZ). This liquid precursor is evaporated in a bubbler and transported into the reactor by an inert carrier gas. The precursor reacts with the substrate surface. Since the precursor does not react with itself (self-pyrolysis) or with ligands of itself this step is concluded when the surface is fully covered. Given the right conditions it is not possible to deposit more than one atomic layer. Thus, this process is self limiting. After this step the reactor is purged by an inert gas and the remaining ligands are flushed out. Only the Zr remains on the substrate surface. Ozone is injected

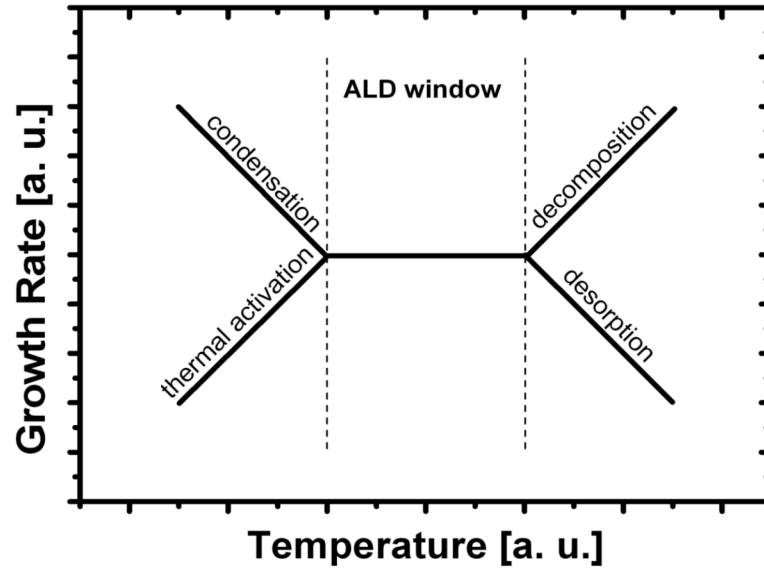


Figure 3.1: ALD-growth vs. temperature. This schematic depicts some of the different processes limiting the temperature window for a stable growth rate in ALD as described by Ritala et al. [46].

into the reactor oxidizing the metal surface. The reactor is purged again by an inert gas completing the ALD cycle. In a self limiting process the thickness of the deposited films is dependent on the number of cycles alone and not on the substrate temperature. However, the half-reactions are only truly self-limiting within a certain temperature window. At lower temperatures the growth rate is determined by thermal activation or precursor condensation before reaching a stable rate. At high temperatures the growth rate increases due to precursor decomposition or decreases due to desorption of the precursor. This limits the deposition temperature to a comparatively narrow window as shown in Fig. 3.1. Films deposited by ALD are mainly amorphous after deposition since substrate and deposition temperatures are comparatively low. Since the entire substrate is in contact with the carrier gas flux all parts of the sample surface can be reached by the precursor. "Shadow" effects are avoided. This results in a very high conformity at steps and trenches. Thus, this method is very well suited for the deposition of thin-films on three dimensional structures like deep trench or cup shaped stack capacitors.

3.2 Post-deposition Processing

3.2.1 Deposition of Top Electrodes

For macroscopic electrical characterization, capacitors were fabricated by depositing metal top electrodes (TE). These were deposited using a shadow contact mask in a purpose-built metal evaporator chamber. This is a HV chamber with two thermal evaporators and one electron-gun evaporator. Thermal evaporation is done by resistively heating a boat filled with the metal. In the electron gun evaporator an electron beam is aimed at the target material located in a water cooled crucible. The electron beam evaporates the metal locally and the metal vapor is deposited on the substrate. A shadow mask is placed between the evaporator and the sample. Metal electrode structures are deposited on the sample surface through holes in the mask. To widen the range of measurable leakage currents and to observe possible fringe and border effects, the holes in the shadow mask exhibit four different sizes [23]. A detailed description of the shadow mask used in this work is given in the appendix A Fig. 8.1. To improve the quality of the AC measurements the same process was used without an shadow mask to deposit 200 nm of Al of the backside of the samples.

3.2.2 Rapid Thermal Annealing

One way to influence the crystal structure of dielectric thin films is the substrate temperature applied during deposition. Another way is to anneal the sample after deposition, this post deposition annealing (PDA) step can be done in a regular annealing furnace. This type of treatment is suitable for PDA steps extending over a long period of time, in the order of hours. If the annealing time is within the order of minutes the heating and cooling phases play a more significant role since the ratio of annealing time to heating plus cooling time is comparably larger. In order to minimize the influence of the heating/cooling-process these must be short in respect to the actual annealing time. In a rapid thermal annealing (RTP) furnace halogen lamps are used to heat the furnace within seconds. The substrate temperature is controlled in a closed loop fed by either a thermocouple or a pyrometer. In addition, various process gases can be injected into the furnace chamber. Typical gases are nitrogen, oxygen and forming gas. A RTP furnace can be used to either passivate defects like oxygen vacancies or control the crystallographic properties of dielectric thin-films [47–49].

3.3 Structural Characterization

The following section will introduce the methods of physical characterization used in this work. It will only explain the basic underlying principles of each method and show their capabilities and limits. Since most methods are well established in research and development in semiconductor industry, more detailed explanations can be found in standard textbooks [1,23,50,51]. This work will concentrate on the principles and effects actually needed for the discussion and deductions of the following chapters.

3.3.1 Transmission Electron Microscopy and Electron Energy Loss Spectroscopy

A transmission electron microscope (TEM) is an electron microscope where an electron beam is directed through an extremely thin sample by an condenser lens system. These electron lenses are electromagnetic lenses and rely on the Lorenz force of magnetic fields on moving electrons. They can be classified as condensor, objectives and projectors. Giving the details on these systems is far beyond the scope of this work. The images acquired are the result of the interaction of the samples mesoscopic structure and the electron beam in transmission. The resolution of these microscopes is determined by the wavelength of the electrons. This is in turn given by the *de Broglie* relation:

$$\lambda_{DB} = \frac{h}{\sqrt{2meV}} \quad (3.1)$$

Where h is the Planck constant, m the electron mass, e is the electron charge and V the voltage used to accelerate the electrons. V is typically in the range of 100 kV resulting in a $\lambda \approx 3.7 \text{ pm}$. Since the mean free path of an electron in solid matter is limited the samples must be thinned in order to be sufficiently transparent for electrons. The sample thickness is reduced to 100 nm for low resolution experiments and even below 10 nm for high resolution experiments. The TEM images used in this work are cross sectional TEM images. Here the sample is either cleaved perpendicular to the sample surface and glued onto a substrate which is the thinned by electrochemical milling. Or the sample is cut out of a bulk sample by a focused ion beam (FIB) in a scanning electron microscope (SEM). This will be elucidated in section 3.3.2. A bright field TEM image is depicted in 3.2 a). Here, the electron beam is transmitted through the sample, magnified and projected on a screen. The contrast mechanism is dominated by the occlusion and absorption of electrons in the sample [1]. The electrons are scattered by the Coulomb potentials of the samples atoms. Therefore thicker regions or region where the atoms carry more electrons in their shells, being of high atomic order, appear darker than thinner regions or

regions where atoms are of lower periodic order. Another mechanism that must be taken into account is the scattering of electron waves in periodic structures like crystal lattices within the sample. The periodic atomic lattice can be described by:

$$\rho = \sum_G \rho_G e^{i\vec{G} \cdot \vec{r}} \quad (3.2)$$

\vec{G}, \vec{r} are lattice vectors and ρ is the density of scattering centers. \vec{G} must satisfy the condition

$$\vec{G} \cdot \vec{r} = 2\pi m, m = \pm 1, 2, 3 \dots \quad (3.3)$$

for all lattice vectors

$$\vec{r} = u\vec{a} + v\vec{b} + w\vec{c}; u, v, w = \pm 1, 2, 3 \dots \quad (3.4)$$

The wavelength of the electrons is given by 3.1. The Bragg condition gives the angle of diffraction as

$$\sin \phi = \frac{n\lambda}{2d} \quad (3.5)$$

where d is the distance between n lattice planes and n is the order of the reflex. In reciprocal space the distance between two lattice planes is $\frac{1}{d}$. With respect to the coordinate system of the reciprocal lattice

$$\vec{a}^* = \frac{\vec{b} \times \vec{c}}{\vec{a}(\vec{b} \times \vec{c})}; \vec{b}^* = \frac{\vec{c} \times \vec{a}}{\vec{b}(\vec{c} \times \vec{a})}; \vec{c}^* = \frac{\vec{a} \times \vec{b}}{\vec{c}(\vec{a} \times \vec{b})} \quad (3.6)$$

the reciprocal lattice vector \vec{g} is

$$\vec{g} = h\vec{a}^* + k\vec{b}^* + l\vec{c}^*. \quad (3.7)$$

For constructive interference the condition

$$\sin \alpha = \frac{\lambda|\vec{g}|}{2}, \quad (3.8)$$

must be fulfilled. By taking into account the reciprocal wave vector and the reciprocal wavelength $|\vec{k}| = \frac{a}{\lambda}$ equation 3.8 is

$$\sin \alpha = \frac{a|\vec{g}|}{2k}. \quad (3.9)$$

This means the constructive interference only takes place when:

$$|\vec{k}_0| = |\vec{k}_1| \quad (3.10)$$

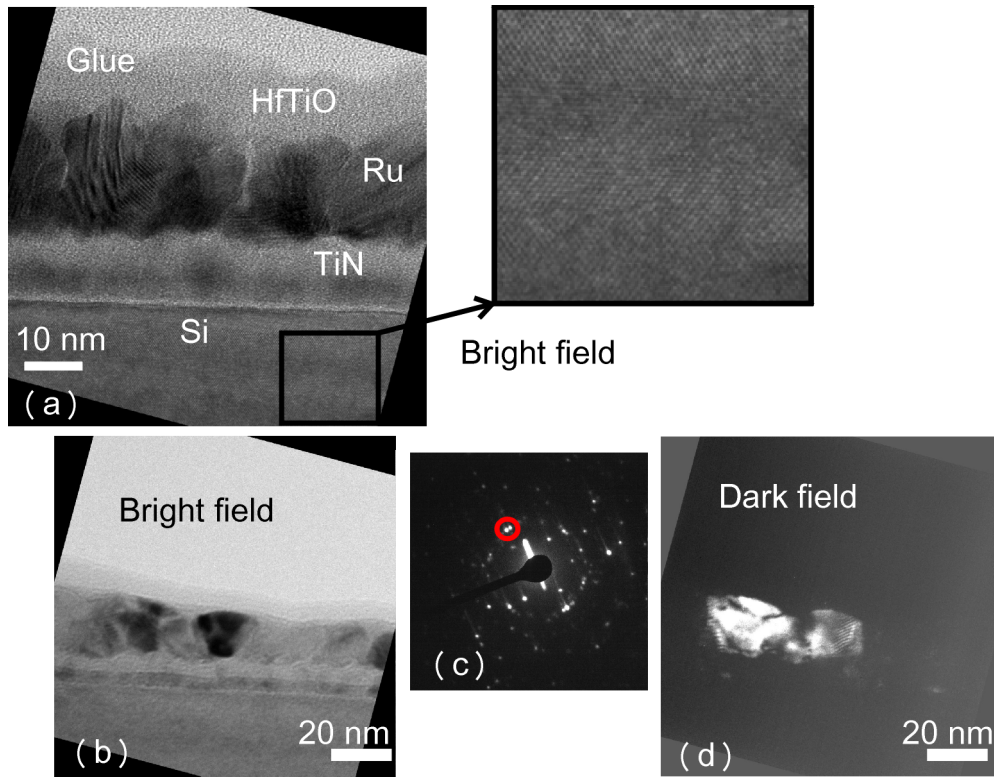


Figure 3.2: a) High resolution bright field TEM image of a TiN / Ru / HfTiO-stack. The *Moiré* patterns are visible in the Ru layer. b) Lower resolution bright field TEM image of a different area. The *Moiré* pattern in a crystallite is visible. c) Electron diffraction pattern of selected area. d) Dark field TEM image of the same area as (b). The crystallite appears bright.

where $\vec{k}_{0,1}$ is the momentum before and after scattering, respectively. This is compliant to the conservation of momentum². This means that lattice planes must satisfy $\vec{k}_0 - \vec{k}_1 = \vec{g}$ for a diffraction reflex. If the sample is polycrystalline and the electrons are scattered in several crystal lattices the diffracted waves interfere and *Moire* patterns can appear in bright field TEM images. As in Fig. 3.2 a). The amorphous HfTiO appears light gray without *Moire* patterns. The diffraction pattern of the atomic stacks of the single crystalline Si can be seen in detail in the inset.

Another modulus operandi of TEM is the dark field mode. In this mode an aperture in back focal plane is used to select or exclude reflexes, see Fig. 3.2 c). Now only regions of the sample scattering electrons to the selected reflections will appear in the image, see Fig. 3.2 d). This way TEM is a powerful tool to characterize crystalline and nanocrystalline film stacks with respect to their thickness, structure and morphology.

An additional measurement often done within a TEM setup is electron energy loss spectroscopy (EELS) or energy filtered transmission electron microscopy (EFTEM). This extends the structural analysis of TEM by a spatially resolved chemical analysis. EELS spectra can be obtained in reflection and transmission. The following description will be limited to EELS in transmission. Here the kinetic energy spectrum of the electrons transmitted through the sample is analyzed. The spatial resolution is obtained by scanning the focused electron beam across the sample via another electron optic. When electrons enter the sample the scattering processes are not limited to elastic scattering, being changes in direction. The incident beam's electrons also loose energy by inelastic scattering at the bulk's atomic shells. These losses can be caused by phonon-, plasmon- and of inner-atomic-shell excitation. Their fine structure is characteristic for the chemical elements and can be used for chemical composition analysis. To measure the correct energy loss the initial energy of the incident beam must be known. This is achieved by inserting a monochromator in the path of the electrons. These devices basically consist of two slits and an electric or magnetic field. In the following the case of the magnetic field shall be discussed. The electrons enter through one slit, are diverted by the Lorentzian force, and only electrons of one specific energy can exit the device through the other slit. The energy of the electrons exiting the device can thus be adjust by altering the strength of the magnetic field. After passing through the sample the electrons enter the analyzer. This analyzer is similar to the monochromator, it consist again of one slit, magnetic(electric) field and a position sensitive detector. After inelastic scattering the electrons are of a whole range of different kinetic energies [1]. Each energy is distracted differently in the magnetic field and therefore detected at at different location.

²For inelastic scattering: $E_0 = \hbar\omega_1 = \hbar\omega_1 = E_1$, so $\omega_0 = ck_0 = ck_1 = \omega_1$ [51]

By subtracting the energy spectrum from the initial kinetic energy a spectrum of the energy loss on a specific sample location is obtained. By scanning the sample when the detector is sensitive to a certain energy loss, associated with a certain element, a spatial distribution mapping of this element is obtained. Fig. 4.12 depicts such a map.

3.3.2 Scanning Electron Microscopy

In a scanning electron microscope (SEM) an electron beam passes a condensor lens, a deflecting coil responsible for the scanning motion of the beam and an objective lens. When entering the sample surface the electron beam is highly focused. The spatial resolution of the SEM is strongly dependent on how well the beam is focused. The electrons arriving at the samples surface interact with the sample through various processes. Some of these processes are:

- Backscattering: Electrons of the incident beam are directly backscattered, elastically and inelastically, by the bulk atomic shells of the sample. The strength of this signal is dependent on the atomic mass of the atoms in question. The energy loss is strongly dependent on the electronic properties of the sample. Therefore, the contrast is chemically sensitive.
- Excitation of secondary electrons: Incident beam electrons are absorbed by the sample and subjected to several scattering processes. They excite a series of other electrons which in turn undergo several scattering processes before they are finally emitted from the samples surface.

Backscattered and secondary electrons are typically detected by two detectors. The detector for backscattered electrons is located opposite of the sample, whereas two secondary electron detectors, are located on two sides above the sample. Since the emission of secondary electron is strongly dependent on sample morphology, incident angle and facet angle of topographical features the contrast can be improved by tilting the sample and mixing the signal of both detectors. Due to a lack of height contrast mechanism SEM images do not give hard data on sample roughness and feature height. To ensure the necessary mean free path for the electrons the microscope chamber is under ultra high vacuum.

Another tool sometimes added to an SEM is a Focused Ion Beam (FIB). Here accelerated and focused, typically Gallium, ions are used to mill out a part of the sample and weld it to an micro-manipulator for further analysis steps like TEM.

3.3.3 X-ray Reflectivity and Grazing Incidence X-ray Diffraction

Not only electron diffraction can be used for thin-films characterization. X-ray diffraction (XRD) experiments provide valuable information on the structure of thin films. In order to examine thin films the incident beam is aimed at the sample in a very small angle. This way the optical path through the thin film is maximized. This subspecies of X-ray diffraction is called grazing incidence X-ray diffraction (GI-XRD) and gives information on the crystal structure of thin-films. Another X-ray based structural analysis method that can typically be performed with the same hardware is X-ray reflectivity (XRR). XRR can be used to determine film density, film thickness, surface and interface roughness. In GI-XRD the monochromatic incident X-ray is scattered into multiple secondary waves by the atoms of a crystal lattice plane. The intensity $I(\vec{q})$ can be described by the *Born* approximation

$$I(\vec{q}) \propto \left| \int \rho(\vec{r}) e^{i\vec{q}\cdot\vec{r}} d^3r \right|^2 \quad (3.11)$$

$$\propto |FT(\rho(\vec{r}))|^2 \quad (3.12)$$

where \vec{q} is the wave vector transfer defined by the elastic scattering process:

$$\vec{q} = \vec{k}_f - \vec{k}_i \quad (3.13)$$

$$q = |\vec{q}| = 2k_{if} \sin \frac{\phi}{2} = \frac{4\pi}{\lambda} \sin \frac{\phi}{2} \quad (3.14)$$

Where $\vec{k}_{f,i}$ are the wave vector of the reflected and incident waves and ϕ is the scattering angle. The operator FT is the three dimensional *Fourier* transformation.

Since reflection takes place on all lattice planes the number of secondary waves is very high. Again the Bragg condition for construction interference for the reflected X-ray is:

$$\lambda = 2d_{hkl} \sin \theta \quad (3.15)$$

Where λ is the wavelength, d_{hkl} is the distance between lattice planes (see Equation 3.4), and θ is the angle between the reflected wave and the crystal planes. Where h,k,l are the *Miller* indices of the corresponding lattice plane. Due to the very high number of secondary waves only very small deviations of the *Bragg* condition lead to destructive interference. Each of these reflexes can be associated with a lattice plane. This makes GI-XRD a very useful tool to examine the crystalline properties of thin-films.

In XRR one Bragg reflection is examined that always exists, the-(000) re-

flection. This is identical to the transient incident beam, it does not carry much information about the thin-film except its absorption and the average electron density. With this method even amorphous layers are visible in a reflectogram. The reason for this can be found with the convolution theorem of *Fourier* transformations. If we consider a heterostructure consisting of a bulk crystal, with one electron density, covered by a thin film with another electron density the *Fourier* transformation of an infinite crystal lattice is a series of delta functions. These are the *Bragg* reflections. The *Fourier* transformation of the density function returns an oscillation whose period is dependent on the film thickness. The convolution of both is an oscillation of each *Bragg* peak. If we now consider only the (000)-peak for total reflection we have a measurable entity which is extremely sensitive to the electron density profile perpendicular to the sample surface. The intensity of the reflected signal is a function of q_z . This is the component of \vec{q} , which is perpendicular to the surface. q_z can be described by:

$$I(q_z) \propto \frac{1}{q_z^4} \left| \int \frac{d\rho(z)}{dz} e^{iq_z z} dz \right|^2 \quad (3.16)$$

The reflectivity actually depends on the change of electron density within the stack. Since this measurement integrates over a large area of the sample surface the oscillations are perturbed by film thickness variations which in turn correlate to the surface roughness [1].

3.3.4 X-ray Photoelectron Spectroscopy

X-ray photoelectron spectroscopy (XPS) is a surface analysis method used to study electronic properties such as band structures and electron binding energies. A monochromatic X-ray beam is used to illuminate the sample. The photons bearing a specific energy are absorbed by the material and can cause the emission of photoelectrons. In solids, the inelastic mean free path, at the typical energies, is limited. Thus, this method's abilities are limited to the first few nanometers beneath the surface. The kinetic energy of these photoelectrons is related to their binding energy inside the atoms and the original energy of the photons. The photoelectrons are energetically filtered in a spectrometer. Electrons can now be counted in dependence of their kinetic energy. Due to the relation between the electrons binding energy and their kinetic energy a spectrum can be acquired where the number of occurrences is displayed in respect to their binding energy [1,23]. This spectrum is specific for each element. By comparing the relative peak heights in such a spectrum this method can be used to investigate the composition and even some electronic properties like band width and band gap distances.

3.4 Electrical Characterization

The core figures of merit in dielectric thin-film characterization for the application in DRAM capacitors are leakage current and the capacitance equivalent oxide thickness. The latter is determined out of the film thickness and the capacitance. Leakage current is measured directly. However, further electrical data can be used to characterize dielectric thin-films. Dielectric breakdown voltage and polarization are also important properties of an insulating dielectric layer. The measurement of these properties will be described in this section. All electrical measurements were carried out with a semiautomatic shielded probe station. In this case a *Süss PA200* with a *ProbeShield* and *Cascade Summit 12000* with a *MicroChamber*. In such a probe station the sample is shielded from light and electric noise. The devices under test (DUT) are contacted electrically with micromanipulators. In order to measure large numbers of devices the sample can be moved in such a manner that all devices of interest can be contacted by moving the chuck, on which the sample is held, in a predefined way. The measurement hardware used in this work was a *Keithley 4200 Semiconductor Characterization System* equipped with an capacitance voltage unit (CVU) for capacitance measurements [52]. The polarization measurements were carried out with an *aixACCT TF 1000 Analyser* [53].

3.4.1 Capacitance Measurement

The capacitance C_{DUT} of a DUT is measured by applying a sine shaped alternating current (AC)-signal to the capacitor and measuring the AC current I_{AC} and the alternating voltage V_{AC} . The capacitance is calculated from the current I_{DUT} and the frequency f of the AC signal.

$$C_{DUT} = \frac{I_{DUT}}{2\pi f V_{AC}} \quad (3.17)$$

A direct current (DC) bias voltage can also be applied in addition to measure capacitance at different biases. All real capacitors are not ideal capacitors and have, to some extent, an energy loss inherent to them. This issue is addressed by considering the capacitor as an ideal capacitor with a resistor connected in parallel and the above values as vectors in a complex impedance plane illustrated in Fig. 3.3. The complex admittance describes the parallel combination of capacitance and conductance. The conductance being the origin of the energy loss. The angle Θ between the components is the phase angle between the AC signal and the admittance. However, the complementary angle $\theta = 90^\circ - \Theta$ is of more interest. This angle describes relative lossiness of the parallel combination of C_P and G_P . Moreover, $D = \tan\theta = \frac{\epsilon''}{\epsilon'} = \frac{1}{G_P C_P}$ is a direct measure for the lossiness of a capacitor and is called the dissipation factor D. It is

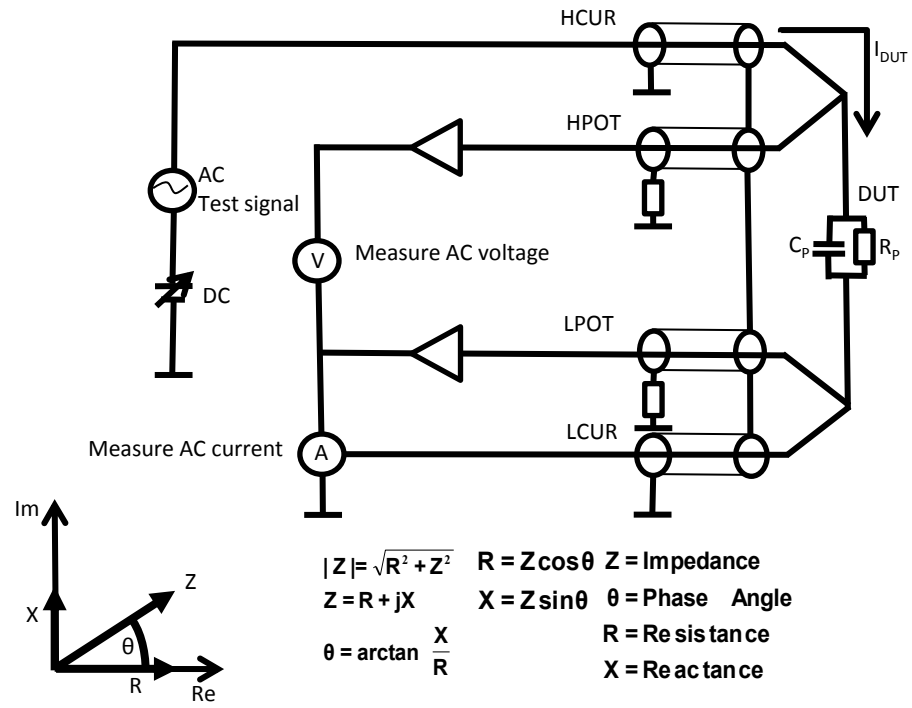


Figure 3.3: Simplified capacitance measurement setup [52] and parallel measurement model. Complex impedance plane for the impedance Z .

the relationship between the imaginary and real part of the dielectric constant ϵ . By measuring capacitance and dissipation over a range of DC bias voltages the dielectric properties and qualities of the DUT can be determined. If D is not sufficiently low the capacitance measurement is unreliable. C_{DUT} and D are measured in such a manner that after each voltage step the measurement routine has a delay before the AC signal is applied and the actual sensing starts.

3.4.2 Current Measurement

Current measurements were performed with the aim to study the origin of the dielectric losses and to study the insulating properties of the dielectric. There is no direct way of distinguishing between the contributions of the different current mechanisms, described in chapter 2, in a direct current measurement at the capacitor electrodes. Therefore, it is also not possible to distinguish between transport and relaxation mechanisms. It is necessary to address the different mechanisms by changing external influences. One of these influences is the temperature, which can be adjusted by changing the chuck temperature of the probe station. Another way of addressing different mechanisms is changing the delay between the application of a bias voltage and the actual current measurement. Thus, separating dielectric relaxation from leakage current.

The current measurement is done with a source measure unit (SMU). This is a device capable of applying a bias voltage and measuring a current at the same time. An additional preamplifier enables this SMU to detect currents down to a noise level of 10 fA.

3.4.3 Polarization Measurement

The polarization measurements were conducted using a commercial tool. The details of operation can be found in the work of Schumacher and its manual [53,54]. This tool applies a voltage $V(t)$ to the test capacitor and measures the displacement current, including dielectric loss. The current response is measured by a virtual ground amplifier. Here the polarization P is calculated by:

$$P(t) = \frac{1}{A} \int_{t_0}^{t_1} I(t) dt \quad (3.18)$$

$I(t)$ is the current at the time t , A is the area of the capacitor.

3.4.4 Simulation of Leakage Currents

The simulation of leakage currents was carried out using a Fortran code written by Martin Städele of Qimonda AG Munich. This code self-consistently calculates the integrals in equation 2.41 for a sequential two step process:

$$J_{TAT} = e\sigma_T \int_{-\infty}^{\infty} N_T(E_x)N(E_x)\frac{D_1}{D_1 + D_2}(E_x)dE_x \quad (3.19)$$

D_1 and D_2 are taken from equations 2.38 and 2.38, respectively. If the second process is Poole-Frenkel emission D_2 is replaced by equation 2.14. This software is also capable of simulating material stacks. The parameters needed to calculate the integrals are:

- Number of dielectric layers in stack
- Workfunctions of electrode and dielectric material
- Effective mass
- Dielectric constant
- Band gap
- Film thickness
- Start and end voltage
- Trap level
- Capture cross section
- Trap distribution (discrete or gaussian curve). In case of gaussian curve:
Distribution width

3.5 Summary

All deposition techniques have their unique advantages and disadvantages. PVD techniques are advantageous when there is no precursor available. MBD has superior temperature control over sputtering and therefore high control over the deposition rate to an extent that even allows epitaxy. Sputtering does not rely on evaporating matter, the target material is ablated by a plasma. Thus, this method does not rely on a suitable vapor pressure of the deposited material. Moreover, since the target can be built in any size the machines are not subject to stringent geometrical constraints, unlike MBD. Sputtering

is already a standard process in industry. The substrates can be of virtually any size. Specifically in the logic and memory semiconductor industry the sputtering can be utilized to deposit on 300 mm wafers. Another technique already standardized in the 300 mm fabrication process is ALD. Additionally to the possibility to deposit on large substrates, ALD is also able to deposit on three dimensional structures like deep trenches or ridges, without any shadow effects ensuring high step coverage. However, ALD relies on suitable precursor materials. The development of new precursors is complex and expensive and only economically reasonable if there is sufficient industrial demand for a material. This is in turn only the case if the material properties are promising. This is why, for a screening process of novel materials it is sometimes necessary to use PVD techniques owing to a lack of a precursor. In order to manufacture materials of the desired crystalline phase deposition can be performed at elevated substrate temperatures. An alternative to deposition at high temperatures is a PDA step. A typical PDA is RTA where the sample is subjected to high temperatures for only short amounts of time and the heating and cooling rate is extremely high. Each of the numerous characterization methods alone provides already valuable information about the properties, physical and/or electrical of dielectric thin films. However, when used in combination with each other, especially if the information obtained by one method can be applied by another method to specify its results in turn, an iterative process is implemented providing a complete picture of the desired materials properties. This information can be used to iteratively modify the processing parameters elucidated in the first part of this chapter. The following chapter will describe the integration of another method, CAFM, into this materials development scheme.

4 Experimental Setup and Validation

4.1 The Conductive Atomic Force Microscope

4.1.1 The working Principle of the Atomic Force Microscope

The atomic force microscope is a subspecies of the scanning probe microscope (SPM) [55]. These all derive from the scanning tunneling microscope (STM) developed by Binnig and Rohrer in 1982, which was the first SPM [56,57]. The STM itself is, in essence, an offspring of the topografiner developed by Young in 1972 [58]. In both, the a current is measured. All of the above have one thing in common. In all instruments a surface is scanned and the a height Z of the probe head at the probe location (X,Y) is recorded. In contrast to Scanning Electron Microscopy, where the interaction of the scanning electron beam with the sample is recorded at the location (X,Y) , the height recorded in scanning probe microscopy is determined by different interactions between a mechanical probe and the sample surface. These interactions are coupled to the probe head height via the feedback loop in the microscope hardware. As the probe head is moved across the sample surface by an piezoelectric actuator in the X - Y plane the interaction of probe and sample surface is constantly measured and the output is returned to the feedback loop. Here this value is compared to a predefined setpoint and the probe height height Z is adjusted to comply with this setpoint. The movement in the Z direction is also done by a piezoelectric actuator. In most modern SPM the piezoelectric actuator is a tube manufactured out of a piezoelectric material such as polycrystalline $Pb[Zr_xTi_{1-x}]O_3$ ($0 < x < 1$). This tube is separated into three segments:

- The inner segment: Changes the tube length according to an externally applied bias voltage.
- Two opposite outer segments: Bend the tube according to an externally applied bias voltage in X -direction.
- Two opposite outer segments, perpendicular to the above segments: Bend the tube according to an externally applied bias voltage in Y -direction.

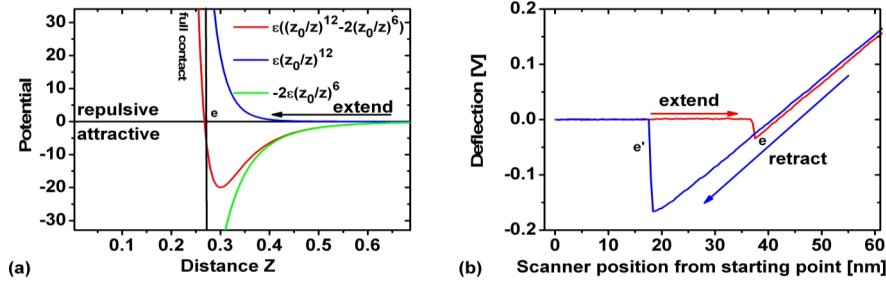


Figure 4.1: (a) Schematic Lennard-Jones-Potential (red) as the sum of repulsive (blue) and attractive forces (green). The point of equilibrium or "snap in point" is marked "e". (b) A typical deflection-distance graph. Z is the extension of the scanner piezo in Z direction. At the "snap in point", when Z exceeds 40 nm, deflection is proportional to distance. Repulsive forces dominate. When the scanner retracts the "snap off point" point e' is smaller than e . This is due to adhesive capillary forces induced by a water film on the sample surface.

As each Z value is recorded with reference to the corresponding position (X, Y) a complete map of the sample surface interaction with the probe is acquired. The offset induced by the spheric nature of the scanner movement is corrected by the measurement software.

In the case of the AFM the interaction between sample surface and probe is the sum of all forces between probe and sample surface. These are short range and long range forces. Short range forces are induced by the repulsion of ions and the overlap of electron wave functions. The latter are repulsive as a consequence of the *Pauli*-principle. Attractive short range forces may originate in covalent or metallic bonding. The range of these forces is less than 1 nm. The long range forces are *Van-der-Waals*-forces, electrostatic forces, magnetic forces and capillary forces. *Van-der-Waals*-forces are weak intermolecular forces which can be categorized into three species: Dipole-dipole interaction between permanent dipoles, dipole interaction between permanent and induced dipoles and *London*-interaction between fluctuating and induced dipoles. These forces are the contributors to the *Van-der-Waals*-force. The *Van-der-Waals*-potential can be approximated by:

$$U_{vdW} \propto \frac{-1}{Z^6} \quad (4.1)$$

Magnetic forces also act on the tip but are negligible for this work. Capillary adhesive forces induced by a liquid film on the surface are not relevant in the setpoint regime and the hard samples used throughout this work. Therefore

they are not discussed in detail. Electrostatic forces occur between probe and sample surface whenever charge carriers are present. These forces are dependent on the electrical and geometric properties of the probe and the sample surface.

The overall potential between probe and sample surface can be approximated by the Lennard-Jones-Potential as depicted in Fig. 4.1 a) [1, 59]:

$$U(Z) = \epsilon \left[-\left(\frac{z_0}{Z}\right)^{12} - 2\frac{z_0^{12}}{Z} \right] \quad (4.2)$$

It relies on the forces between sample atoms and probe atoms. Thus, the name Atomic Force Microscope. These forces are measured by measuring the deflection of a flexible cantilever on which the probe is mounted. In the initial AFM built by Binnig in 1986 this was measured by measuring the tunneling current between the cantilever and a STM tip located on top of the cantilever [55]. In most modern commercially available AFMs today the cantilever deflection is measured by sensing the position of a laser beam reflected by a cantilever onto a 2 or 4-segment optical sensor. The underlying operational principle will be discussed next. This will be done according to Szot, using a 2 segment sensor for simplicity [1].

As shown in Fig. 4.2 a laser beam is pointed on the backside of the deflected cantilever and reflected onto the sensor consisting of two adjacent photodiodes. L is the length of the cantilever. The distance between cantilever and sensor is S . When the cantilever is not displaced the beam is reflected onto both photodiodes. Both diodes, A and B, have the same irradiation $P_A = P_B = \frac{P}{2}$ (P represents the total light intensity). When the cantilever is deflected the change of irradiation Δd in the photodiodes A and B is a linear function of the displacement δ :

$$\delta \propto \Delta d = 2 \sin \Theta \cdot S = 2\Theta \cdot S = 3S \frac{\delta}{L} \quad (4.3)$$

With the approximation for small angles $\Theta = \sin \Theta$ and $\Theta = \frac{3\delta}{2L}$ from Fig. 4.2. P_A and P_B can be approximated by:

$$P_A = \frac{P}{2} \cdot \frac{(d + \Delta(d))}{2} \quad (4.4)$$

$$P_B = \frac{P}{2} \cdot \frac{(d - \Delta(d))}{2} \quad (4.5)$$

The normalized difference is:

$$\frac{P_A - P_B}{P_A + P_B} = \delta \cdot \frac{3S}{Ld} \quad (4.6)$$

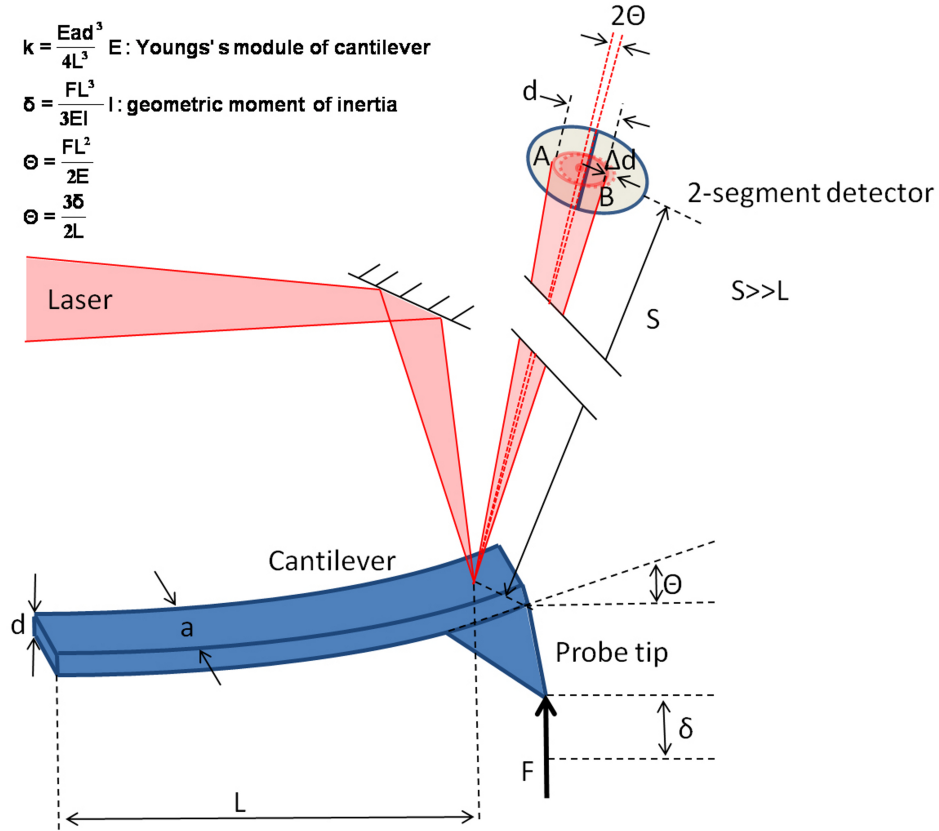


Figure 4.2: Schematic: Working principle of contact mode AFM as described by Szot [1]. As the probe tips is deflected by δ the cantilever is bent by the angle Θ . The laser beam is deflected by the angle 2Θ , or by the distance Δd on the 2-segment sensor. Note that in reality S is three orders of magnitude larger than L . The same is valid for cantilever and sensor dimensions.

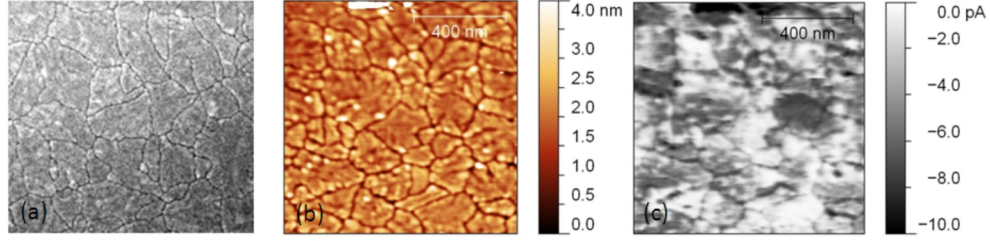


Figure 4.3: (a) SEM Micrograph of 10 nm HfSiO_2 after 1 min RTA in N_2 (b) AFM morphology map (c) Current map at -8.2 V.

The amplification of the cantilever motion through the optical lever arm method can now be understood as:

$$\frac{\Delta d}{\delta} = \frac{3S}{Ld} \quad (4.7)$$

Depending on the AFM setup and the cantilever this factor is about 1000. An AFM is able to detect changes of the the cantilever position of about 0.01 nm. The normalized difference in equation 4.6 is fed into the feedback loop, where it is compared to the setpoint. In the case of any deviation from this setpoint the Z position of the probe head is changed until the measured signal complies with the setpoint again. This *modus operandi* is called the contact mode. In this mode the force pressing the probe tip onto the sample surface is constant. When the probe head scans along the sample surface the probe head height is recorded along with the probe head position. This results in a map of the sample surface topography. Another *modus operandi* is the tapping mode [1]. However, this is not relevant for this work.

4.1.2 The Conductive Atomic Force Microscope

Conductive atomic force microscopy (CAFM) is a AFM operated in contact mode using a conductive probe tip. The latter is connected to a preamplifier. This preamplifier is a high gain transducer that converts the current into a voltage. As a bias voltage is set between sample and probe tip the current is measured relative to the probe tip position and sample bias. This way a current map is recorded along with the topography map, allowing to correlate between sample topography and charge carrier transport. Over the last decade CAFM has been developed as powerful tool for oxide thin film characterization, primarily to characterize SiO_2 but also other oxides [60–62]. Fig. 4.3 depicts an SEM Micrograph of HfSiO_2 a), and compares it to a morphology map acquired by AFM, on a different location, b) and the corresponding current map b). A network of interconnected trenches is visible in morphology and current image. These trenches can be attributed to crystallite grain boundaries, increased

charge transport takes place at these grain boundaries [15, 16, 63]

4.1.3 Experimental Limitations and external Influences

CAFM is subject to several external perturbations. These are of mechanical and electrical nature. The mechanical perturbations are either inherent low frequency building oscillations, high frequency acoustical noise or caused by temperature changes. Irregular thermal expansion of the AFM setup or parts of may result in changes of the probe position relative to the sample surface. This is called thermal drift. These can be minimized by proper system design described in the next chapter. Other sources of error are due to effects inherent to the scanning piezo. The origin of these effects lies in the fact that most piezoelectric scanner tubes behave in a non-ideal nature. There can be some remanent polarisation depending on temperature, scanner age and scanner history. This effects the piezo-movement in such a way that the elongation per Volt is not always linear or exactly the same. When movement in the X-Y plane is concerned this error has two degrees of freedom resulting in two types image distortion.

- Creep: Remnant polarization in one or two scanning dimensions after moving the designated scanning area results in a shift of the area actually scanned.
- Warp: Different polarization in the two scanning dimensions result in different distances moved in Y- and X-direction.

Other sources of error are external electromagnetic fields induced by wiring, lamps and other electrical devices. When characterizing leakage currents in dielectric thin films the figure of merit is the current density. In state of the art DRAM capacitors the current density is within one order of magnitude of $10^{-8} \frac{A}{cm^2}$ at a bias voltage of one Volt. The entity directly measured is the current. When conducting macroscopic current measurements and currents are below the inherent noise level of the measurement setup, the size of the measured device is increased and the is current density is calculated. When trying to probe leakage currents on a mesoscopic scale this scheme is not an option. Since high lateral resolution is the goal of this experiment the small contact area is also a limiting factor in terms of detecting very small currents. In order to measure these an amplifier with a gain of $10^{12} \frac{V}{A}$ is used. This amplifier must be connected to the probe-tip without interfering with its movement. This is done via a very thin flexible cable. To maintain flexibility this cable is unshielded. When an unshielded cable is connect to a sensing device with a gain of $10^{12} \frac{V}{A}$ all electromagnetic noise detected by this cable is amplified along with the desired signal resulting in a background noise within one order of magnitude of 100 fA raw mean square (RMS).

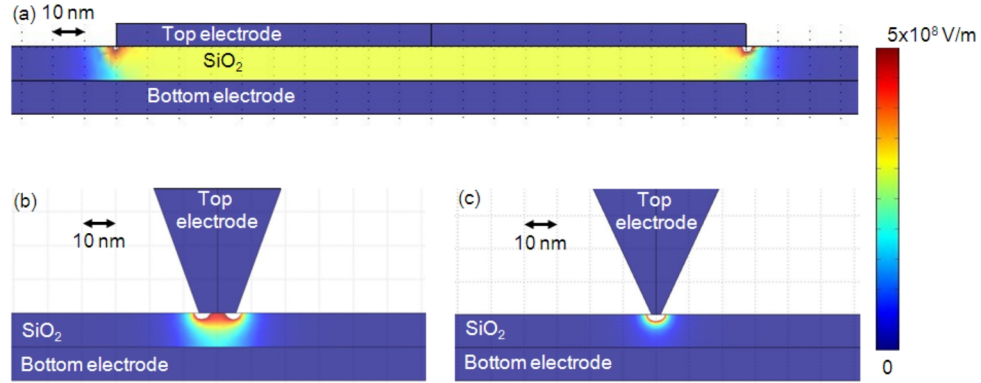


Figure 4.4: Three dimensional finite elements calculation results of test structures consisting of metal bottom electrode, a SiO_2 -film and (a) A very large pad, (b) a large tip and (c) a small tip as a top electrode. As the top electrode shrinks toward within orders of magnitude of the film thickness the fringe effects dominate the electric field.

As mentioned above, the contact area is an important factor in CAFM experiments. When the contact area is within the range of the film thickness the electric field within the dielectric film changes dramatically. In order to understand this finite element calculations were carried out. In these, three dimensional models consisting of a metal bottom electrode (Ti), a dielectric (SiO_2) and a top electrode (Ti) of various geometries were defined. The electric fields along a fine mesh were calculated. The same potential of -3 V was applied to all models. The results depicted in Fig. 4.4 a) yield that for large contact areas the field extends through the entire dielectric film for most of the contact area. Extremely high field peaks are visible at the contact area borders. However, these fringe effects are of a very low range. When the contact area is decreased in Fig. 4.4 b) these fringe effects begin to dominate the electric field geometry. Resulting in a high local electric field which barely reaches the bottom electrode. Fig. 4.4 c) shows an extreme case where the electric field consists only of fringe effects and the bottom electrode is not reached at all. These results explain the high bias voltages, compared to conventional I-V characterization, required to measure currents in CAFM. They also demonstrate how nanoscale electrical probing causes electrical stress of a highly local nature. This makes CAFM very sensitive to local defects in thin-films.

Since measurements are conducted in ambient conditions sample surface contamination is a source of error which cannot be ignored. However, the advantage of conducting these experiments in ambient conditions is the uncomplicated changing of cantilevers and samples compared to a UHV system and absence of mechanical perturbations induced by the flow of an inert gas. All thin films examined in this work are made of extremely hard and inert ma-

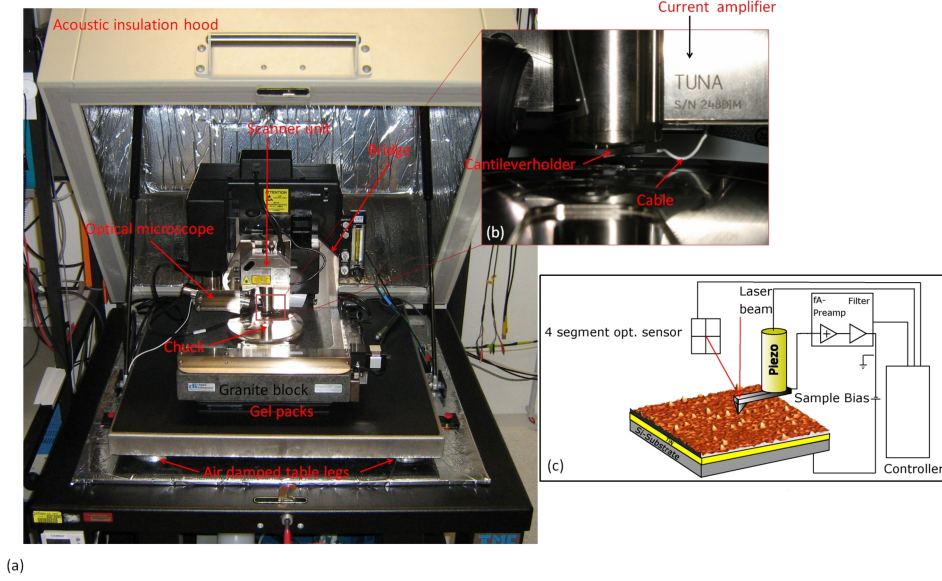


Figure 4.5: (a) The commercial Veeco Instruments CAFM setup used in this work. (b) A detailed view of the cantilever holder and the current amplifier called the TUNA module. (c) Schematic of the CAFM setup. The substrate is biased and the amplifier is grounded.

materials: TiN, HfO_2 , ZrO_2 and their compounds. This enables us to avoid macroscopic sample contamination by using a standard cleaning procedure in an ultrasonic bath with isopropanol. Moreover, the hardness of the examined materials allows operation of the AFM in the full contact regime depicted in Fig. 4.1. This alone already avoids effects induced by mesoscopic contamination to some extent. The AFM probe is simply pressing through any sample contamination. However, this behavior must be closely monitored to ensure reliable measurements. This is done by comparing the trace and retrace images for friction effects. Another method is monitoring the lateral forces inflicted on the probe tip during image acquisition. This can be achieved by scanning perpendicular to the cantilever orientation and comparing the cantilevers torsional movement. Any torsional movement of the cantilever is registered by the 4-segment sensor as lateral deflection. If the lateral signal in trace and retrace direction are opposite then this is due to lateral force eg. friction impeding the probe tip. A detailed description of Lateral Force Microscopy is beyond the scope of this work and this method is used only qualitatively in this work. Measurements show that lateral forces induced by friction through surface contaminates do not significantly effect current mapping.

4.1.4 Experimental Setup

The AFM used in this work is shown in Fig. 4.5. It is a commercially built AFM by Veeco instruments¹ It was designed as a "scanning by probe" setup in order to accommodate samples as big as 6" wafers on a vacuum chuck. This amplifier's maximum gain is $10^{12} \frac{V}{A}$. The scanner is mounted on a symmetrical bridge over the sample. The bridge is symmetrical to reduce the influence of thermal drift. In order to minimize other mechanical disturbances such as low frequency building oscillations the AFM is mounted on a heavy granite block. The heavy compact and construction has a high eigenfrequency. This makes it less sensitive to building oscillations. The granite block is decoupled by flexible gel packs from the table. The extremely heavy table in turn is decoupled from the building by air damped table legs. These are standing on "Elefant's Feet" which are fastened directly to the base plate of the laboratory building. To insulate the AFM acoustically from the environment against high frequency oscillations; a acoustic insulation hood surrounds the AFM setup. To reduce the influence of external electromagnetic fields the preamplifier is mounted right on the scanner casing. This reduces the cable length between AFM-probe and preamplifier to about 2 cm reducing the electrical noise. Since the films studied are deposited on highly n-doped silicon substrates the current measurement can be performed via the chuck through the substrate. The sample is set on a potential lower than the probe, this prevents local anodic oxidation [64]. Thus, electrons are injected from the substrate.

4.1.5 Local I-V Curves: Electrical Probing on the Nanoscale

In contrast to electrical characterization with conventional semiconductor probing equipment electrical probing on the nanoscale with a CAFM requires more care in the verification of a sufficient electrical contact between probe and sample. When conducting an experiment with a dedicated probe station comparatively large probes (contact can be down to $1 \mu m$ in diameter) held by large and heavy stabilized manipulators are used. The probes make contact to metal electrodes on the sample surface. These contacts were deposited especially for this purpose. In a CAFM a very small (approx. 15 nm tip-apex area) and conductive probe is used. The AFM was originally designed to obtain a detailed topological map of the sample surface and to measure interatomic and electromagnetic forces [55]. Unlike in probe stations used for macroscopic electrical characterization a mechanically stable electric contact for electrical characterization is not native to this setup and considerable care has to be take to achieve this.

¹Now Bruker.

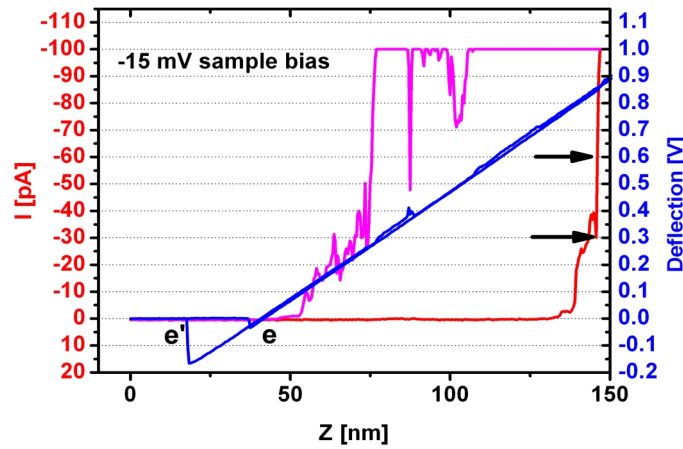


Figure 4.6: Typical combined current distance and deflection-distance spectrum taken simultaneously at 15 mV. At the "snap in point" e , when Z exceeds 40 nm, deflection gets proportional to distance. Upon positive reflection repulsive forces dominate. As Z exceeds 146 nm current is not highly dependent on deflection (force) anymore. The current amplifier limit is 100 pA. As Z is decreased again large currents are measured until $Z \approx 75$ nm. A typical setpoint is at a deflection offset of 0.3 V to 0.6 V larger than the "snap in point".

To achieve a stable and sufficiently large contact area finding the correct feedback loop setpoint is critical. On the one hand the force pressing the probe onto the sample surface must be sufficiently high to protrude through all surface contaminants, for example water. On the other hand the adhesive force must not be too high since high forces result in lower spatial morphological resolution and induce higher tip wear. Thus, decreasing tip lifetime dramatically. Force-distance and force-current spectroscopy are combined with morphology and current imaging in order to determine the optimal setpoint. This is done on chips of highly n-doped silicon covered with 10 nm of conducting TiN deposited either by pulsed CVD or sputtering.

Figure 4.6 depicts how the deflection signal, measured in V, is at first constant during approach, as no surface probe interaction takes place. Then, at the "snap in" point, attractive van der Waals forces dominate (see Lennard-Jones-Potential in Fig. 4.1). The deflection signal decreases until the probe moves even closer to the sample surface and repulsive Coulomb forces dominate probe behavior. At this point the signal increases with the scanner position. The bias voltage is set to -15 mV. When the probe is pressed harder onto the sample surface a deflection value A is reached where the current measured is not dependent on the deflection anymore. Since the deflection is proportional to the force pressing the probe onto the sample surface the deflection setpoint, defined in section 4.1.1, should always be higher than A. When the probe is moved away from the surface (see dark blue graph in Fig. 4.6) a current is still measured at Z values where there was no current during approach. The resulting hysteresis is the electrical equivalent of the mechanical hysteresis between the "snap in point" e and the "snap off" point e'. However, this method has two inherent flaws. The first flaw is that in the process of determining the correct setpoint the probe might already suffer damage due to high forces on its tip apex, rendering the tips useless for further experiments. This suggests that this method is only useful for determining the correct setpoint range for a certain probe. The second flaw is that the method assumes the probe to be stationary on one location of the sample surface. When acquiring current maps the probe is scanned along the sample surface. For these experiments a setpoint must be found that provides valid and reproducible currents while scanning. For this the TiN surface is scanned while bias voltage is set to -15 mV. Initially the setpoint is set to the value where spatial resolution is satisfactory and scanning morphology acquisition is stable. Now the setpoint is increased until the mean current measured is not dependent on the setpoint value anymore. With the tips most often used this is typically at a value between 0.3 V and 0.6 V above the "snap in point". This is of course dependent on the cantilever spring constant. The Olympus OMCL-AC 240TM tips used in this work have a typical spring constant of $2 \frac{N}{m}$. The resulting force pressing the probe onto the sample surface is in the order of nN. In order to validate the CAFM measurement it is mandatory to repeat one of the procedures explained

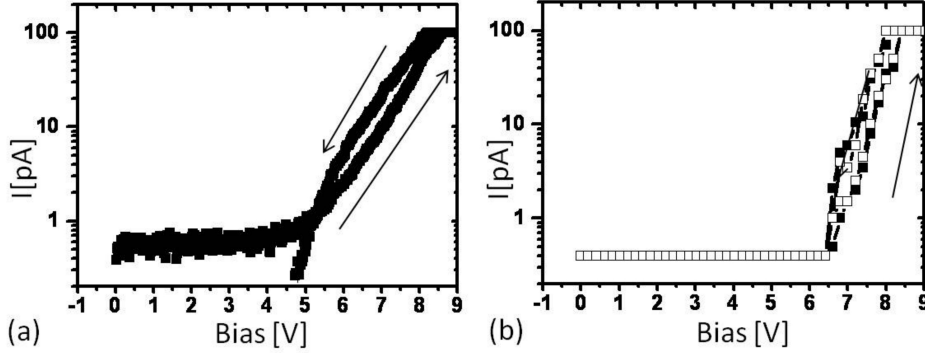


Figure 4.7: (a) Local I-V curves acquired by ramping the current while the tip rests on a specific location. The I-V-curves were started at 0 V. (b) Local I-V curves acquired in the amorphous matrix by extracting the current from an image series. Different symbols represent different locations. [65].

above after each experiment.

As discussed before in this chapter it is possible to acquire current maps along with morphological maps of the sample surface. Thus, correlating morphological properties with electrical ones. To gain further insight into the electrical properties it is also possible to measure local I-V spectra at designated locations of the sample surface. Two methods can lead to the acquisition of these spectra.

- **Local I-V ramps:** Here, dedicated locations of sample morphology are defined and the probe is directed to these locations. After that the bias voltage is ramped according to predefined parameters and the current is measured. Fig. 4.7 a) depicts such a spectrum.
- **Extracted I-V curves from image series:** This method starts by taking a series of simultaneous morphology and current maps of the same area at discrete bias voltages and changing the bias voltage consecutively from image to image. Such a series is partially presented in Fig. 4.8 and 4.7 b). Figure 4.7 b) also shows I-V curves that are assigned to each location by taking into account the entire set of current maps. This is similar to the technique of Seko et al. and Nikiforov et al. [66,67] but this work considers a much larger amount of images, up to 90, enabling a significantly more detailed analysis.

Both methods have their advantages and flaws. The most obvious difference is that the first method only allows conductivity measurement at preselected locations whereas the second method probes the conductivity of an entire area

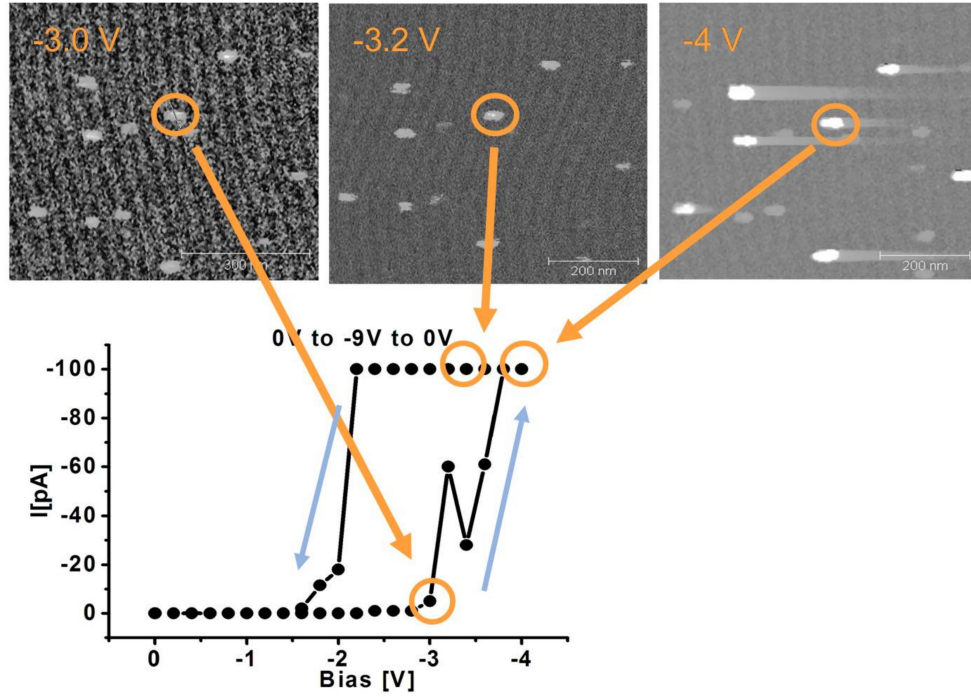


Figure 4.8: Extraction of local I-V curves from consecutive current maps taken at different voltages. The top images show the current maps at different biases, where the brightest signal correspond to higher currents. By taking the current values at a specific location in consecutive current maps entire I-V curves can be extracted. The characteristic is taken at a crystallite site [49].

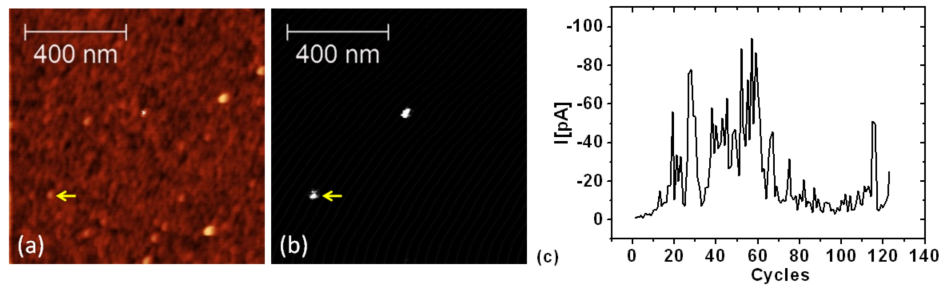


Figure 4.9: Morphology (a) and current map (b) of the sample area scanned 123 times at -2.4 V. Color scale is 5 nm and -10 pA respectively. The current was extracted from current maps at the location marked (arrow) and displayed over the number of cycles in (c).

at different voltages. This is relevant when studying structurally inhomogeneous samples. As a test vehicle for both methods a sample is studied in which $(\text{ZrO}_2)_{0.8}(\text{Al}_2\text{O}_3)_{0.2}$ crystallites are embedded in an amorphous matrix. This way both methods can be compared on the same sample, but on different morphological features. Figure 4.7 shows that the results obtained by both methods on different locations on the amorphous matrix are in fact comparable. However, since local I-V ramps are taken in a relatively short time span these I-V curves are more sensitive to time dependent properties of the dielectric film described in chapter 2. I-V curves extracted from image series take a long time to measure and therefore neglect this information. In Fig. 4.7 a) the decreasing path of the I-V curve actually reaches negative currents. The origin of this is beyond the scope of this section and will be discussed in detail in chapter 5. The I-V curve extracted from the image series in figure 4.7 b) does not exhibit this detail. The reason lies in the time dependence of this effect. There is a significant amount of time between measurements. When it comes to the ability to correlate current and morphology data from local I-V ramps, these have the disadvantage that there is no certainty that the electrical data was acquired exactly at the specified location. Other than the level of confidence in the AFM hardware. Piezo effects like "creep" and "warp" and thermal drift are not negligible. Since the extracted I-V curves deliver a corresponding morphology map to each current map, the exact position of current measurement relative to the sample surface can be verified. This type of experiment can also be conducted in order to determine the effect of repeated electrical on an insulating layer. Figure 4.9 shows such a measurement. The same sample area was scanned 123 consecutive times at a bias voltage of -2.4 V. The current is extracted from the image series, where each measurement was taken of the same area of the sample surface and at the same bias voltage. After 10 scans the current varies strongly after each consecutive scan indicating stress induced leakage currents (SILC), an in depth discussion is given in chapter 5.

In order to confirm electrical damage done by CAFM measurements a second larger set of morphology and current maps is acquired at moderate bias voltage. Figure 4.10 depicts such a set. The currents detected on the pre-scanned area in the center are still at the same locations but are larger in magnitude. This indicates that the currents measured initially are the origin of electrical damage to the film and are located at grain boundaries [14, 15, 65, 68]. This additional spatial information about the electrical damage is unique to the CAFM method.

In conclusion, the information gain achieved by correlating leakage currents and morphology is "bought" by a lower level of precision when measuring current voltage curves. This is a moderate price to pay since direct correlation of electrical and structural data cannot be obtained by other methods. Thus, the additional information supplied by this method is, when experiments were conducted properly, an important addition to the results supplied by standard

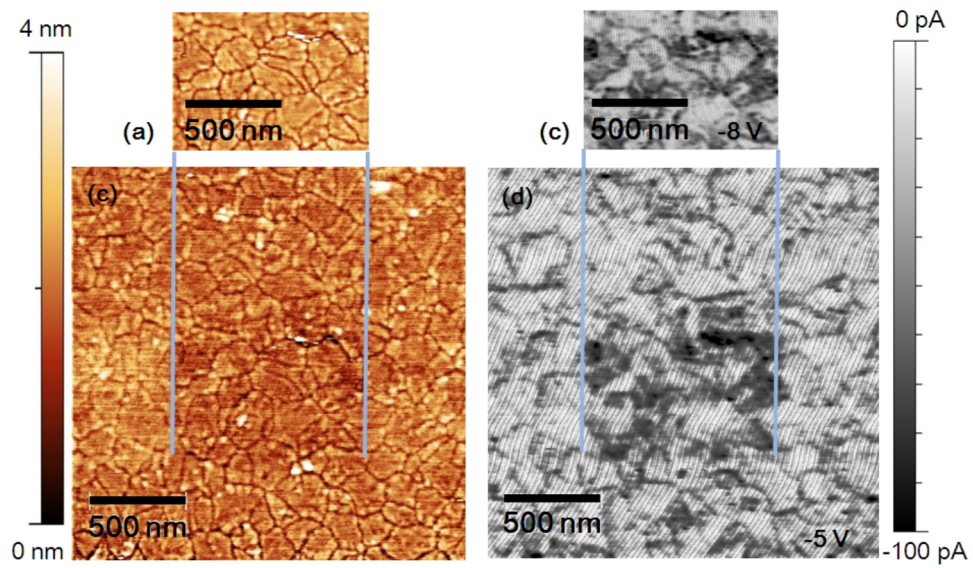


Figure 4.10: AFM morphology and current map of Si/HfSiO₂ with interfacial SiO₂. The insets (a) and (b) were acquired at -8 V whereas the larger maps (c) and (d) were acquired at -5 V. Current scale is 100 pA. The pre-scanned area is clearly visible in the current maps. This is accounted to to the electrical stress induced during the previous scan.

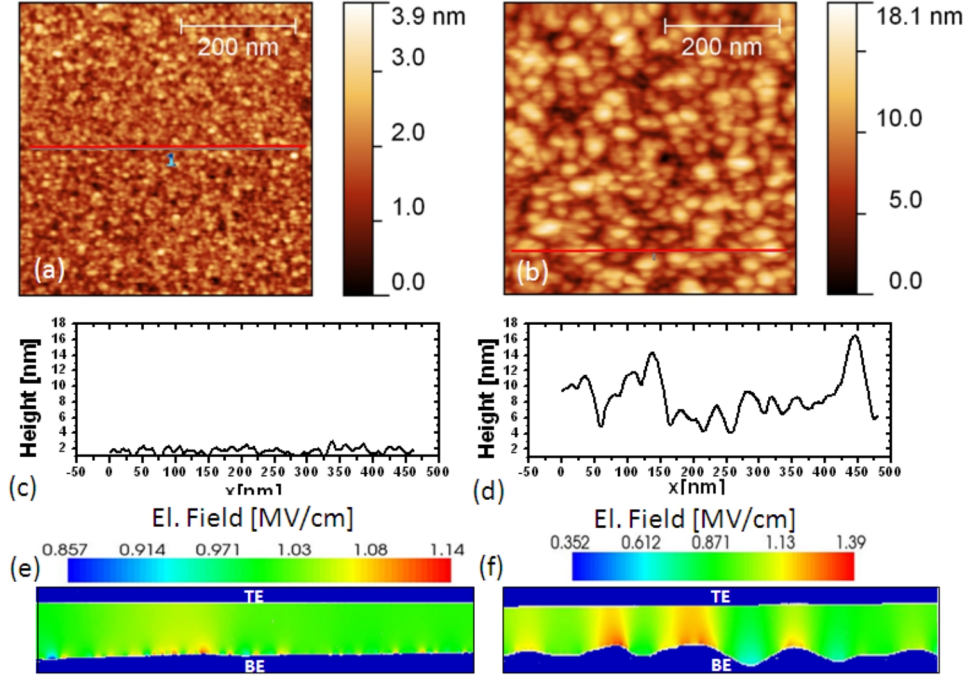


Figure 4.11: AFM morphology maps of the TiN (a) and the Ru (b) bottom electrode. (c) and (d) are profiles along the red line in the corresponding morphology map. (e) and (f) are the calculated electrical fields on the basis of such section cuts. It must be pointed out that the calculations are not based on the exact section cuts in (c) and (f).

characterization techniques.

4.2 Effect of the Bottom Electrode and Defects

In order to determine the applicability of CAFM as characterization tool to examine doped-semiconductor/metal/dielectric-stacks a comparative study of such stacks was carried out [69]². For this purpose, samples consisting of different bottom electrode (BE) materials and marginally different dielectric materials were fabricated. The BE materials were, TiN as a representative for lower workfunction materials and Ru as a representative for higher workfunction materials. The dielectric was HfTiO₂ with different Hf:Ti ratios. These materials were chosen for several reasons. HfO₂ is a standard high k dielectric for capacitor and transistor gate oxide application and in use for the 65 nm

²Copyright (2011) American Institute of Physics. This article may be downloaded for personal use only. Any other use requires prior permission of the author and the American Institute of Physics.

device generation [7]. Ti was incorporated into HfO_2 in order to increase the dielectric constant [70–73]. However, the lower conduction band (CB) offset between HfTiO_2 and the BE material leads to increased leakage currents and poorer insulating quality [74]. In order to increase the CB offset a BE material with a high workfunction is necessary. Rangan et al. have shown that Ru is such a material with a CB offset of 2.4 eV [75]. The resulting leakage currents are within the apparative limits of the current measuring setup. Thus, these samples are an ideal test vehicle for the CAFM setup discussed in this work. Moreover, a comparative study of these material stacks is essential to gain deeper insights on the carrier transport in general.

Five samples were studied. All consist of a 10 nm thick TiN BE, which was deposited by pulsed chemical vapor deposition on a highly n-doped silicon wafer. The Ru BE was deposited by atomic layer deposition on top of the TiN BE. The dielectric layers were deposited by co-sputtering in an industrial sputter system from HfO_2 - and TiO_2 -target³. The Metal-Insulator-Metal (MIM) structure was completed by depositing top electrodes (TE) in a high vacuum evaporation tool by electron beam evaporation. The TE consists of a 10 nm Ti adhesion layer and 200 nm Al. A 12 nm layer of TiO_2 deposited on a TiN bottom electrode and 12 nm of HfTiO_2 with Ti:Hf ratios of 1:1 and 3:2. The latter were deposited on TiN and Ru BE. Figure 4.11 shows AFM morphology maps of TiN a) and Ru b) deposited by pulsed CVD and ALD, respectively. The profiles in b) and c) demonstrate the difference in surface morphology along with the different RMS of 0.44 nm for TiN and 2.52 nm for Ru. To elucidate the influence of the BE topography alone a simulation of the electric field was performed by G. Jegert [76]. The calculated electric fields of similar TiN e) and Ru f) coated with a dielectric film are depicted in e) and f). The electric field is highest where the surface curvature is high but extends further where large grains extend far into the oxide film. These calculations emphasize that an analysis with high lateral resolution is necessary in order to understand transport mechanisms on a mesoscopic scale.

The physical and morphological properties of the material stacks were analyzed. Figure 4.12 shows transmission electron microscopy (TEM) images along with electron energy loss spectroscopy (EELS) measurements of the dielectric layers deposited on top of the Ru BE with a Ti:Hf ratio of 3:2⁴. It is shown that the TiN layer is much smoother than the Ru layer and that both metal layers are polycrystalline. The dielectric layers do not show crystallinity in the TEM images. These measurements also reveal that the thickness of the dielectric layers is fairly homogeneous. Moreover, due to the conformal dielectric deposition, the morphology of the BE is transferred to the dielectric surface. Furthermore, EELS analysis does not yield Ti clustering within the

³This was done at Qimonda Dresden GmbH & Co. OhG.

⁴TEM measurements were undertaken by Lutz Hillmann at Infineon Dresden

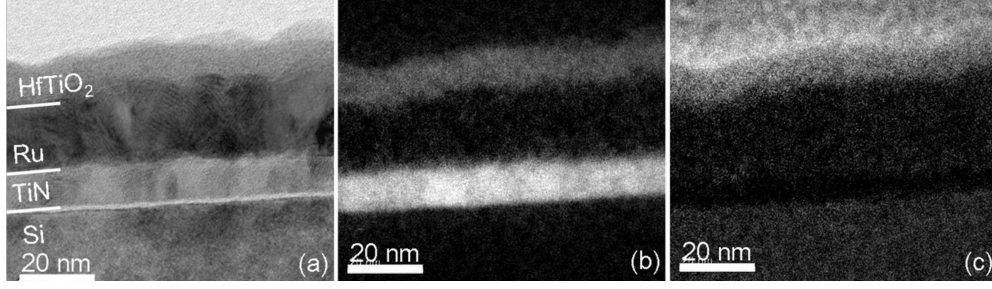


Figure 4.12: (a) TEM images showing a uniform layer thickness of the dielectric on top of the polycrystalline Ru BE. The polycrystalline TiN BE is smooth whereas the Ru BE is comparatively rough. (b) Depicts the Ti- and (c) the O-distribution for the 3:2 Ti:Hf ratio layer as measured by EELS.

dielectric layer.

Figure 4.13 depicts contact mode AFM morphology maps of the dielectric layers deposited on TiN a), b) and Ru c), d). The Ti:Hf ratio is 1:1 for a), c) and 3:2 for b) and d). The measurements confirm TEM experiments, the roughness of the Ru BE is transferred to the HfTiO₂ layer. The incorporation of Ti decreases the roughness only slightly.

Comparison of CAFM experiments (Fig. 4.14) conducted on both BEs and 1:1 and 3:2 Ti/Hf ratios show different spatial current distribution at an applied bias voltage of -0.8 V. In all cases currents occur in "hot spots". This indicates that in this case conduction is a highly local effect. However, it has to be emphasized that in the case of a tip-apex radius of only a few nanometers the electric field is extremely localized due to being dominated by border effects in field geometry. Moving to higher Ti concentrations conductivity of the dielectric increases drastically on both BEs. Current map (c) and current distributions (a) show unimodal current distribution, whereas on the Ru BE charge carrier transport is dominated at fewer sites (e) in the whole area resulting in a bimodal distribution (g). When the Ti:Hf ratio is 3:2 the current distribution (b) is unimodal with negative skew for the TiN BE and bimodal (h) for the Ru BE. Indeed, the maximum current measured is higher for the Ru BE (f). Comparing this information with the TEM/EELS and morphological data acquired we come to the conclusion that conduction is highly dependent on the Ti concentration and the effective CB offset. However, it should be considered that BE morphology can have an even higher influence on conductive properties of the MIM structure.

This is confirmed by observation of the local current evolution in local I-V curves and macroscopic I-V measurements. In Fig. 4.15 local I-V curves were extracted from CAFM image series. These were compared with the mean and median current measured in the same sample area. In addition, macroscopic I-V measurements were made for comparison (insets). These yield mean currents

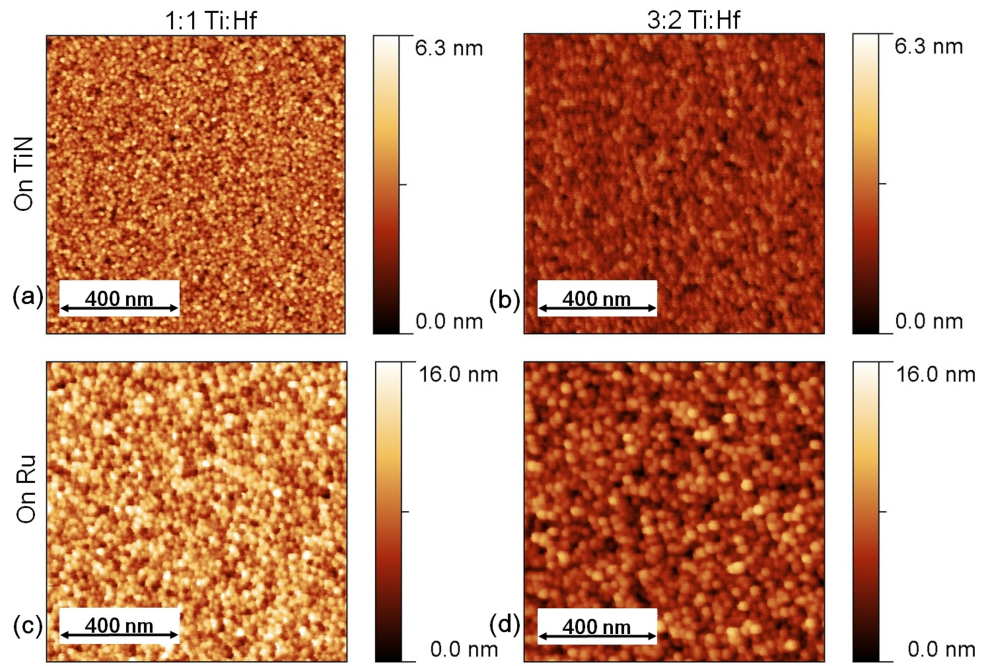


Figure 4.13: Contact mode AFM morphology maps of the layers deposited on TiN (a),(b) and Ru (c),(d). The Ti:Hf ratio is 1:1 for (a)(c) and 3:2 for (b) and (c). Roughness analysis yields RMS: (a): 0.7 nm, (b): 0.4 nm, (c): 2.4 and (d) 1.9 nm

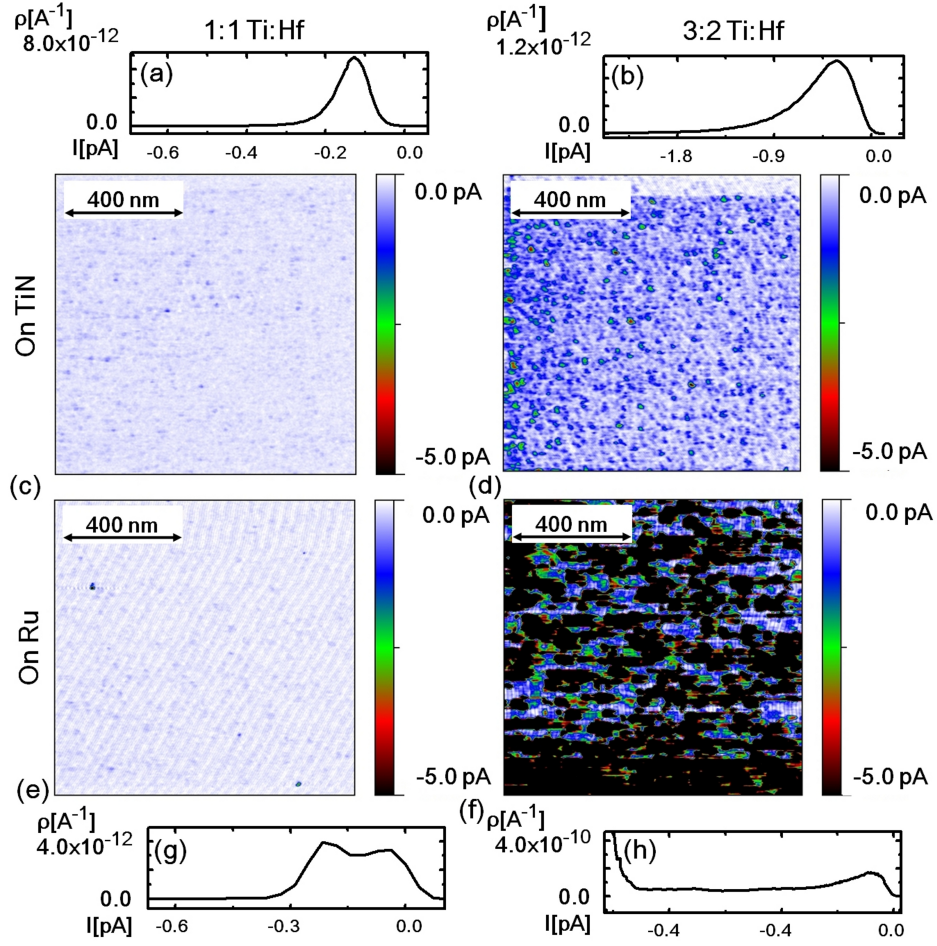


Figure 4.14: 1 $\mu m \times 1 \mu m$ CAFM current maps of the layers deposited on TiN (c),(d) and Ru (e),(f). The corresponding current distributions are depicted in (a),(b) and (g),(f) respectively. The Ti:Hf ratio is 1:1 for (a),(c),(e),(g) and 3:2 for (b),(d),(f),(h). Bias voltage was -0.8 V (substrate injection). False color scale is linear for comparison.

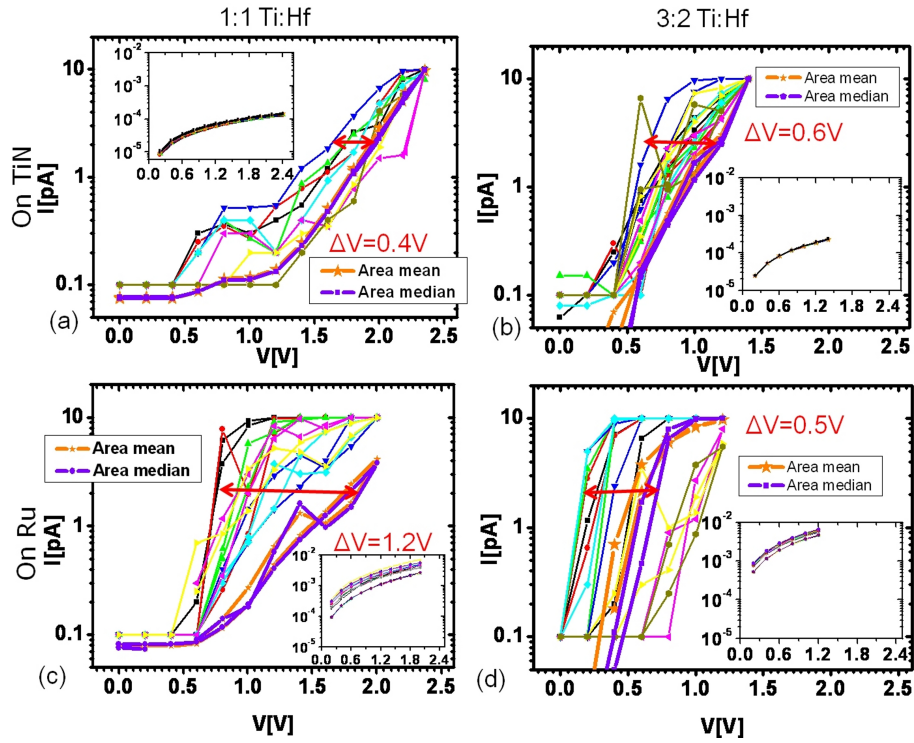


Figure 4.15: Local I-V curves extracted from CAFM current maps of the layers deposited on TiN (a),(b) and Ru (c),(d). The Ti:Hf ratio is 1:1 for (a),(c) and 3:2 for (b) and (d). The insets show the corresponding macroscopic I-V measurements.

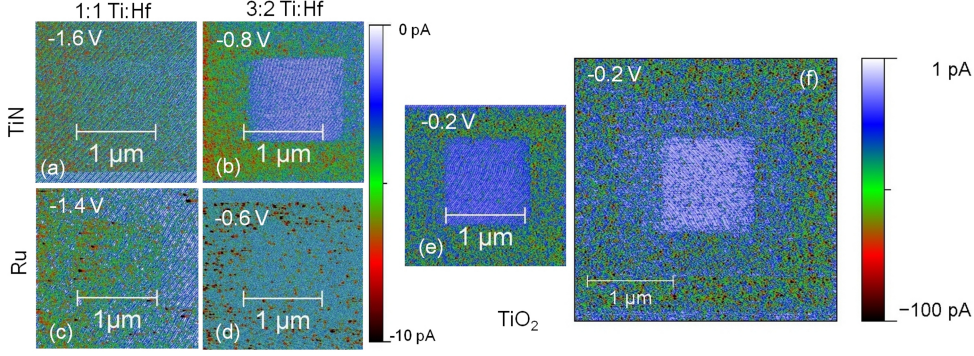


Figure 4.16: Comparison of the current progression of different compositions and on different BE. CAFM current maps of the layers deposited on TiN (a),(b) and Ru (c),(d). The Ti:Hf ratio is 1:1 for (a)(c) and 3:2 for (b) and (d). These were taken of a larger area after the image series for the local I-V curves were taken. Note the different current distribution in (b), (c),(d) and (f). (e) is a current map acquired in the same way on TiO₂ on TiN and (f) was acquired after (e), over an even larger area. The bias voltage used was the bias voltage where the median current exceeded 0.5 pA in the previous image series (depicted in Fig. 4.15). Note that the previous scan area is visible in the current maps. False color scale is set to emphasize local contrast [77].

at - 1.0 V sample bias for TiN BE at a low Ti:Hf ratio (a) of $6.2 \cdot 10^{-5}$ A and high Ti:Hf (b) of $1.2 \cdot 10^{-4}$ A. Correspondingly, for Ru BE $2.3 \cdot 10^{-3}$ A (c) and $5.4 \cdot 10^{-3}$ A (d). Macroscopic I-V measurements integrate currents over the entire TE area yielding ohmic behavior. Only mesoscopic CAFM analysis reveals detailed information about the dielectric thin-film. For comparison between conductive sites and the median current over the whole area ΔV is defined. This is the maximum difference of bias voltage V , at which the current of 2 pA was exceeded at "hot spots", and bias voltage at which the median current exceeds 2 pA. ΔV is 0.4 V for the TiN at low Ti (a) and 0.6 V at high Ti content. For the Ru BE it is 1.2 V for low Ti (c) content and 0.5 V for high content (d). Moreover, notice that in (d) the median current differs from the mean current and the median and mean current have a similar slope as the "hot spot" I-V curves. This, and the higher ΔV is an indicator that extrinsic electronic properties like trap states below the CB become dominant for charge carrier transport for the Ru BE. Whereas for the TiN BE intrinsic properties like CB offset are more visible in I-V measurement.

Fig. 4.16 depicts another electrical process in the dielectric layer. After acquiring the CAFM image series shown in Fig. 4.15 the scan area was increased and an additional current map was acquired at a lower bias voltage. False color scale is set to emphasize local contrast [77]. These voltages were chosen with reference to the local I-V curves. For each sample a bias voltage was chosen

at which an intermediate average current was measured. For the TiN BE and high Ti content Fig. 4.16 b), e) and f) the currents measured in the previously scanned area are smaller than in the surrounding, pristine area.

This effect is enhanced by the increased Ti content. For the Ru BE this is only visible for the higher Ti content Fig. 4.16 d). At the lower Ti content the opposite effect is observed: The current is slightly larger in the previously scanned area than in the pristine area (c). This complex behavior is caused by the interplay of trap density and CB offset.

In image (a) where the trap density is low and the CB offset is high, electrons are trapped in the previously scanned area. Thus, current is reduced in this area due to charge trapping. When Ti content is higher even more electrons are trapped at low voltages in the prestressed area, leading to significantly lower currents. As shown in Fig. 4.16 e)-f) this effect is even stronger in TiO_2 . On the Ru BE in Fig. 4.16 c) the currents in the prestressed area are similar or larger. This is attributed to additional traps created during previous measurements by thermochemical bond breakage [78]. This area is electrically damaged and this damage prevails in the later scan and becomes the dominant mechanism. In contrast, when Ti content is higher in image Fig. 4.16 d) the charge trapping is the dominant mechanism and current is again reduced due to charge trapping at low voltages.

In conclusion, a comparative study of HfTiO_2 deposited at two different Ti/Hf ratios and on two different bottom electrodes was carried out by TEM, I-V spectroscopy and CAFM. These yield that the higher surface roughness of the Ru BE is conveyed to the dielectric layer and that the influence on conductivity of this is higher than the influence of the lower conduction band offset of the Ru/HfTiO interface. Accordingly a high CB offset can only be of value when the BE is sufficiently smooth. Furthermore, it was shown that the influence of a lower CB offset is elucidated by CAFM even when macroscopic measurements do not yield this information. Finally, the influence of the CB offset of a material stack on charge trapping was demonstrated. These results imply that multiple functionalities of oxides can be tuned by choice of electrode material and Ti intermixture in the dielectric. Moreover, it was shown that CAFM is a powerful tool to characterize highly local carrier transport because, due to its high spatial resolution, it indeed delivers information the macroscopic I-V spectroscopy does not reveal.

4.3 Summary

This chapter illustrated the working principle of the AFM in general and CAFM in detail. It gave an overview of the limitations of this technique as well as a description of how external influences limit resolution and reliability. Experimental technique was explained in detail and local conductivity mea-

surements were validated on well established and novel dielectric materials. Finally it was demonstrated how CAFM is suitable to distinguish effects induced by the BE from effects induced by film composition where macroscopic electrical characterization fails due to lack of spatial resolution.

5 High-k Materials

To achieve a k -value larger than 30 in thin ZrO_2 films it is necessary to obtain the tetragonal crystalline phase. Typically this can be achieved by either depositing the layer at high temperatures or by a post deposition annealing step. Both methods induce high leakage currents. To reduce these Al_2O_3 can be incorporated in the ZrO_2 film. This can be in the form of an alloy or by depositing small amounts in the center of the ZrO_2 film, forming a $\text{ZrO}_2/\text{Al}_2\text{O}_3/\text{ZrO}_2$ (ZAZ)-nanolaminate. ZrO_2 films have been shown to fulfill the requirements of the 50 nm DRAM technology node [8, 79]. Incorporation of very small amounts of Al_2O_3 into ZrO_2 reduces leakage while maintaining a sufficiently high dielectric constant [6, 22, 80, 81]. A deeper understanding of the mesoscopic mechanisms involved is essential for future materials engineering. On one hand the ZrO_2 - Al_2O_3 system is eutectic, on the other hand Al_2O_3 has a larger band gap than ZrO_2 [82–86]. Therefore the origin of the improved insulating qualities of the ZrAl_xO_y -films and ZAZ nanolaminates remains to be identified. It is unclear if it is, in the case of the alloy, a higher band gap, in the case of the nanolaminate, a higher band gap interlayer between two ZrO_2 layers or generally a different crystalline structure as a consequence of the reduced miscibility of ZrO_2 and Al_2O_3 . This chapter is a comparative study of thin ZrAl_xO_y -, ZrO_2 - and ZAZ-films, deposited by MBD and ALD. The purpose is to gain a deeper understanding of leakage mechanisms and the effect of Al incorporation in ultra-thin dielectric films. To induce crystallinity these films were either deposited at high temperatures or subjected to different RTA processes after deposition. They were characterized by grazing incidence XRD, XRR, TEM, I-V-, C-V-Spectroscopy and CAFM. CAFM has already been used to identify nanoscale crystallites as the origin of high leakage currents in high- k dielectrics [14, 15, 65, 87, 88]¹.

5.1 $(\text{ZrO}_2)_{0.8}(\text{Al}_2\text{O}_3)_{0.2}$ Nanocrystallites

5.1.1 Sample Preparation

The $(\text{ZrO}_2)_{0.8}(\text{Al}_2\text{O}_3)_{0.2}$ sample discussed in this section was prepared by MBD. The dielectric film was deposited on top of a bottom a TiN BE, which in turn

¹The TEM experiments were carried out by Lutz Hillmann at Infineon Dresden. XRR and XRD experiments were conducted by Lutz Wilde at Fraunhofer CNT.

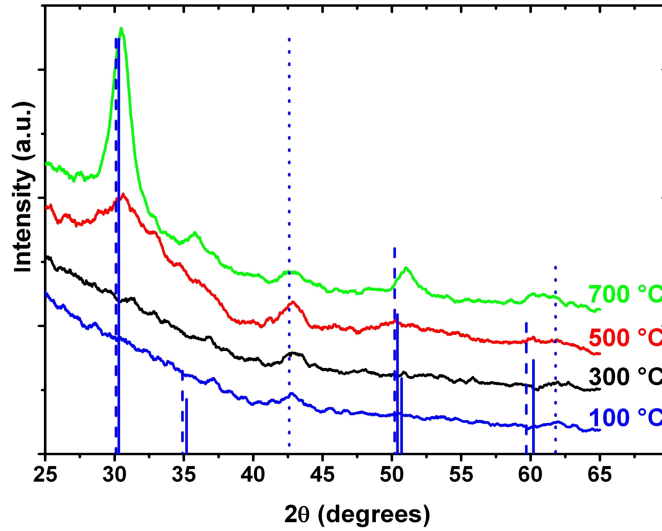


Figure 5.1: GI-XRD spectra of the $(\text{ZrO}_2)_{0.8}(\text{Al}_2\text{O}_3)_{0.2}$ -films. Comparison of different deposition temperatures yields crystallization at high deposition temperatures [14]. The dashed and solid lines mark the position of the peaks associated with tetragonal and cubic ZrO_2 , respectively. The dotted line is associated with TiN.

was deposited on a highly n-doped Si substrate. The BE was deposited by pulsed CVD and is 4 nm thick. The Al_2O_3 was evaporated from an effusion cell and ZrO_2 was evaporated from an electron beam evaporator cell. The substrate temperature was 500°C.

5.1.2 Structural and electrical Characterization

The physical properties of the $(\text{ZrO}_2)_{0.8}(\text{Al}_2\text{O}_3)_{0.2}$ were measured by XRF, GI-XRD and TEM. Additional X-ray fluorescence analysis confirms the films composition as 81.1%at \pm 0.8%at ZrO_2 and 18.4%at \pm 0.8 %at Al_2O_3 .

The GI-XRD results shown in Fig. 5.1 yield a clear dependence of the crystalline properties and substrate temperature. In earlier work by Bierwagen et al [14], the samples deposited at 100°C and 300°C show no crystalline properties in GI-XRD. The films deposited at 500°C show evidence of some degree of crystallization. When $(\text{ZrO}_2)_{0.8}(\text{Al}_2\text{O}_3)_{0.2}$ is deposited at 700°C a distinct peak is visible in the GX-RD graph. This peak can be associated with the tetragonal or the cubic phase.

More detailed TEM investigations of the film deposited at 500°C reveal a films thickness of 20 nm and the formation of crystallites. In Fig. 5.2

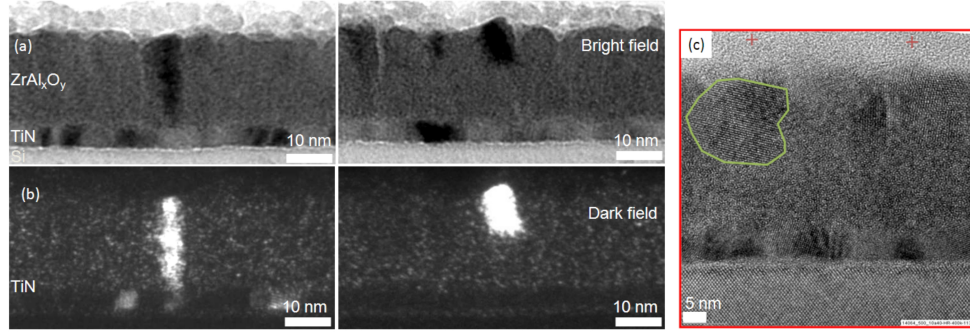


Figure 5.2: (a) Bright field and (b) dark field TEM images of $(\text{ZrO}_2)_{0.8}(\text{Al}_2\text{O}_3)_{0.2}$ films deposited at 500°C . Crystallites appear dark in bright field and bright in dark field images. (c) High resolution TEM images. Note the *Moire* pattern (green) indicating crystallites. The crystallites are embedded in an amorphous matrix. Some extend from the TiN bottom electrode through the entire layer.

crystallites embedded in an amorphous matrix are visible as areas of low brightness in bright field images (a) and as areas of high brightness in dark field images (b). In high resolution images the crystallites are visible as *Moire* patterns indicating interference at similar lattice planes. Some of these crystallites extend from the bottom electrode to the surface of the dielectric film.

Electrical characterization was done on 69 devices. I-V spectroscopy yields a median current density $3.4 \cdot 10^{-1} \frac{\text{J}}{\text{cm}^2} \pm 2.8 \cdot 10^{-1} \frac{\text{J}}{\text{cm}^2}$. However, the majority of devices shows almost ohmic behavior. This is evidence for a broken device. The high leakage current density prohibits reliable capacitance measurement. This and the high variation can be explained by the highly heterogeneous film structure depicted above. To confirm this a detailed highly local leakage current analysis is necessary was carried out.

5.1.3 Nanoscaled Carrier Transport Analysis

In a detailed CAFM study local charge carrier transport at crystallites and amorphous matrix sites was analyzed. For this the methods described in section 4.1.5 were employed. Initially, regular morphology and current maps were measured. As a second step, a long sequence of current maps were acquired at constant bias voltage in order to examine the effects of repeated electrical stress. Local I-V spectra were taken at amorphous matrix sites by ramping the bias voltage up and down in one specific location. Finally I-V spectra were extracted from image series at crystallites and the amorphous matrix.

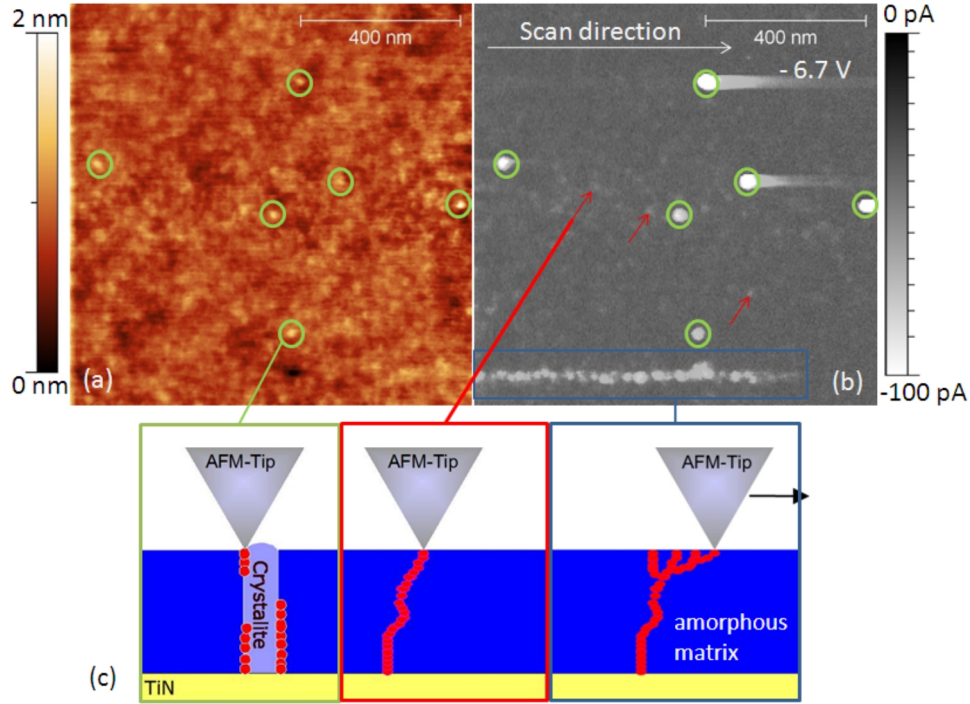


Figure 5.3: (a) Morphology map and (b) current map acquired at -6.7 V. At this high bias three different types of current spots can be distinguished. Green circles mark high current spots that correlate with hillocks in morphology. Red arrows mark low currents that do not regularly correlate with significant surface features. The blue rectangle marks a chain of current spots in the scan direction. (c) Three suggested models for three types of current site. Green: Current along crystallite grain boundaries, Red: Leakage current in the amorphous matrix. Blue: Stress induced leakage currents along defects created by the biased tip. Note the reduced spatial resolution due the the high bias voltage.

Regular morphology and current maps acquired at bias voltages of -6.7 V are shown in Fig. 5.3. The current maps show different kinds of current spots in one map. Comparison with the morphology map yields evident correlation between the bright hillock features in morphology and the leakage spots in the current maps. By taking the structural information from TEM into account these can be divided into three species according to their correlation with morphology, current evolution and the relative magnitude of current. The first type (green circles) of current spot has the highest currents and correlates with hillock features in morphology. This type can be associated with crystallites in an amorphous matrix. Carrier transport occurs along crystallite grain boundaries [14]. Other measurement conducted at crystallites are shown in Fig. 4.9 c). Where the same area was scanned at the same bias voltage of $V = -3.2$ V for 123 successive times. These measurements show increased current fluctuations of a crystallite site. This suggests a contribution of SILC to the formation of a leakage path [89]. This behavior is typical for SILC where charge carriers transport is dominated by trap assisted tunneling and new trap sites are created.

The second type (red arrows) does not correlate with any predominant morphological features. These areas exhibit quite low currents that are distributed almost evenly in the current map. This type can be associated with sites of high leakage current or even incipient dielectric breakdown within the amorphous matrix. The third type (blue box) is composed of a row of current spots aligned parallel to the scan direction. This indicates that the biased AFM tip has produced a dielectric breakdown along some defects in the amorphous matrix. These defects create a leakage path which "follows" the tip along pre-existing defects in the dielectric. This is strong evidence that carrier transport is a highly local effect even in amorphous or nanocrystalline material. In addition, current spots at crystallites are not affected by the scanning motion of the tip, due to the fact that the defect density is much higher there than in the surrounding area. The current spots in the amorphous matrix however are sensitive to the tip movement. This is possible because of a more homogeneous defect distribution in the amorphous matrix.

The following examination will focus primarily on comparing conduction at crystallites with conduction within the amorphous matrix. The evolution of current spots with increasing bias voltage is clearly visible in the current maps in Fig. 5.4 b) and c).

To probe the embedded crystallites local I-V spectra were extracted from image series starting at 0 V. Bias voltage was increased by 0.2 V for each successive image until 4.0 V, substrate injection. Then this bias voltage was reduced again at each new image acquisition until 0 V was reached. This experiment was repeated in reverse order on a different area of the sample. A comparison of I-V spectra starting at 0 V and 4.0 V is depicted in Fig. 5.5. Here, three different types of conduction behavior can be distinguished:

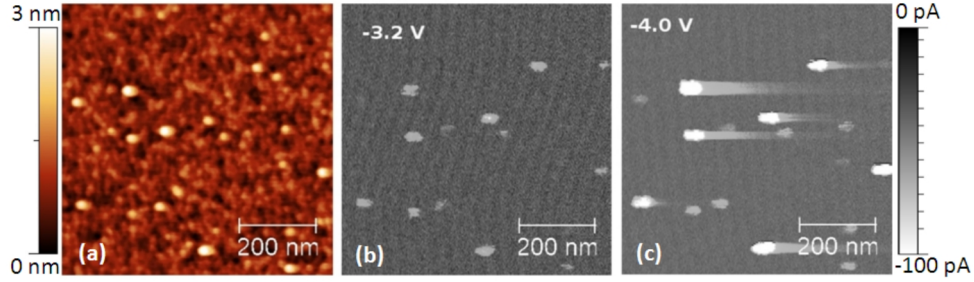


Figure 5.4: Part of a bias voltage series: (a) Morphology mapping, false color scale is 3 nm. (b) Current mapping of the same area at 3.2 V, color scale is 53.50 pA (nonlinear [77]). (c) Current mapping at 4.0 V, color scale is 100 pA (nonlinear) [77]. The morphology does not change during the entire bias series. The smear-like, striping artifacts are an effect induced by the preamplifier.

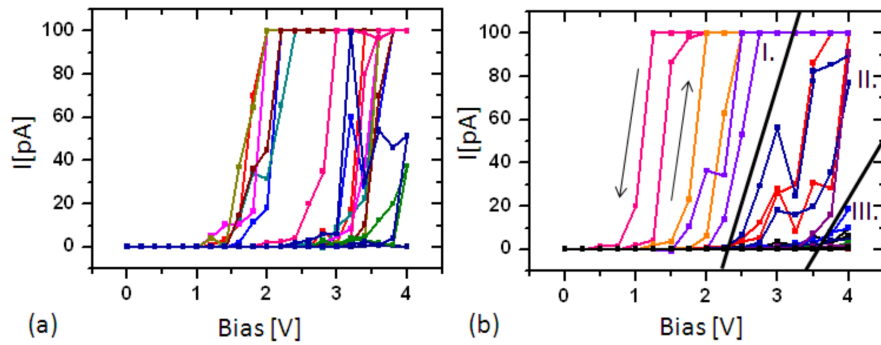


Figure 5.5: Local I-V spectra extracted from image series at crystallite sites. (a) Series starting and ending at 0 V. (b) Series starting and ending at 4 V, substrate injection. I, II and III mark three types of hysteresis for different sites [49].

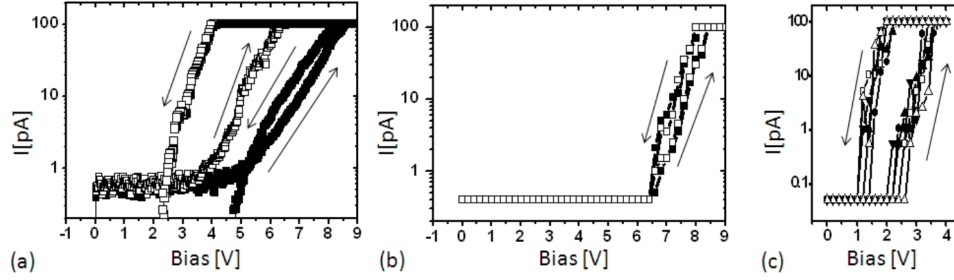


Figure 5.6: Local I-V curves: (a) Acquired in the amorphous matrix by ramping the current while the tip rests on a specific location. Solid squares show the first ramp and open squares the 104th ramp where a filamentary leakage path is already formed. The I-V-curves were started at 0 V. (b) Acquired in the amorphous matrix by extracting the current from an image series. Different symbols represent different locations. (c) Local I-V curves acquired on crystallites by extracting the current from an image series. Different symbols represent different locations [65].

1. High currents at low bias voltage, the preamplifier already reaches its maximum current at low bias voltages. In Fig. 5.5 a) hysteresis is large, in Fig. 5.5 b) hysteresis is small.
2. Lower currents at comparable voltages, with respect to I. the preamplifier limit is reached at high bias voltage. Small hysteresis.
3. Low currents, the pre-amplifier limit is not reached.

In order to establish a figure of merit to characterize hysteresis behavior a factor $\Delta V = v_c - v'_c$ is defined, where v_c is the bias voltage at which currents exceeds 10 pA for the first time in the ascending bias voltage branch and v'_c where current falls below 10 pA for the first time in the descending branch. The hysteresis behavior of type I. of current spots is dependent on the starting bias voltage of the image series. When the series starts at 4 V hysteresis is small, $\Delta V = 0.4 \text{ V} \pm 0.1 \text{ V}$ and when the series starts at 0 V hysteresis is large, $\Delta V = 1.8 \text{ V} \pm 0.3 \text{ V}$. Due to the large hysteresis distribution in Fig. 5.5 b) the distinction is not as obvious as in 5.5 a). The large leakage currents acquired by macroscopic I-V measurement and the similarity of the macroscopic measurements to the local I-V spectroscopy starting at 0 V imply that the comparison of leakage currents at crystallites and in the amorphous matrix that is of most interest. Therefore, this is therefore focused on next.

A detailed comparison of charge transport at crystallites and in the amorphous matrix is depicted in Fig. 5.6. In Fig. 5.6c) the hysteresis behavior for type I

current spots at crystallite sites is shown. In a) I-V curves extracted from image series at pristine amorphous sites are displayed. Here, v_c is $6.8 \text{ V} \pm 0.3 \text{ V}$ (averaged over 3 matrix sites). The increase of current is fairly consistent with Fowler-Nordheim conduction. At 100 pA the maximum measurable current is reached. As the bias voltage is decreased again v'_c is $6.4 \text{ V} \pm 0.2 \text{ V}$. The hysteresis, i.e. the difference between v_c and v'_c , is small ($0.4 \text{ V} \pm 0.1 \text{ V}$). For the later comparison with crystallites it will be important to know how the I-V curves develop when the same site in the amorphous matrix is repeatedly stressed. In this case the leakage behavior changes as generally observed in CAFM measurements [62, 87, 90, 91]. In later ramps v'_c is shifted to values between $3.0 \text{ V} \pm 1 \text{ V}$ and v_c to $5.0 \text{ V} \pm 1 \text{ V}$ and hysteresis is significantly larger than before. Here v_c and v'_c vary so much that taking an average of different locations and measurements does not contribute to clarity. To demonstrate the leakage behavior at a stressed site, the I-V characteristics of the 104th voltage ramp is shown in Figure 5.6 a). Currents are larger at low bias voltage, and the hysteresis is increased. Figure 5.6 b) shows I-V curves taken at amorphous sites by extraction from current mappings. These show the same behavior as the first voltage ramps on a fixed location. This is crucial for the interpretation of the I-V curves extracted for the crystallite sites. At these sites conventional I-V curves cannot be measured reliably, for reasons of piezo creep and warp, see chapter 4. Comparison of Figure 5.6 a) and b) suggests that both types of I-V measurement yield equivalent results. In contrast, Figure 5.6 c) shows the I-V curves extracted for pristine crystallite sites, which exhibit a different behavior. Here, v_c is $3.2 \text{ V} \pm 0.2 \text{ V}$ and v'_c is $1.4 \text{ V} \pm 0.1 \text{ V}$, resulting in a mean hysteresis of $1.8 \text{ V} \pm 0.3 \text{ V}$ (averaged over 5 hillock sites).

For crystallite sites it is known that oxygen vacancies and interstitials are a common defect at grain boundaries [92, 93]. Thus, the leakage path is already present prior to measurement. This explains the large hysteresis at pristine sites in Figure 5.6 c). The measurements imply that the injected charge carriers are trapped at low bias voltage and then detrapped at high bias voltage resulting in a high v_c .

When bias voltage is decreased again trapping dominates over trap assisted conduction only at low bias voltages v'_c (Figure 5.7 e). The fact that the morphology remains unchanged during the entire series and the shape of the decreasing I-V curve is retained confirms that no hard breakdown took place [94]. The comparison of the measurements made at crystallite sites and at amorphous sites reveals remarkable similarities for repeatedly stressed matrix sites and previously unstressed crystallite sites. In both cases the hysteresis is significantly larger than for unstressed matrix sites and absolute v_c and v'_c are much lower.

This is consistent if we bear in mind that electrical stress activates traps which form the leakage path in the amorphous matrix [95], thus creating a situation similar to defects along a grain boundary across the entire layer. Moreover, the

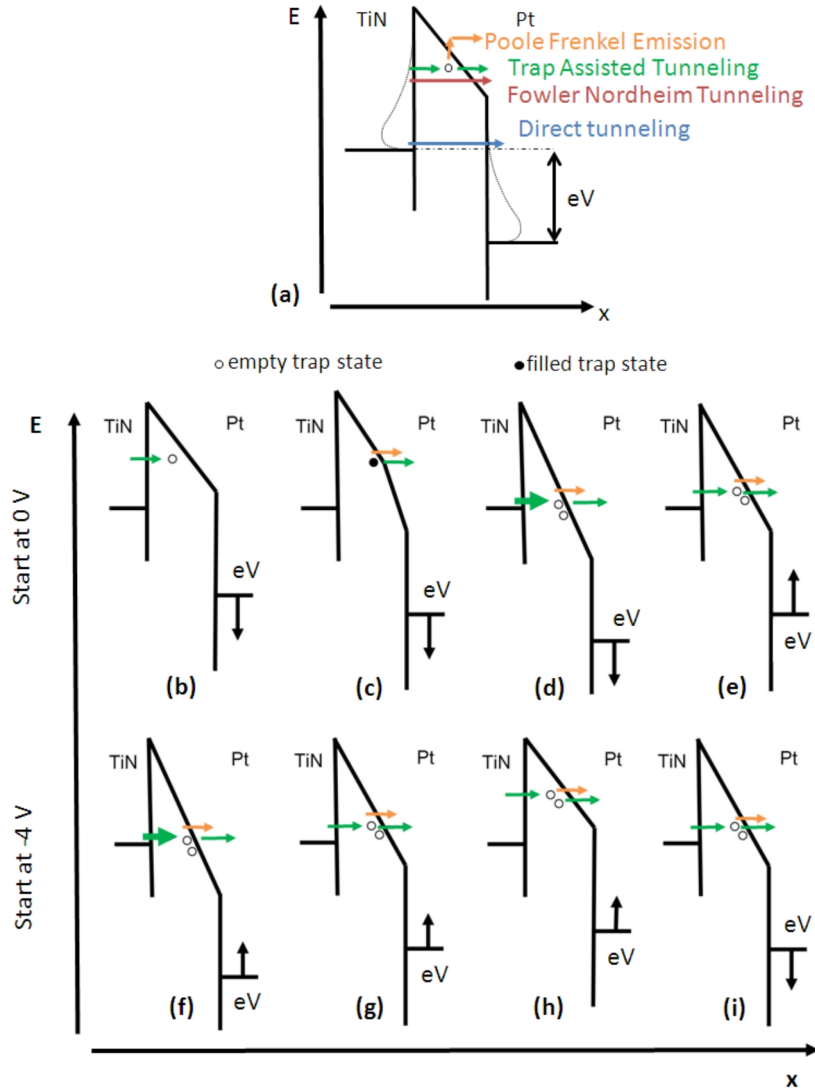


Figure 5.7: Proposed charge carrier transport mechanism: (a) Summary of the four possible mechanisms. Starting at 0 V (b) charges can tunnel into defect states at lower bias voltage. (c) These charges are trapped, causing an internal electric field. These charges can be detrapped and electric stress causes more defects. (d) At higher bias voltages more charges can tunnel into the additional trap states and can be detrapped again. (e) As bias voltage is decreased again the trap states are at higher energies and the charges cannot tunnel into them any more and are not trapped. (f) through (i): Measurement starting at -4 V: (f) At high bias-voltage charges are trapped but detrapped more effectively. Additionally defects are created. (g) These defects act as transient states for charge carriers. (h) This happens even at low bias-voltage. (i) When bias is increased tunneling into trap states does not occur to the same extent as in (c).

shape of the I-V curves (Figure 5.6 a, c) is irregular for both types of sites and significantly different from the exponential increase observed for the unstressed matrix (Figure 5.6 a, b). While the latter is typical for the Fowler-Nordheim dominated conduction, the irregular shape suggests that trap-assisted charge carrier transport mechanisms dominate conduction in unstressed crystallite and pre-stressed amorphous sites. Li et al. and Lucovsky et al. reported on higher leakage current at broken down amorphous sites in an oxygen deficient leakage path, and at oxygen vacancies at crystal grain boundaries respectively [92,95]. Together with our observations this suggests a similarity of defect types but different defect densities at both locations. The different absolute values of v_c and v'_c in crystallite and amorphous sites is determined by the defect density and the number of defects acting as traps. These defects are more likely to form along the grain boundary than inside the crystallites. Therefore, the current voltage measurements confirms tentative observations that carrier transport takes place preferably at the boundaries of crystallites and not through the grains [14].

The fact that the hysteresis is smaller when the series is started at large bias voltages as in Fig. 5.5 a) suggests that the filamentary leakage path is established at high bias voltage by a combination of high electrical fields and SILC as depicted in Fig. 5.7 f). This suggests that charge carrier trapping does not take place to the same extent than when the high electrical stress was applied prior to measurement as shown in Fig. 5.7 g)-i).

5.2 Zirconium Dioxide

5.2.1 Sample Preparation

A 10 nm thick TiN bottom electrode (BE) was sputtered onto a highly n-doped silicon substrate. The dielectric layers were deposited by ALD in a commercial ALD-system². The precursors were tetrakis[ethylmethylamino]zirconium (TEMAZ) for Zr and ozone for oxygen. Deposition temperature was 270°C. The ZrO₂-layers were targeted at 6 nm, 8 nm and 10 nm. Deposition parameters are summarized in table 5.1. Two different RTA processes were carried out, 1 minute at 650°C or 1 minute at 900°C, while purging the chamber with nitrogen. To complete the metal-insulator-metal(MIM) structure for electrical characterization, top electrodes(TE) were deposited. These consist of a 10 nm Ti adhesion layer followed by 200 nm of Al. Ti was deposited by electron beam evaporation and Al by thermal evaporation. The nominal TE sizes were $6.25 \cdot 10^{-5} \text{ cm}^2$, $2.25 \cdot 10^{-5} \text{ cm}^2$ and $1.40 \cdot 10^{-5} \text{ cm}^2$. To reduce errors the size of each individual TE was measured and used for the current density calculation.

²ALD deposition was carried out at Fraunhofer CNT.

Table 5.1: List of sample and deposition parameters. For simplicity, films are referenced to by their target thickness. The ZrO_2 precursor was TEMAZ. The oxygen precursor was ozone and the deposition temperature was 270°C . The purge gas was Argon. The cycle times were TEMAZ 1 s, O_3 4 s, and Ar 8 s

Name	Material	Target thickness	XRR	Cyc. seq.
Z6	ZrO_2	6 nm	4.7 nm	60Zr
Z8	ZrO_2	8 nm	6.1 nm	86Zr
Z10	ZrO_2	10 nm	9.4 nm	110Zr

Table 5.2: Chemical composition of the ZrO_2 -films acquired by XPS.

Name	C1s[at%]	O1s[at%]	Ti2p[at%]	Zr3d[at%]
Z6	3.4	66.5	0.8	28.9
Z8	3.3	66.0	0.1	30.2
Z10	4.2	64.3	0	31.3

5.2.2 Structural Characterization

After deposition of the dielectric films a XPS analysis was done in order to confirm the correct film composition. The results are summarized in table 5.2. The carbon contamination is assumed to be on the sample surface. The Ti2p signal weakens with increasing film thickness. This is due to the limited detection depth of XPS, see chapter 2. Additional support for this is the fact that the O1s and the Zr3d signals increase with film thickness, reciprocally to the Ti2p signal. Furthermore, the XPS spectra in Fig. 5.8 also exhibit a redshift for sample Z8 and Z10 of 0.15 eV. This is due to the higher degree of crystallinity of the thicker films [97]. Comparison of Fig. 5.8 a) with the results by Weinreich et al. in Fig. 5.8 b) exhibit not only a larger Ti2p signal for TiN but also for TiO_2 and TiNO [96]. This is strong evidence for the formation of an interfacial TiO_2/TiNO -layer between the BE and the dielectric.

A detailed structural analysis the ZrO_2 -films was carried out by TEM analysis. The TEM micrographs are shown in Fig. 5.9. As in XPS, an interfacial layer can be seen between the BE and the ZrO_2 . It is important to note that this layer does not contribute to surface roughness. Moreover, TEM micrographs reveal *Moire* patterns indicating incipient crystallization in Z6 in Fig. 5.9 a). As film thickness increases the formation of crystallites becomes more evident, see Fig. 5.9 b) and c). To illustrate the effect induced by post deposition RTA a TEM analysis of the Z8 sample was conducted. The results shown in Fig. 5.10 a)-c) elucidate the evolution of crystallization. Untreated films show the formation of small, ≈ 5 nm wide, crystallites during growth in sample Z8. Larger, ≈ 20 nm wide, crystallites appear after 650°C RTA (b). Finally even larger, ≈ 50 nm wide, crystallites are visible after 900°C RTA (c).

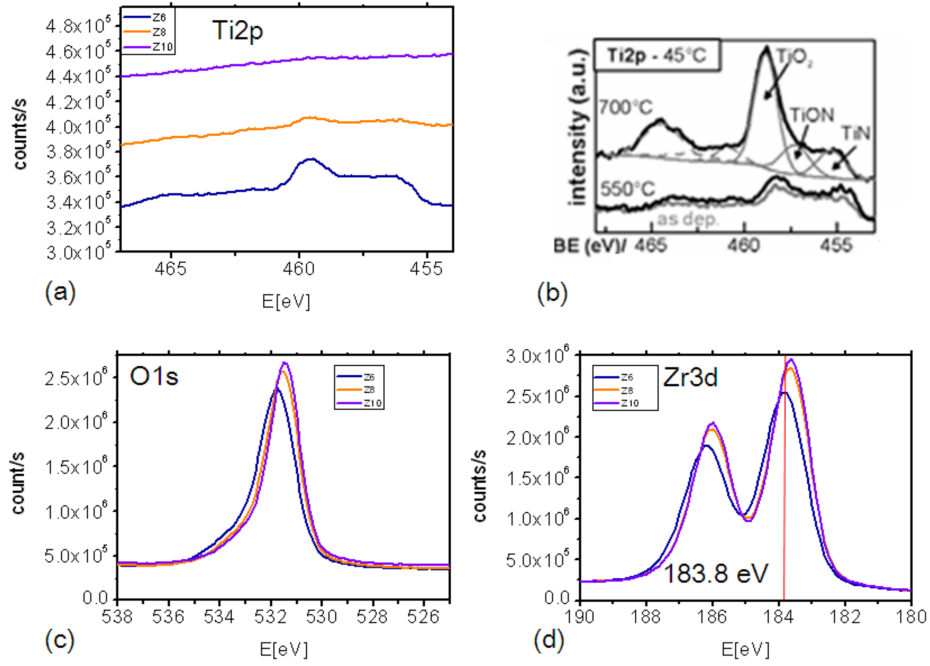


Figure 5.8: XPS Spectra of the ZrO₂ films. (a) Ti2p signal: This signal is strongest for the thinnest film. Moreover, it exhibits the same evidence of TiO₂ and TiON as in (b). Here the Ti2p signal measured by Weinreich et al. on 4 nm of ZrO₂. Deconvolution shows evidence for TiO₂ and TiON [96]. (c) O1s signal (d) Zr3d signal: Analogous to the Ti4p signal is this signal weakest for the thinnest films. This is due to the limited information depth of this method. Note the red shift for the 8 nm and 10 nm films.

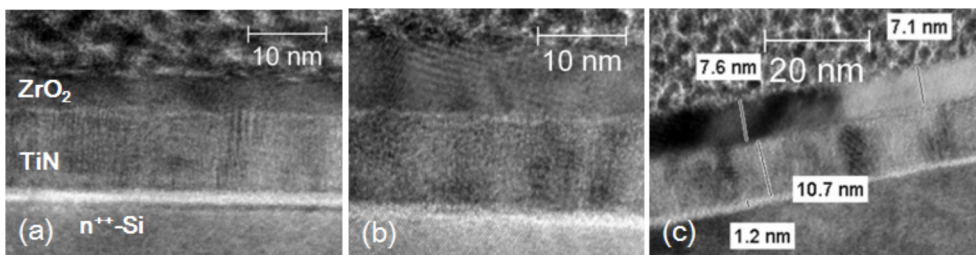


Figure 5.9: TEM micrographs of the ZrO₂-films: (a) Z6. (b) Z8 and (c) Z10

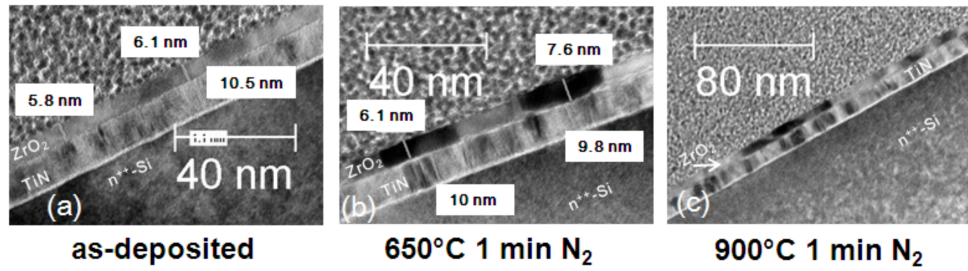


Figure 5.10: TEM micrographs of the 8 nm ZrO_2 -films: (a) as-deposited, (b) after 650°C RTP and (c) after 900°C RTP. An increase in crystallite grain size is visible from (a) to (c). Note the different scale bars.

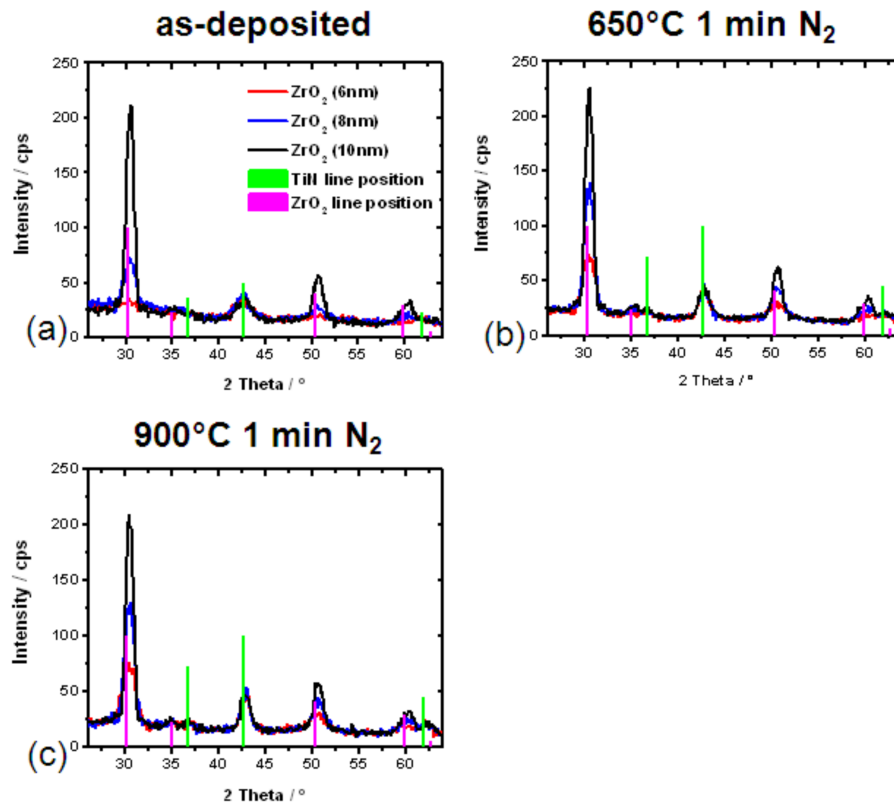


Figure 5.11: GI-XRD graphs of as-deposited (a) ZrO_2 films and of films that have been subjected to a 1 min 650°C N_2 (b) or 900°C N_2 (c) RTA process. (a) Clearly yields enhanced crystallization with increased layer thickness of ZrO_2 . Comparison of (b) and (c) yield the crystallization after 650°C and 900°C to be comparable.

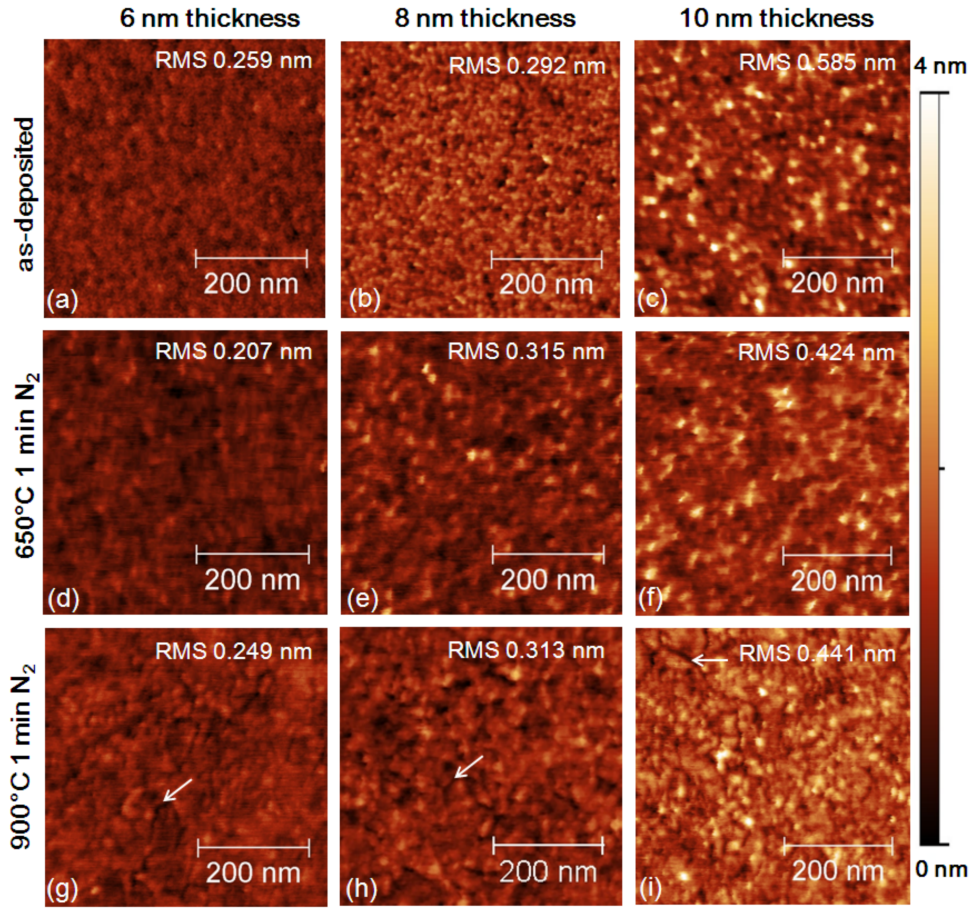


Figure 5.12: AFM morphology maps of the as-deposited and annealed ZrO_2 . (a)(b)(c) are as-deposited, (d)(e)(f) were subjected to a 1 min 650°C RTA in N_2 , (g)(h)(i) were subjected to a 1 min 900°C RTA in N_2 . Layer thickness is 6 nm (Z6) for (a)(d)(g), 8 nm (Z8) for (b)(e)(h) and 10 nm (Z10) for (c)(f)(i). Increased layer thickness shows enhanced surface features in the form of hillocks appearing considerably brighter. Increased anneal temperature induces a network of interconnected trenches. The white arrow in images (g-i) marks such a representative trench.

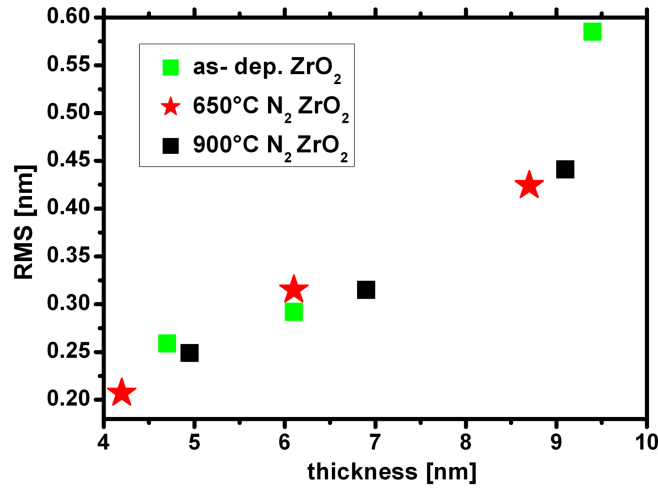


Figure 5.13: Comparison of AFM surface roughness change of ZrO₂. As film thickness increases hillocks form and dominate surface roughness.

To confirm the crystallization during deposition and during RTA all samples were examined by GI-XRD. These yield that at film thicknesses exceeding 6 nm ZrO₂ crystallites form during deposition. Fig. 5.11 a) depicts these GIXRD studies of the as-deposited ZrO₂, which show crystallization for film thicknesses exceeding 8 nm in sample Z8. Fig. 5.11 b) and c) demonstrate that the degree of crystallinity in ZrO₂ is comparable after the 650°C and the 900°C RTA. The effect on surface morphology and the extension of the crystallites within the dielectric is studied by AFM. Fig. 5.12 a)-i) depicts AFM topography maps of the ZrO₂ layers. The number and height of the bright "hillock" features and surface roughness increase with film thickness. Moreover, sample Z10 and all ZrO₂ samples subjected to the 900°C RTA exhibit a network of interconnected trenches separating large areas. This result complies with the increased crystallite grain size visible in TEM micrographs. After the 650°C N₂ RTA surface roughness decreases for all except the 8 nm film. With exception of Z8, although insignificantly, the 900°C N₂ RTA caused surface roughness to decrease in comparison to the as-deposited films but it is still higher than after the 650°C RTA. A comparison of surface roughness and film thickness is displayed in Fig. 5.13. Film thickness and layer density was determined by XRR.

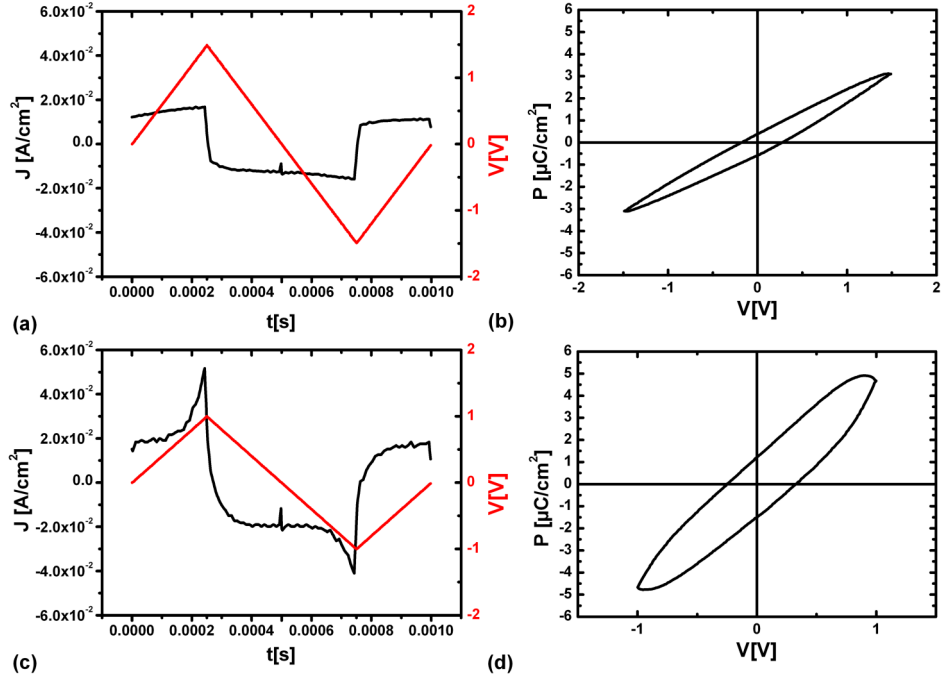


Figure 5.14: Polarization measurements on ZrO₂-films. As-deposited ZrO₂: (a) Voltage and current plotted over time. (b) Polarization plotted over voltage. ZrO₂ annealed at 900°C : (c) Voltage and current plotted over time (c) Polarization plotted over voltage. The results show paraelectric behavior superimposed with leakage currents.

5.2.3 Macroscopic electrical Characterization

Polarization Measurement

Since the dielectric properties like ferroelectricity also has an impact on charge transport in dielectrics and ZrO₂ alloys have been reported to be an incipient ferroelectric, polarization experiment have been carried out [98, 99]. These measurements can identify ferroelectricity and can help distinguish between displacement and leakage currents.

Polarization measurement on the 8 nm ZrO₂-films were conducted at a frequency of 1 kHz. The voltage was swept between -1.5 V and 1.5 V. Fig. 5.14 a) and b) depict the current response and the polarization of the as-deposited film. An ideal paraelectric would have a rectangular current response, due to the fact that the latter is proportional to the change of the applied voltage. The polarization would be a straight line whose slope is proportional to the dielectric constant. In this case, it is ahead of phase of the voltage. The leakage current contribution is in phase with the voltage. The

current response depicted here is the response of a paraelectric material which has considerable leakage currents. The polarization, which is calculated according to equation 3.19 shows some hysteresis which is the direct consequence of leakage currents. Fig. 5.14 c) and d) show analogous results for the sample annealed at 900° in N₂. Note that due to the high leakage currents and low breakdown voltage the voltage was only swept from -1 V to 1 V. For the RTA treated films the leakage currents and the polarization are significantly higher.

Capacitance and Leakage Current Density

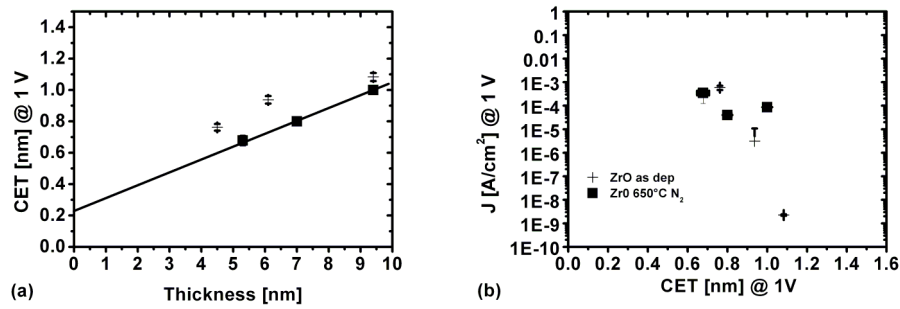


Figure 5.15: Electrical performance of ZrO₂: (a) CET plotted over film thickness. (b) Leakage current density plotted over CET. Labels and legend are valid for both graphs.

Further macroscopic electrical characterization was carried out in the form of C-V Spectroscopy and I-V Spectroscopy. In a first step all samples were electrically characterized at room temperature. These results are summarized in Fig. 5.15. In a second step an in depth leakage current characterization of selected samples was carried out to determine trap levels and the transport mechanism out of variable temperature I-V spectroscopy.

The standardized room temperature experiments summarized in Fig. 5.15 yield that the CET values for as-deposited films thicker than 6 nm are not proportional to film thickness. Combining this information with XPS, GIXRD and TEM data, this suggests that these films are of different crystallinity and therefore exhibit different dielectric constants. For ZrO₂ the 650°C RTA effectively lowers CET but leakage increases from $2.3 \cdot 10^{-9} \frac{A}{cm^2}$ to $5.9 \cdot 10^{-4} \frac{A}{cm^2}$ at 1 V bias voltage. The CET is proportional to film thickness. Structural analysis confirms the crystalline nature of all three ZrO₂ films. For ZrO₂ a k value of 47 can be obtained out of the linear fit. This is close to the theoretical value of 46.6 for the tetragonal phase [11,12]. The fit crosses the ordinate above 0 nm, this is attributed to an interfacial TiON layer and is also visible in XPS and

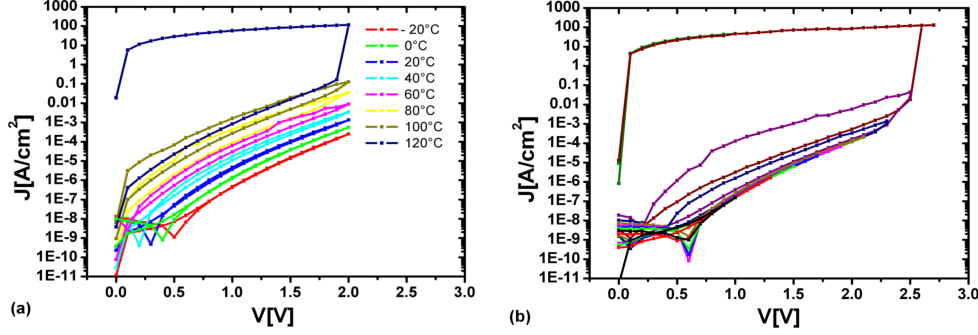


Figure 5.16: Leakage current characteristics of as-deposited Z8 ZrO_2 -film: (a) I-V loops measured automatically at temperatures ranging from -20°C to 120°C . Note negative hysteresis for low temperatures and positive hysteresis for higher temperatures. (b) I-V loops measured manually on one test device at room temperature with increasing maximal voltage V_{max} . V_{max} ranged from 1.0 V to 2.7 V.

TEM images discussed previously. After annealing at 900°C leakage currents increase dramatically, determination of capacitance is no longer possible.

For an in depth and comparative I-V study the as-deposited and 900°C annealed 8 nm thick films were chosen since their performance extends from the acceptable to the unacceptable [100]. In order to determine the trap level below the conduction band edge I-V spectroscopy was carried out over a temperature range from -20°C to 120°C . Moreover, to understand soft breakdown behavior these measurements were conducted in the form of I-V loops. In these the bias voltage started at 0 V, is increased until a predetermined maximal voltage V_{max} . V_{max} is determined on an on-chip test capacitor by measuring subsequent I-V loops at room temperature and consecutively increasing the end voltage with each loop until hard dielectric breakdown occurs. V_{max} of the variable temperature measurements is a voltage well below the lowest value where any breakdown in the test structures occurred. An anticlockwise hysteresis is a sign for dielectric breakdown. In Fig. 5.16 b) such a sequence of I-V spectra measured at room temperature is shown.

For the as-deposited 8 nm thick ZrO_2 the initial I-V loop ends at 1 V and shows clockwise hysteresis. This is due to the current measured at the top electrode actually turning negative while the bottom electrode is still at a positive bias voltage. Electrons are actually flowing back into the bottom electrode.

This is an indicator for charge carriers being trapped in a trap band below the conduction band edge and inducing an internal electric field. This behavior is persistent throughout the following I-V loops until the loops ending at 2.3 V. Incidentally the first loop shows anticlockwise hysteresis. This anticlockwise hysteresis is symptomatic for incipient soft or progressive breakdown. The currents of the next loop concur with the initial loop until bias voltage exceeds

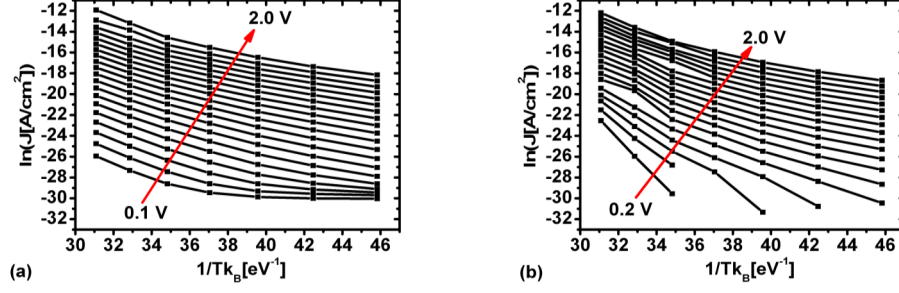


Figure 5.17: As-deposited ZrO_2 : Arrhenius plots extracted from Fig. 5.16 a) (a) First (increasing) branch of the I-V loop (b) Second (decreasing) branch of the I-V loop.

2.3 V. The insulating qualities of the dielectric films degrade further. This is being repeated for each new I-V loop until hard dielectric breakdown occurs at 2.6 V. After hard breakdown the conduction behavior is ohmic.

Since the trap level extraction requires a complete set of I-V spectra taken over a broad range of temperatures without hard breakdown, the maximum bias voltage V_{max} selected for these experiments was significantly lower than the breakdown voltage in room temperature measurement. Fig. 5.16 a) depicts the I-V spectra obtain in such an experiment. V_{max} was 2 V. The temperatures ranged from -20°C to 120°C .

The I-V curves acquired at -20°C essentially resembles the first curves in Fig. 5.16 b) the zero-crossing point is at lower bias though. With increasing temperature this zero crossing point is shifted to lower biases. Moreover, at 20°C an incipient anticlockwise hysteresis can be noticed for larger voltages. This anticlockwise hysteresis is responsible for the shift of the zero-crossing point. For higher temperatures the anticlockwise hysteresis increases. At 60°C the first current discontinuities are visible indicating SILC. Since the increasing branch of the I-V loop always has the same slope and is just shifted to higher current it can well be assumed that persistent dielectric degradation has not taken place yet. A hard dielectric breakdown takes place at 120°C and a bias voltage of 2 V.

Since the I-V loops deliver two different I-V curve branches, which also exhibit different temperature dependent behavior two sets of arrhenius plots can be extracted out of I-V loop data. Fig. 5.17 a) was extracted from the first branch of Fig. 5.16 and b) from the second branch. The different temperature dependencies are obvious. However, these plots are not linear. An arrhenius plot is a linearization method used to extrapolate activation energies out of sets of values which are exponentially dependent on temperature. In cases where not one but two or more competing processes contribute to these values, the

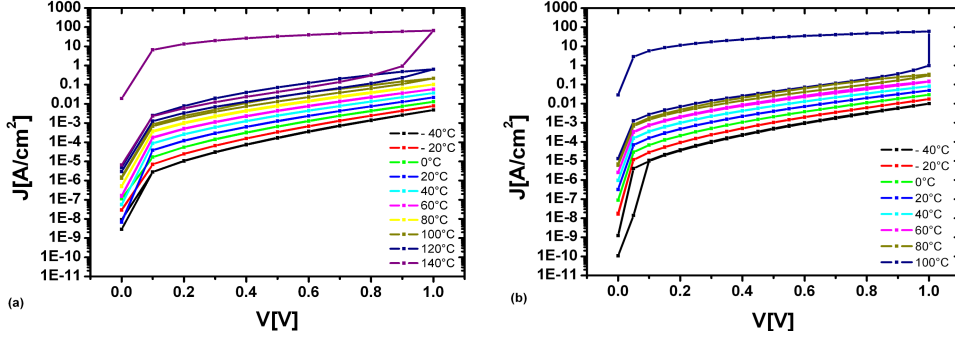


Figure 5.18: Annealed ZrO_2 : (a) I-V loops measured at temperatures ranging from -40°C to 140°C in 0.1 V steps. No negative hysteresis for low temperatures and slight positive hysteresis for higher temperatures. (b) 11 I-V loops measured in 0.05 V steps at temperatures ranging from -40°C to 100°C . V_{max} was 1.0 V.

arrhenius plot does not have to be linear anymore. In the case of two competing processes Celina et al. prove that if one process is more dominant, in one temperature regime, than the other and both processes have different activation energies the arrhenius plot can be a curve [101]. The competition between both processes is the origin for the curvature of the plot. However, different activation energies can be extrapolated for each relevant temperature regime. In arrhenius plots like in Fig. 5.17 the gradual change from low temperature processes to high temperature processes is observed.³ Given more data over a larger temperature and voltage range a more complex analysis scheme could be applied. However, since the temperature range is limited by the probe station and the voltage range is limited by the breakdown voltage of the test capacitors, a simplified approach with two competing processes was chosen. Consequentially, the plots are split into two temperature regimes for the least mean squares regression. The trap level extracted for the first branch of the I-V loops is 0.80 eV below the conduction band edge for high temperatures and 0.45 eV (below the conduction band edge) for low temperatures. For the second branch of the I-V loop the extracted trap levels are 1.04 eV and 0.51 eV below the conduction band edge, at high and low temperatures, respectively. The trap levels and the mean correlation coefficients obtained out the least mean squares regression conducted to determine the activation energies, are summarized in table 5.4.

To determine the effects of the 900°C rapid thermal annealing in N_2 a variable temperature experiments similar to the ones on the as deposited sample were carried out. The resulting I-V spectra are depicted in Fig. 5.18. Fig. 5.18 a) shows a temperature series acquired from -40°C to 140°C and Fig. 5.18 b)

³See Appendix B Fig. 8.2.

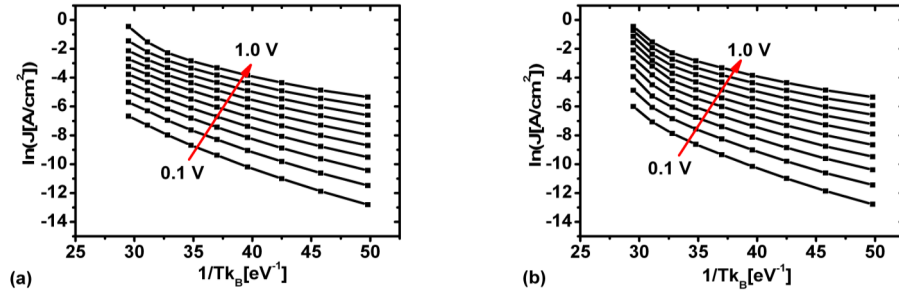


Figure 5.19: Annealed ZrO₂: *Arrhenius* plots extracted from Fig. 5.18 a) (a) First (increasing) branch of the I-V loop (b) Second (decreasing) branch of the I-V loop.

shows a temperature series acquired on a different device from -40°C to 100°C . To verify whether or not the number of measurements has an impact on the I-V behavior the voltage was increased in steps of 0.05 V . The initial I-V loop measured at -40°C shows some small clockwise hysteresis. The first loop exhibiting visible anticlockwise hysteresis is measured at 80°C . Hard breakdown occurs at 100°C . In another measurement shown in Fig. 5.18 a) on a different device the sampling stepsize was 0.2 V . Again some clockwise hysteresis is visible in the I-V loop measured at -40°C . The first measurement showing visible significant anticlockwise hysteresis is again acquired at 100°C . This hysteresis increased in the following I-V loop measured at 120°C . Hard breakdown occurs at 140°C and 1 V bias. Considering that the sampling number of single measurements (voltages) in Fig. 5.18 b) is four times higher than in a) this shows that the number of measurements does have some slight impact on the hysteresis and dielectric breakdown.

As with the as-deposited sample the I-V loops shown in Fig. 5.18 a) taken on the annealed sample were used to extract *Arrhenius* plots. These are shown in Fig. 5.19. The I-V loops also deliver two different I-V curve branches, which also exhibit different temperature dependent behavior two sets of *Arrhenius* plots can be extracted out of I-V loop data. Analogous to the as-deposited sample Fig. 5.19 a) was extracted from the first branch of Fig. 5.18 and b) from the second branch. The different temperature dependencies are visible. Again, these plots are not entirely linear. This suggests that two competing processes with different activation energies contribute to the overall current and each $\ln J-1/Tk_B$ curve has two different slopes [101]. The plots are split up into two temperature regimes for the least mean squares regression again. The trap level extracted for the first branch of the I-V loops is 0.40 eV below the conduction band edge for high temperatures and 0.26 eV below the conduction band edge for low temperatures. For the second branch of the I-V loop the

Table 5.3: ZrO₂: Summary of variable temperature I-V results.

ZrO ₂	Initial Hyst.	T. for clockw. Hyst.	T. for anti-clockw. Hyst.	Hard BD
As-dep.	clockw.	-20°C ...80°C	20°C ...100°C	120°C 2.0V
Annealed	none	–	100°C ...120°C	140°C 1.0V

Table 5.4: ZrO₂: Summary of extracted trap-levels and mean correlation coefficients

ZrO ₂	Temperature regime	Trap Level		Correl. coeff.	
		First	Second	First	Second
As-dep.	High	0.80 eV	1.04 eV	0.983	0.996
	Low	0.45 eV	0.51 eV	0.989	0.988
Annealed	High	0.40 eV	0.65 eV	0.998	0.997
	Low	0.26 eV	0.27 eV	0.992	0.982

extracted trap levels are 0.65 eV and 0.27 eV below the conduction band edge, at high and low temperatures respectively.

5.2.4 Nanoscaled Carrier Transport Analysis

Because the thickest films show crystallization during deposition the question arises whether this has any impact on the electrical properties of the dielectric that cannot be noticed by macroscopic electrical characterization. CAFM provides detailed topographical information correlated with conductivity information. In a first comparative study these 10 nm thick films are compared by CAFM. In a further more detailed study the 8 nm thick films are studied and compared by the method of local I-V spectroscopy already applied in the previous section.

In Fig. 5.20 the topography map a) of 10 nm thick as-deposited ZrO₂ (Z10) is compared to the current map b) measured in that area at -5.6 V. The surface is rough. The hillocks cannot be associated with high currents. Current appears in the form of "hot spots" with a diameter between 15 to 25 nm. These are extremely local dielectric breakdowns induced by the high electric field under the AFM probe. For comparison, the locations of these spots are marked with a red arrow in the current map, and with a green arrow in the topography map. These spots are located at depressions in topography.

In Fig. 5.21 the topography map a) of 10 nm thick ZrO₂ (Z10), annealed at 900°C, is compared to the current map c) at -5.5 V. In addition to hillocks interconnected trenches are observed. These are not visible in the as-deposited

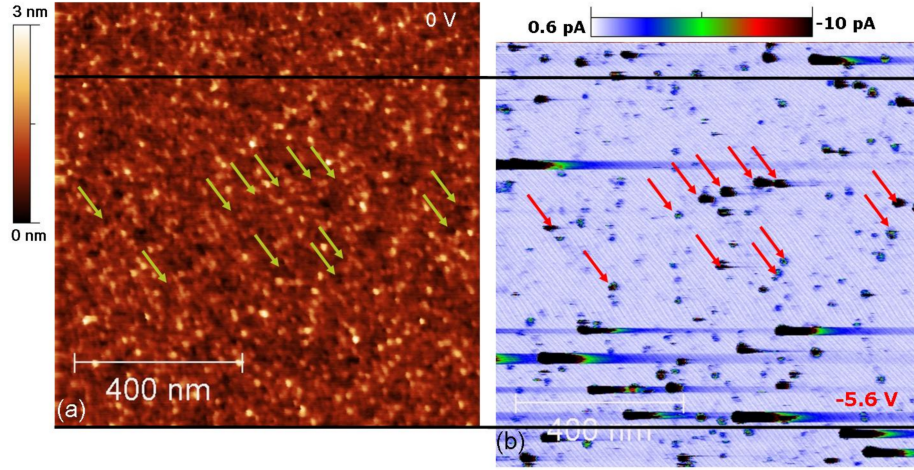


Figure 5.20: Z10: (a) CAFM topography map of the as-deposited 10 nm ZrO_2 film taken at 0 V where spatial resolution is best. The surface is rough exhibiting hillock-like features. (b) CAFM current map taken at -5.6 V substrate injection. The false color bar is linear. The offset between (a) and (b) is due to piezo "creep". High currents are correlated with depressions in the surface.

sample. The inset of Fig. 5.21 b) shows how these trenches separate an entire area from the rest. Taking TEM data and literature into account it these trenches can be associated with crystallite grain boundaries [15, 16, 63]. It is at these trenches where current spots exceeding 10 pA in absolute value are detected. In comparison to the untreated sample the leakage spot density is lower, nevertheless macroscopic measurements show highly increased leakage currents after anneal. The difference to macroscopic measurements is due to different electric fields under the top electrode (TE) and the CAFM tip. Additionally, the CAFM measurements are conducted at a bias voltage. The large TE induces a fairly homogeneous field throughout the dielectric layer in contrast to the very small CAFM probe which induces an inhomogeneous field with extreme field enhancement close to the surface, see chapter 4. It is assumed that CAFM induces a cascade of dielectric breakdowns associated to thermo-chemical bond breakage [78, 81]. These are guided by existing defects [16, 43, 65]. CAFM activates defects which macroscopic measurements do not activate due to lower local electric fields. By taking the known crystallinity of the as-deposited 10 nm ZrO_2 films into account it can be concluded that the crystallite grain boundaries induce the large currents in the CAFM measurement.

To further elucidate the underlying transport properties a comparative study of the 8 nm thick films followed. Local I-V spectra were obtained out of a series of CAFM current maps according to the method discussed in chapter 4. The image series was started at 0 V, bias voltage was increased by 0.4 V with

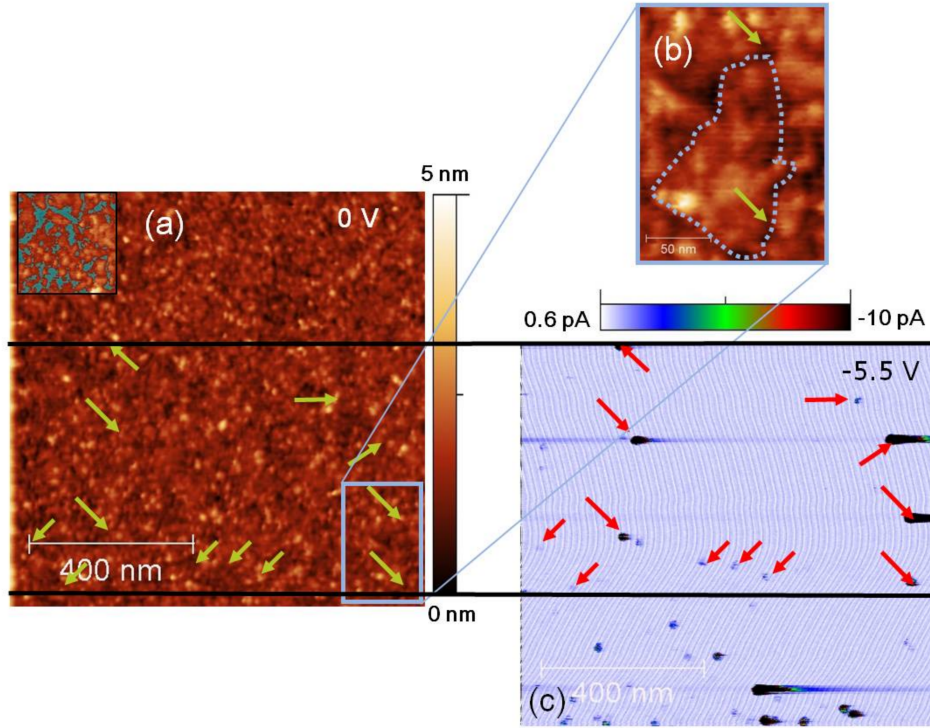


Figure 5.21: Z10: after RTA (a) CAFM topography map of the 10 nm ZrO_2 film subjected to 900°C in N_2 , taken at 0 V. The surface is rough exhibiting hillock-like features and interconnected trenches, see (b). The inset in (a) shows this in a 74.1% threshold analysis [77]. These separate large areas of the surface. (c) CAFM current map taken at -5.5 V (substrate injection). The false color bar is linear. High currents are correlated with trenches separating grains.

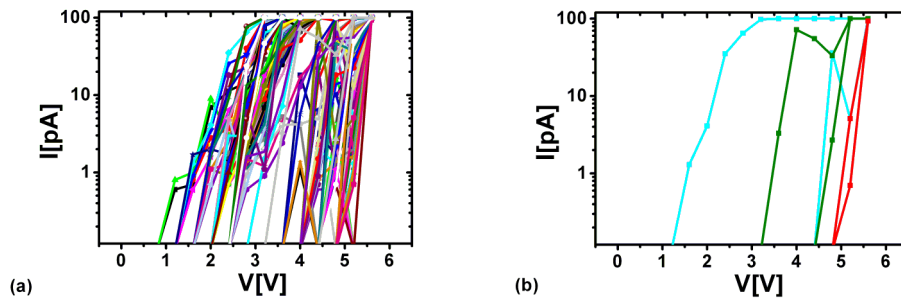


Figure 5.22: ZrO_2 : (a) Local I-V Spectra of as-deposited 8 nm thick film. (b) Selected I-V curves representing no, intermediate and large hysteresis.

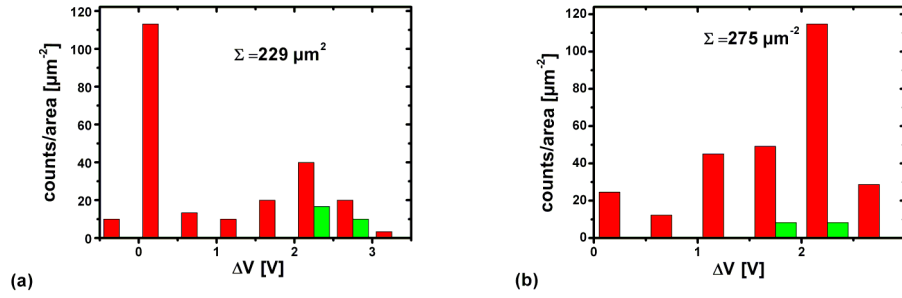


Figure 5.23: Hysteresis distribution and total leakage spot density extracted of the I-V spectra obtained on the as-deposited (a) and the annealed (b) ZrO_2 . The green bars indicate the fraction of leakage spots that were still visible, indicating hard breakdown, in a later scan of the area at 2 V after the acquisition of the image series.

each successive image up to -5.6 V then bias voltage was decreased in the same manner down to 0 V. Fig. 5.22 a) shows such spectra. Out of the large number of spectra obtained, three typical ones are shown in detail in Fig. 5.22 b). The two spectra exhibit anticlockwise hysteresis. Each spectrum is representative for one type: No, intermediate and large hysteresis, respectively. Again ΔV is introduced as a figure of merit for the hysteresis size. Fig. 5.23 a) depicts the distribution of ΔV for the spectra displayed in Fig. 5.22 a). The red bars show the number of I-V curves per area exhibiting a certain hysteresis. The distribution clearly shows that the majority of spectra exhibit no or minor hysteresis. The green bars show the fraction of leakage spots still visible after the acquisition of the entire image series, indicating a local hard dielectric breakdown. The bias voltage applied was only -2 V. The leakage spot density is $229 \mu\text{m}^{-2}$.

An analogous study conducted on the 8 nm ZrO_2 films after 900°C RTA yields a different distribution. For comparability all measurement parameters were the same as with the as-deposited film. The leakage spot density is $275 \mu\text{m}^{-2}$. The distribution displayed in Fig. 5.23 b) shows only few spectrum with no hysteresis. ΔV is distributed over a broad range of values. Most I-V spectra exhibit an hysteresis of 2.0 V or more. The number of hard breakdowns is not significantly different from the as-deposited film. Comparison with morphology yields the local dielectric breakdowns to be located at crystallite grain boundaries. The TEM studies depicted in Fig. 5.10 support this conclusion.

These results annotate that the crystallization of ZrO_2 thin films is indeed film thickness dependent. In general: the post deposition treatment induces an increase in dielectric constant in all films, at the cost of high leakage currents. While keeping the films in an amorphous state during deposition shows only

Table 5.5: List of composition and deposition parameters. For simplicity, films are addressed by their target thickness. The cycle sequence was TEMAZ/TMA/TEMAZ. The oxygen precursor was ozone and the deposition temperature was 270°C. The purge gas was Argon. The cycle times were TEMAZ 1 s, TMA 0.2 s, O₃ 4 s, and Ar 8 s

Name	Material	Target thickness	XRR	Cyc. seq.
ZAZ6	ZAZ	6 nm	4.8 nm	32Zr/2Al/28Zr
ZAZ8	ZAZ	8 nm	6.2 nm	42Zr/2Al/41Zr
ZAZ10	ZAZ	10 nm	7.7 nm	53Zr/2Al/53Zr
ZrAlO 5:1	(ZrO ₂)(Al ₂ O ₃)	6 nm	-	2Zr/11(Al+Zr)/Al/3Zr

little effects in macroscopic electrical performance, nanoscale leakage current analysis anticipates the increase in leakage current induced by post deposition annealing for the thickest film.

5.3 ZrO₂/Al₂O₃/-ZrO₂-stacks

5.3.1 Sample Preparation

In order to study the effects of the incorporation of only one very thin layer of Al₂O₃ within a ZrO₂ thin film, a thickness series of ZAZ-nanolaminate films was deposited on a 10 nm thick TiN BE. This BE was deposited by physical vapor deposition onto a highly n-doped silicon substrate. The dielectric layers were deposited by ALD in a commercial ALD system⁴. The precursors were tetrakis[ethylmethylamino]zirconium (TEMAZ), Trimethylaluminum (TMA) and ozone for Zr, Al and oxygen, respectively. The ZAZ-stacks were deposited at 270°C. With only two cycles of Al included in the center of the film it can well be assumed that the Al₂O₃-layer is not completely closed. The ZAZ-stack's thicknesses were targeted at 6 nm, 8 nm and 10 nm. Deposition parameters are summarized in table 5.5. Additionally, a intermixed 6 nm thick (ZrO₂)(Al₂O₃)-film was deposited for reference. The ratio of ZrO₂ to Al₂O₃ is 5:1. Analogous to the previously discussed ZrO₂-films the ZAZ samples were subjected to two different RTA processes, 1 minute at 650°C or 1 minute at 900°C process, both in nitrogen atmosphere.

5.3.2 Structural Characterization

To confirm composition and to rule out sample contamination all samples were examined by XPS. Fig. 5.24 depicts these measurement. The results are

⁴ALD deposition was carried out at Fraunhofer CNT.

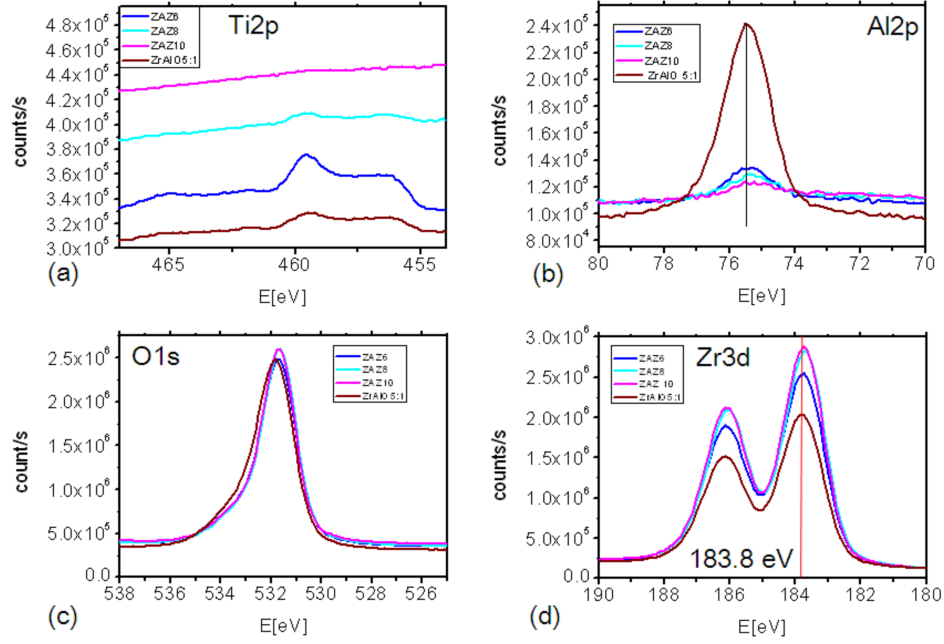


Figure 5.24: XPS Spectra of the ZAZ films. (a) Ti2p signal: This signal is strongest for the thinnest film. Moreover, it exhibits the same evidence of TiO_2 and TiON as in Fig. 5.8 (a). Al2p signal (c) O1s signal (d) Zr3d signal: Analogous to the Ti2p signal this signal is weakest for the thinnest films. This is due to the limited information depth of this method. The peak location is the same for all film thicknesses.

Table 5.6: Chemical composition of the ZAZ- and $(\text{ZrO}_2)(\text{Al}_2\text{O}_3)$ -films acquired by XPS.

Name	C1s[at%]	O1s[at%]	Al2p[at%]	Ti2p[at%]	Zr3d[at%]
ZAZ6	3.1	65.1	3.3	1.0	27.1
ZAZ8	2.9	64.7	3.0	0.2	29.1
ZAZ10	3.7	63.9	2.7	0.0	29.6
ZrAlO 5:1	3.0	65.3	10.9	0.4	20.2

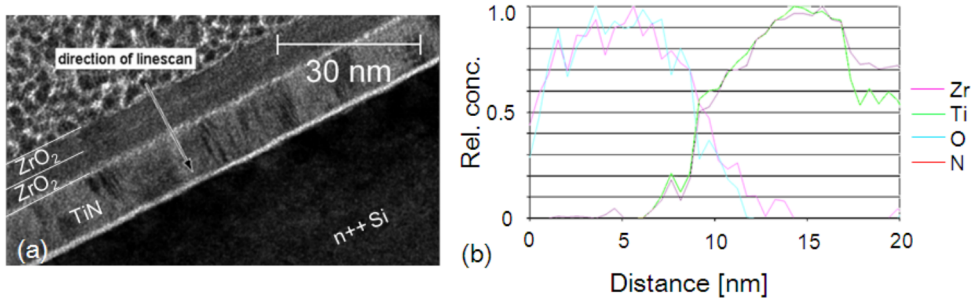


Figure 5.25: Combined TEM and EFTEM analysis of the 10 nm ZAZ film. (a) A white line is visible in the center of the film. However, in the chemically sensitive EFTEM signal no such layer is visible. (b) A more detailed EFTEM line scan at the indicated location in (a) reveals an incipient intermixing at the BE/dielectric interface.

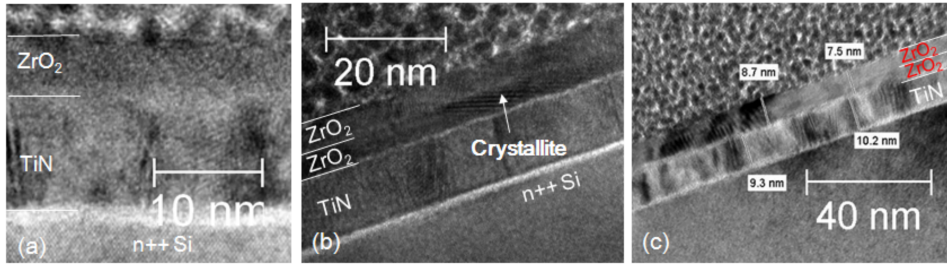


Figure 5.26: TEM study of the crystallization behavior of ZAZ film stacks: (a) TEM image of 5 nm as-deposited ZAZ stack (ZAZ6). No *Moire* patterns are visible. (b) TEM micrograph of the 10 nm as-deposited ZAZ stack. It depicts the abrupt termination of a crystallite in the middle of the layer. It can be well assumed that this is the location of the Al. (c) After an RTP for 1 min at 650°C in N₂ crystallites extend through the entire layer. Note the different scale bars.

summarized in table 5.6. As in the previous section the Ti2p signal is weaker for thicker films. Accordingly the Zr3d and Al2p signals are less strong. This is also due to the limited information depth. A similar interfacial TiO₂/TiNO is also observed. The redshift at larger film thicknesses observed in ZrO₂-films is not observed here. This is due to the amorphous nature of the films discussed later in this section. The relative Al content varies with film thickness which is to be expected for constant absolute Al content and increasing film thickness. To examine the interfacial bottom electrode/dielectric layer and the Al sublayer further, a combined TEM imaging with energy filtered TEM measurement on the 10 nm thick ZAZ film was carried out. In Fig. 5.25 a) a fine line is observed in the center of the ZrO₂ layer. Although energy-filtered TEM does not resolve Al at this location in Fig. 5.25 b), it can be assumed that this is the location

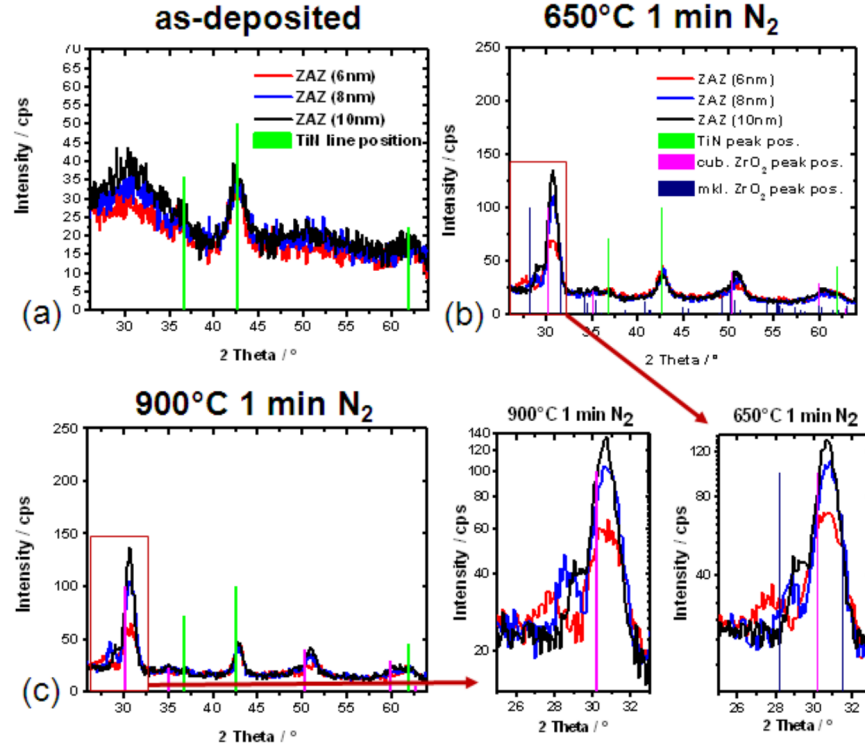


Figure 5.27: GI-XRD graphs of as- deposited (a) ZAZ films and of films that have been subjected to a 1 min 650°C N_2 (b) or 900°C N_2 (c) RTA process. (a) clearly yields that Al incorporation has suppressed crystallization during deposition. ZAZ films that are annealed show a satellite peak to the 30.5° ZrO_2 -peak ((b) and (c)). The satellite peak is shifted towards the main peak as film thickness increases.

of the Al_2O_3 . An intermixing of TiN and ZrO_2 is also observed, confirming the results obtained by XPS.

For a comparison of film thickness dependent crystallization TEM micrographs were acquired of the 6 nm and 10 nm ZAZ-films (ZAZ6 and ZAZ10). Fig. 5.26 a) shows no crystallites in the 6 nm (ZAZ6) film. Fig. 5.26 b) depicts a detailed TEM analysis of the as-deposited 10 nm ZAZ films (ZAZ10) before a) and after b) RTP. In Fig. 5.26 b) a fine line is observed in the center of the ZrO_2 layer. Importantly, it is also shown that crystallites end abruptly at this location. This demonstrates that already two cycles of Al interrupt crystallization during deposition due to a different crystallization behavior after Al_2O_3 deposition. Moreover, after 650°C RTA separate, large crystallites arise throughout the layer.

In order to verify the crystallization behavior by TEM, GIXRD measurement were conducted with all ZAZ films and the ZrAlO film. The latter was mea-

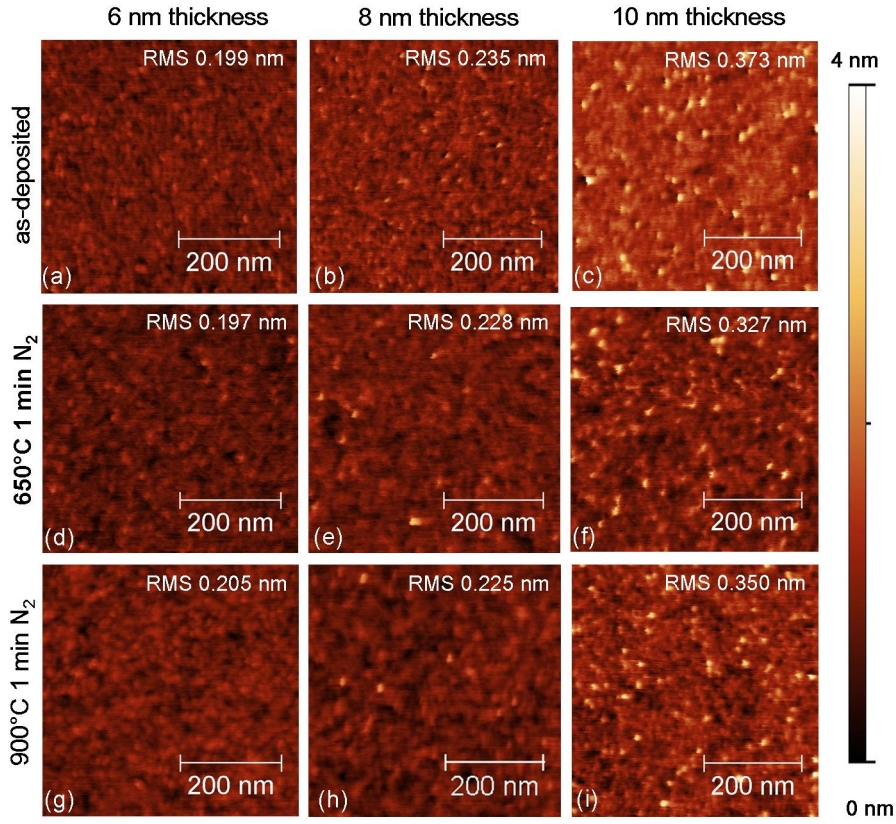


Figure 5.28: AFM morphology maps of the as-deposited and annealed ZAZ. (a)(b)(c) are as-deposited, (d)(e)(f) were subjected to a 1 min 650°C RTA process in N_2 , (g)(h)(i) were subjected to a 1 min 900°C RTA process in N_2 . Layer thickness is 6 nm (ZAZ6) for (a)(d)(g), 8 nm (ZAZ8) for (b)(e)(h) and 10 nm (ZAZ10) for (c)(f)(i). Increased layer thickness induces pronounced surface features in the form of hillocks. Increased anneal temperature induces enhanced surface features only for the 8 and 10 nm thick films.

sured using variable temperature GIXRD. This showed no crystallization up to 750°C. Only after an ex-situ 900°C RTA process did this film show crystallization. Fig. 5.27 show the result of GIXRD on the ZAZ-nanolaminates. Fig. 5.27 a) show that the incorporation of 2 cycles of Al sufficiently suppresses crystallization during growth in films thicker than 6 nm. During RTA the layers crystallize and a satellite peak at lower angles of the peak associated with cubic/tetragonal ZrO_2 at $2\theta = 31^\circ$ appears. The distance between this peak and its satellite decreases with film thickness. This satellite peak does not appear in the pure ZrO_2 in Fig. 5.11. The height of this peak increases with RTA temperature. It is assumed to be a peak induced by strained monoclinic ZrO_2 caused by the sublayer of Al_2O_3 .

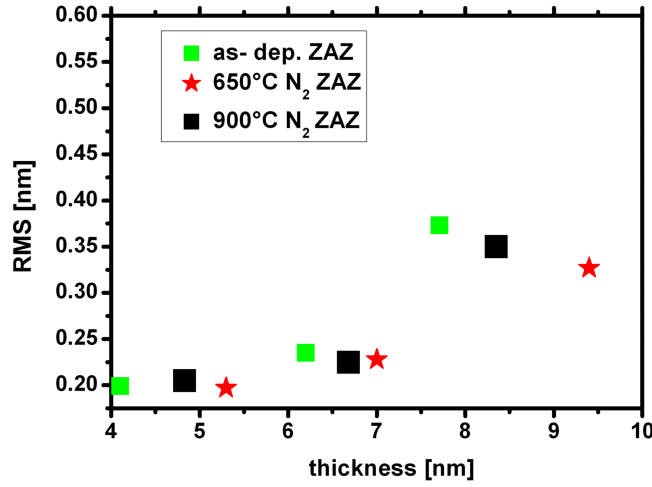


Figure 5.29: Comparison of AFM surface roughness change of ZAZ.

Fig. 5.28 shows AFM topography maps of the ZAZ films. The influence of layer thickness can be seen from left to right. Hillock like features can be seen in c), f) and i), the thickest films. The effect of annealing is not as pronounced as in ZrO_2 . The two thicker films in Fig. 5.28 h), i) develop surface features analog to ZrO_2 , see Fig. 5.12 h), i), but far less pronounced. A small change in surface roughness is observed prior and posterior to RTA in the 6 nm and 8 nm ZAZ films (ZAZ6 and ZAZ8). The 10 nm ZAZ film (ZAZ10) gets smoother after the 650°C and the 900°C anneal. The film annealed at 650°C has the lowest RMS. Comparison of surface roughness in Fig. 5.29 yields that surface roughness increases more sharply with film thickness for ZrO_2 (Fig. 5.12) than for ZAZ. This is consistent with the results of the TEM and XRD measurements. The increase in surface roughness with film thickness is evident for both types of films, as-deposited ZrO_2 however is rougher than ZAZ stacks.

5.3.3 Macroscopic electrical Characterization

Polarization Experiments

Analogous to the polarization measurement on ZrO_2 the characterization of the dielectric properties of the ZrO_2 thin-films was studied by conducting polarization experiments. These were conducted to distinguish between displacement and leakage currents and to determine the influence of a possible ferroelectricity on charge carrier transport [98, 102].

These measurements were also conducted with the 8 nm ZAZ-films. Fig. 5.30 a) and b) depict the current response and the polarization of the as-deposited

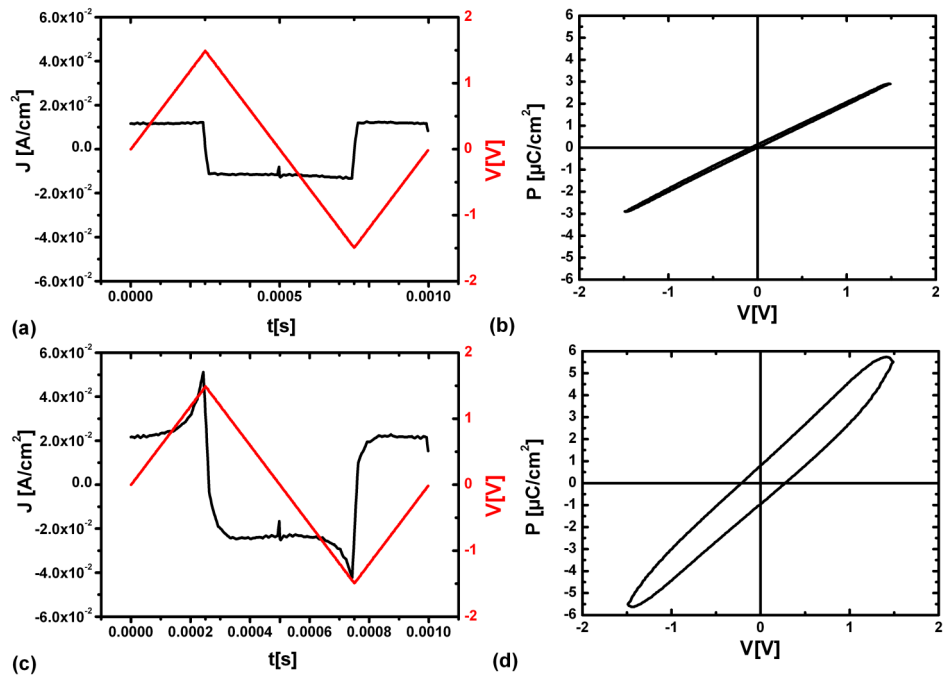


Figure 5.30: Polarization measurements on ZAZ-films. As-deposited ZAZ: (a) Voltage and current plotted over time. (b) Polarization plotted over voltage. ZAZ annealed at 900°C : (c) Voltage and current plotted over time (c) Polarization plotted over voltage. The results show paraelectric behavior superimposed with leakage currents for both films.

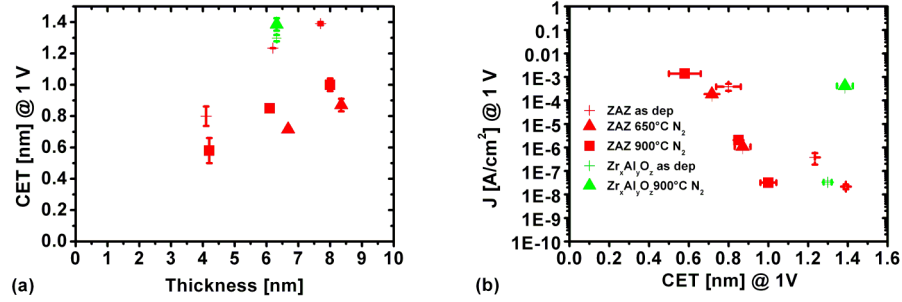


Figure 5.31: ZAZ: (a) CET plotted over film thickness. (b) Leakage current density plotted over CET.

film. The current response depicted here is the response of a paraelectric material where the current response is proportional to the change of the applied voltage. In contrast, leakage currents are almost negligible. Consequently, the polarization shows no significant hysteresis. Fig. c) and d) show the results for the sample annealed at 900° in N₂. The leakage currents are significantly higher as well as the polarization. Note the higher bias voltage than for the annealed ZrO₂ sample. This explains the higher polarization. The current response is similar to the one of ZrO₂ measured with an voltage amplitude of 1 V.

Capacitance and Leakage Current Density

As with the pure ZrO₂ films macroscopic electrical characterization was carried out in the form of C-V Spectroscopy and I-V Spectroscopy. In a first step all samples were electrically characterized at room temperature. These results are summarized in Fig. 5.31. In a second step an in depth leakage current characterization of selected samples was carried out to determine trap levels and transport mechanism out of variable temperature I-V spectroscopy. The results obtained for as-deposited ZrAlO films in standardized C-V and I-V spectroscopy show that incorporation of Al₂O₃ into the ZrO₂ lowers capacitance. This resulted in a CET of 1.3 nm for a 7.9 nm film. The leakage current at 1.0 V are low at $3.3 \cdot 10^{-8} \frac{\text{A}}{\text{cm}^2}$. The RTA step did not lead to significantly decreased CET and the leakage currents increased by four orders of magnitude.

The results obtained for the ZAZ film are different. Since film thickness dependent crystallization is suppressed in ZAZ films the crystal structure is similar within the series. Thus, the CET values have a more linear relation to the layer thickness than for ZrO₂. The leakage current of the ZAZ films is slightly lower

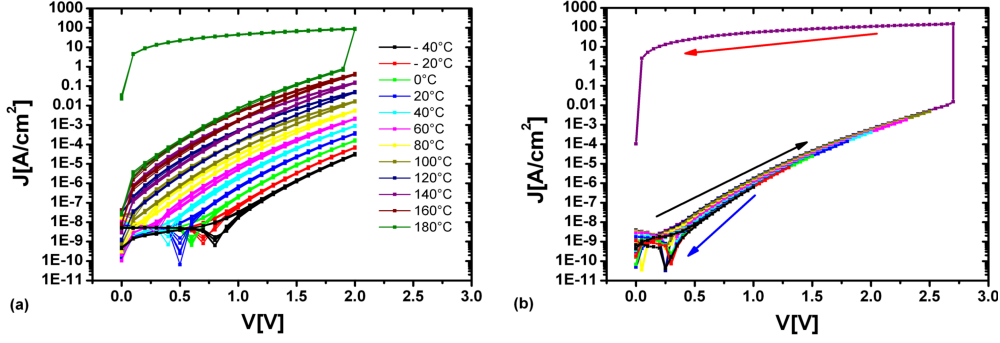


Figure 5.32: As-deposited ZAZ: (a) I-V loops measured automatically at temperatures ranging from -40°C to 180°C . Note negative hysteresis for low temperatures and positive hysteresis for higher temperatures. (b) I-V loops measured manually on one device at room temperature with increasing maximal voltage V_{max} . V_{max} ranged from 1.0 V to 2.7 V.

than for the corresponding ZrO_2 films, except for the 10 nm thick film (Z10) as shown above. After RTA the effect of Al_2O_3 incorporation is more evident. Fig. 5.29 shows that the RTA induces lower surface roughness in topography. TEM analysis yields that crystallite grain sizes increase after this treatment. The incorporation of Al_2O_3 prevents the formation of crystallites spanning the entire dielectric layer. The 900°C RTA effectively crystallizes the entire film resulting in lower CET of 0.7 nm for the 8 nm film and 0.9 for the 10 nm film. The leakage currents remain comparatively low at $1.11 \cdot 10^{-4} \frac{\text{A}}{\text{cm}^2}$ and $2.0 \cdot 10^{-6} \frac{\text{A}}{\text{cm}^2}$ for the 8 and 10 nm films. After 650°C RTA the CET is 1.0 nm while maintaining leakage current density at $3.5 \cdot 10^{-8} \frac{\text{A}}{\text{cm}^2}$ in the 10 nm film. After RTA the 8 nm ZAZ film has a CET of 0.85 nm and a leakage current density of $2.1 \cdot 10^{-6} \frac{\text{A}}{\text{cm}^2}$ at 1 V. In both cases CET was significantly lowered while maintaining low leakage currents.

Analogous to the experiments with ZrO_2 I-V spectroscopy was carried out over a wide temperature range, in order to determine the trap level below the conduction band edge. Again, to understand soft breakdown behavior these measurements were conducted in the form of I-V loops as in the previous section. Fig. 5.32 b) shows a sequence of I-V spectra measured at room temperature. The initial I-V loop ends at 1 V and shows clockwise hysteresis. This is due to the current measured at the top electrode actually turning negative while bottom electrode is still at positive bias voltage. Electrons are actually flowing back into the bottom electrode. This is an indicator for charge carriers being trapped in a discrete trap band below the conduction edge. This behavior is persistent throughout the following I-V loops until hard dielectric breakdown in the loops ending at 2.7 V.

For trap level extraction a complete set of I-V spectra taken at a broad range of temperatures was measured. To avoid hard breakdown the V_{max} selected for

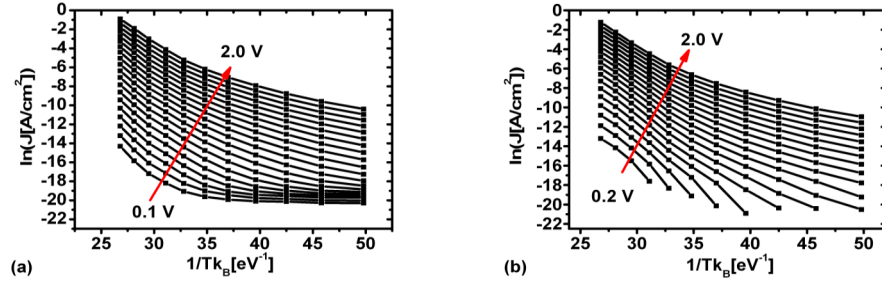


Figure 5.33: As-deposited ZAZ: Arrhenius plots extracted from Fig. 5.32 a) (a) First (increasing) branch of the I-V loop (b) Second (decreasing) branch of the I-V loop.

these experiments in Fig. 5.32 b) was significantly lower than the breakdown voltage at room temperature measurements. Fig. 5.32 a) depicts the I-V spectra obtained in such an experiment. V_{max} was 2 V. The temperatures ranged from -40°C to 180°C . The I-V curves acquired at -40°C are similar to the first curves in Fig. 5.32 b). However, the zero-crossing point is at a lower bias. With increasing temperature this zero crossing point is shifted to even lower biases indicating a temperature dependence, as in pure ZrO_2 . Moreover, at 40°C a incipient anticlockwise hysteresis can be noticed for larger voltages. This anticlockwise hysteresis is responsible for the shift of the zero-crossing point. For higher temperatures the anticlockwise hysteresis increases. No evidence of persistent dielectric breakdown can be found. Hard dielectric breakdown takes place at 180°C and a bias voltage of 2 V.

Again the I-V loops deliver two different I-V curve branches, which also exhibit different temperature dependent behavior. As with ZrO_2 two sets of *Arrhenius* plots can be extracted out of I-V loop data again. Fig. 5.33 a) was extracted from the first branch of Fig. 5.32 and Fig. 5.33 b) from the second branch. The different temperature dependencies are obvious. However, these plots are not linear. Analogous to the procedure already carried out with the *Arrhenius* plots for ZrO_2 each plot is associated with two different slopes [101]. The plots are split again into two temperature regimes for the least mean squares regression. The trap level extracted for the first branch of the I-V loops is 0.80 eV below the conduction band edge for high temperatures and 0.43 eV below the conduction band edge for low temperatures. For the second branch of the I-V loop the extracted trap levels are 1.00 eV and 0.47 eV below the conduction band edge, at high and low temperatures respectively. The trap levels and the mean correlation coefficients obtained out the least mean squares regression conducted to determine the activation energies, are summarized in table 5.8.

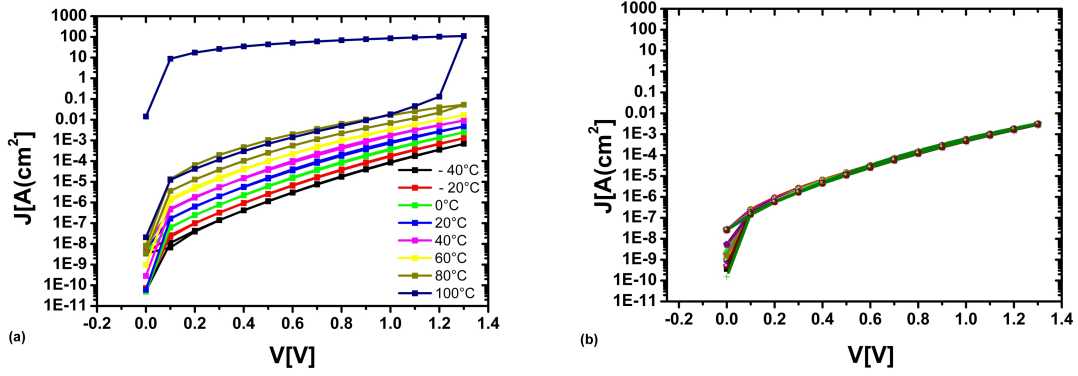


Figure 5.34: Annealed ZAZ: (a) I-V loops measured automatically at temperatures ranging from -40°C to 100°C . Negligible hysteresis for low temperatures and slight positive hysteresis for higher temperatures. (b) 11 I-V loops measured manually on one device at room temperature with a maximal voltage of $V_{max}=1$ V.

To determine the effects of the 900°C rapid thermal annealing in N_2 variable temperature experiments similar to the ones carried out on the as deposited sample were conducted. The resulting I-V spectra are depicted in Fig. 5.34. Fig. 5.34 a) shows a temperature series acquired automatically from -40°C to 100°C . Fig. 5.18 b) I-V spectra carried out to determine whether or not the number of I-V loops done at room temperature has an impact on the I-V behavior. The voltage was swept 11 times, the step-size was 0.1 V and V_{Max} was 1.3 V. All I-V spectra are similar within a mean deviation of 13% .

In variable temperature measurements shown in Fig. 5.34 a), obtained, on a different device the stepsize was also 0.1 V. Here some clockwise hysteresis is visible in the I-V loop measured at -40°C . The first measurement showing visible significant anticlockwise hysteresis is again acquired at 80°C . Hard breakdown occurs at 1.3 V in the following loop, measured at 140°C .

As with the as-deposited sample the I-V loops taken on the annealed sample were used to extract *Arrhenius* plots. These are shown in Fig. 5.35. The I-V loops also deliver two different I-V curve branches, which also exhibit different temperature dependent behavior. Analog to the as-deposited sample Fig. 5.35 a) was extracted from the first branch of Fig. 5.32 and b) from the second branch. The different temperature dependencies are visible. Again, these plots are not entirely linear and each *Arrhenius* plot has two different slopes. The plots are split up into two temperature regimes for the least mean squares regression. The trap level extracted for the first branch of the I-V loops is 0.51 eV below the conduction band edge for high temperatures and

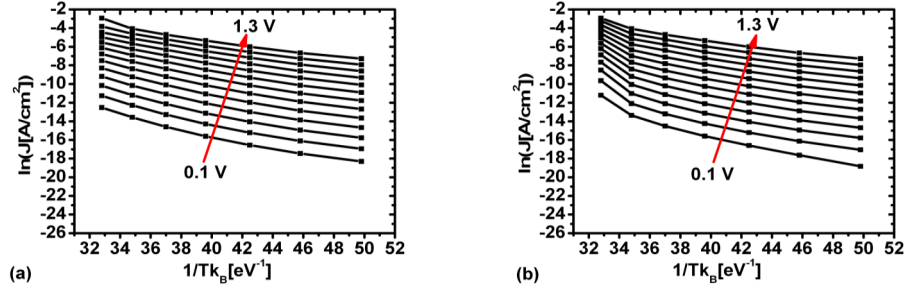


Figure 5.35: Annealed ZAZ: *Arrhenius* plots extracted from Fig. 5.34 a) (a) First (increasing) branch of the I-V loop (b) Second (decreasing) branch of the I-V loop.

Table 5.7: ZAZ: Summary of variable temperature I-V results.

ZAZ	Initial Hyst.	T. for clockw. Hyst.	T. for anti-clockw. Hyst.	Hard BD
As-dep.	clockw.	-20°C ...100°C	40°C ...160°C	180°C 2.0V
Annealed	none	— ...-20°C	80°C ...120°C	100°C 1.0V

0.32 eV below the conduction band edge for low temperatures. For the second branch of the I-V loop the extracted trap levels are 0.75 eV and 0.30 eV below the conduction band edge at high and low temperatures, respectively.

5.3.4 Nanoscaled Carrier Transport Analysis

In Fig. 5.36 the topography map a) of 10 nm as-deposited ZAZ10 film is compared to the current b) measured in that area at -5.7 V. The sample surface exhibits comparable hillock structures to Z10. Some isolated recesses are vis-

Table 5.8: ZAZ: Summary of extracted trap-levels and mean correlation coefficients

ZAZ	Temperature regime	Trap Level		Correl. coeff.	
		First	Second	First	Second
As-dep.	High	0.80 eV	1.00 eV	0.991	0.993
	Low	0.40 eV	0.47 eV	0.962	0.999
Annealed	High	0.51 eV	0.75 eV	0.979	0.858
	Low	0.32 eV	0.30 eV	0.996	0.997

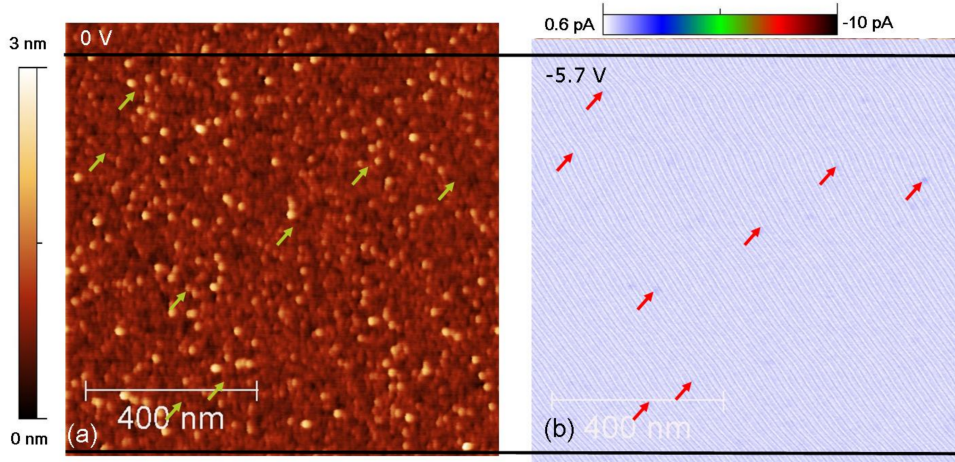


Figure 5.36: ZAZ10: (a) CAFM topography map of the as-deposited 10 nm ZAZ film taken at 0 V. Hillocks are visible. (b) CAFM current map taken at -5.7 V (substrate injection). The false color bar is linear. Few low current spots are barely measurable and cannot be associated to distinct morphological features.

ible. In Fig. 5.36 b) only a few current spots exceeding an absolute value of 1 pA are measured. These do not correlate with morphological features. This corresponds to the amorphous nature of the top part of the ZrO_2 film.

Fig. 5.37 compares the topography map a) of a 10 nm ZAZ10 film annealed at 900°C to the current map b) measured in that area at -5.5 V. Some interconnected trenches appear which are also at the location of current spots in the current map. The number and magnitude of current spots are higher after RTA. These current spots at sites where interconnected trenches are located indicate grain boundaries.

For deeper insight into the dielectric breakdown and leakage behavior the effects of RTA was studied in the 8 nm thick films. As in the previous section, local I-V spectra were obtained out of a series of CAFM current maps according to the method discussed in chapter 4. The image series was started at 0 V, bias voltage was increased by 0.4 V with each successive image until 5.6 V then bias voltage was decreased in the same manner until 0 V. The leakage spot density is $168 \mu\text{m}^{-2}$. Only one I-V loop exhibits hysteresis. ΔV is 3 V. The majority of I-V loops show no hysteresis. The distribution of the hysteresis is depicted in Fig. 5.38 a). The number of I-V spectra per area is plotted over their hysteresis ΔV . The number of leakage spot still visible at 2 V in a later scan of the area indicates only one hard breakdown. An analogous study conducted on the 8 nm ZAZ films after 900°C RTA yields a different distribution. For comparability all measurement parameters were the same as with

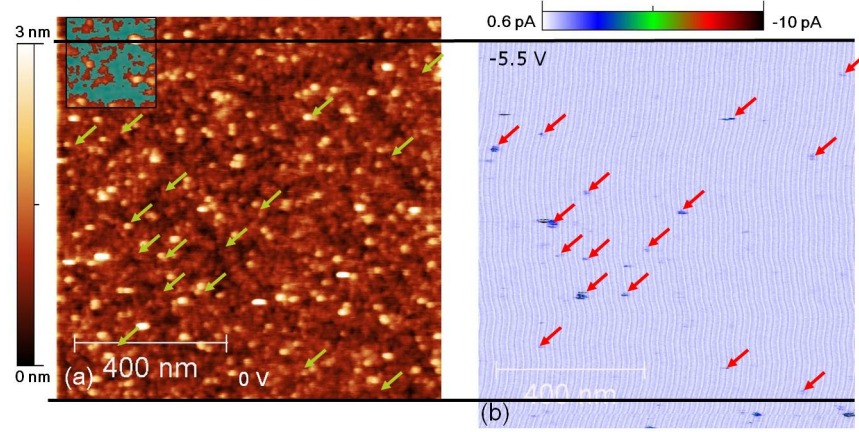


Figure 5.37: ZAZ10 after RTA: (a) CAFM topography map of the 10 nm ZAZ, film subjected to 900°C in N_2 , taken at 0 V. The hillock-like features prevail through RTA and only an incipient underlying network of trenches is visible. The inset in (a) shows this in a 74.1% threshold analysis [77]. (b) CAFM current map taken at -5.5 V (substrate injection). The false color bar is linear. Compared to Fig. 5.38 more current spots of higher current are measured.

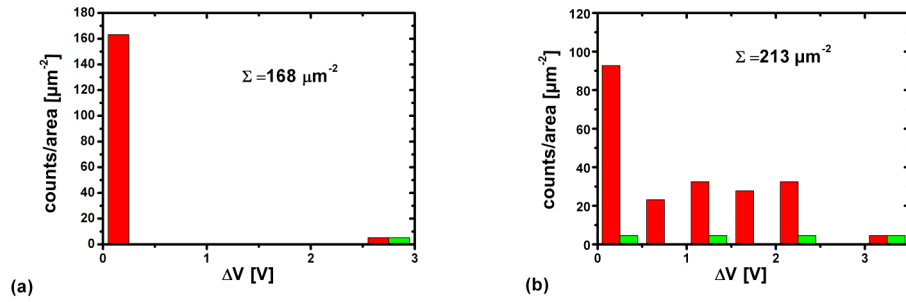


Figure 5.38: Hysteresis distribution and total leakage spot density extracted of the I-V spectra obtained on the as-deposited (a) and the annealed (b) ZAZ. The green bars indicate the fraction of leakage spots that were still visible, indicating hard breakdown, in a later scan of the area at 2 V after the acquisition of the image series.

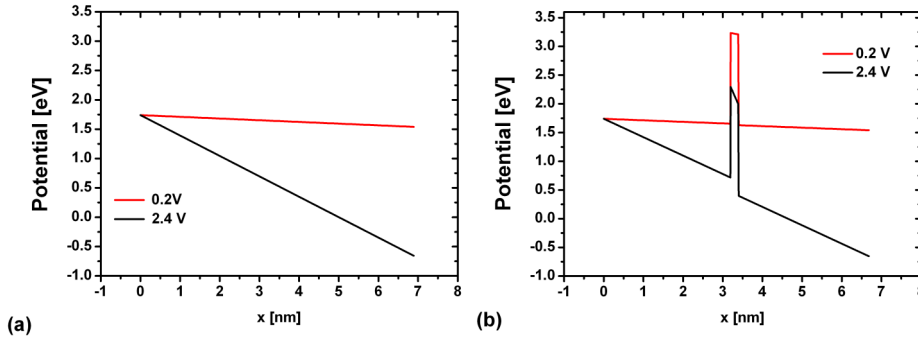


Figure 5.39: Simulated potential at 0.2 V and 2.4 V in (a) ZrO_2 and a ZAZ-stack.

the as-deposited film. The leakage spot density is larger at: $213 \mu\text{m}^{-2}$. The distribution shown in Fig. 5.38 b) depicts that the majority of I-V loops still shows no hysteresis. However the number of I-V loops exhibiting hysteresis is larger. The maximum hysteresis is at 3 V. The number of leakage spots exhibiting a hard breakdown increased.

In conclusion, these results demonstrate that keeping the films in an amorphous state during deposition is inherent for good electrical performance; while crystallization after deposition helps increasing the k-value of the films. The electrical properties can be tuned by inserting a sublayer of Al_2O_3 into the ZrO_2 . The Al_2O_3 stops crystallization during deposition by superimposing slightly different lattice parameters to the film as demonstrated by GI-XRD.

5.4 Simulation of Leakage Currents

To complete the analysis of the charge transport mechanisms in ZrO_2 and ZAZ-nanolaminate the leakage currents were simulated. The results shown in the previous section indicate a mixture of Poole-Frenkel conduction and trap-assisted tunneling. In simulation it is possible to separate between these competing mechanisms. Moreover, it is possible to elucidate the influence of

Table 5.9: Material properties used for leakage currents simulation.

Material	ZrO_2	Al_2O_3
Dielectric constant	47.0	9.5
Traplevel (center/width)	0.4 eV / 0.4 eV	0.4 eV / 0.4 eV
Effective mass	0.45	0.45
El. aff.	2.96 eV	1.38 eV

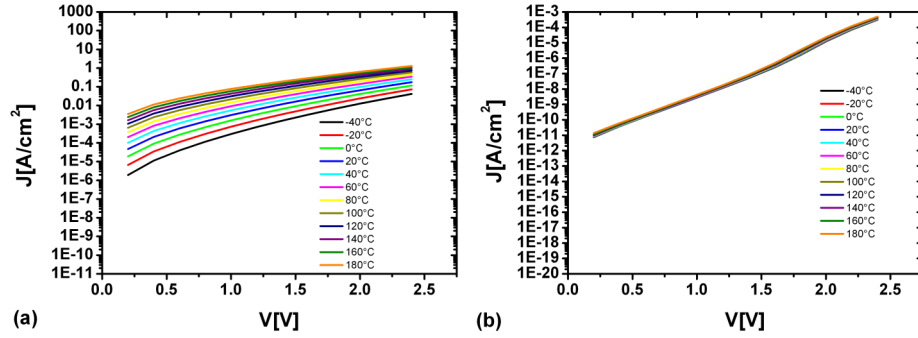


Figure 5.40: Simulation results of leakage currents in ZrO_2 : (a) Leakage currents where the second step is *Poole-Frenkel* emission. (b) Leakage currents where the second step is also tunneling.

the Al_2O_3 interlayer on the conduction band course within the nanolaminate. If materials of different dielectric constants are adjacent to each other in a nanolaminate and an external bias voltage is applied the electric field within this material stack is not constant.

This simulation calculates the potential and the leakage currents within a ZrO_2 -layer and a ZAZ-nanolaminate. It was done to compare the theoretical leakage currents of material stacks that roughly resemble the stacks studied previously. Fig. 5.39 compares the potentials across the dielectric. The film thickness entered into the simulation were the ones measured for the corresponding annealed 8 nm thick ZrO_2 - and ZAZ-films. The Al_2O_3 interlayer is 0.2 nm thick, this is thinner than the lattice constant, this estimates a deposition rate of 0.1 nm per ALD cycle. The dielectric constant used in both cases was 47 for ZrO_2 and 9.5 for Al_2O_3 . The trap levels were assumed to be gaussian distributed. The mean trap level was 0.4 eV below the conduction band and the distribution width was assumed to be 0.4 eV, this is more or less concurrent with the ones measured previously. The most important material properties for this simulation are summarized in table 5.9. Fig. 5.39 b) shows voltage drop of 0.33 V across the Al_2O_3 interlayer. This voltage drop reduces the electric field inside the two ZrO_2 -layers to $2.25 \frac{\text{MV}}{\text{cm}}$ with respect to an electric field of $3.47 \frac{\text{MV}}{\text{cm}}$ in pure ZrO_2 . However, these results are obtained by making the assumption that all layers are homogeneous and that the Al_2O_3 interlayer is closed. With an incomplete Al_2O_3 -interlayer and nanocrystalline ZrO_2 the result may differ. An unclosed Al_2O_3 -interlayer is more probable with only 2 cycles of Al. A more precise theoretical approach is followed by Jegert by using *Monte Carlo* simulations in [36, 103, 104]. Jegert arrives at the conclusion that a multistep inelastic phonon-assisted tunneling across oxygen vacancies is the dominant conduction mechanism in $\text{TiN}/\text{ZAZ}/\text{TiN}$ stacks.

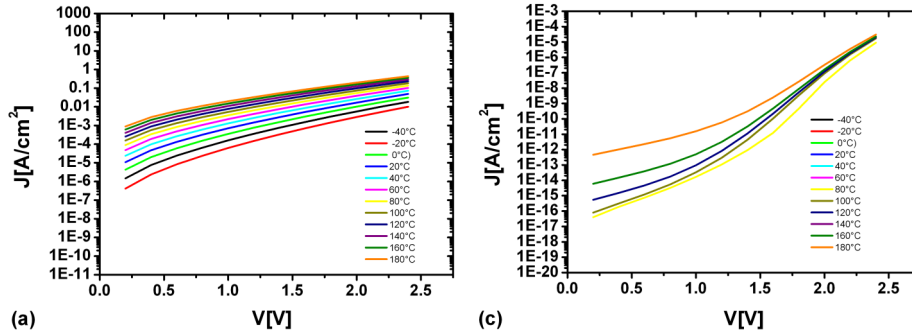


Figure 5.41: Simulation results of leakage currents in ZAZ: (a) Leakage currents where the second step is *Poole-Frenkel* emission. (b) Leakage currents where the second step is also tunneling.

The simulations were done for two scenarios: In both cases the electrons tunnel from the TiN into a trap state. In the first case, these electrons are thermally emitted from the trap state (*Poole-Frenkel* emission). In the second case the electron tunnels a second time from the trap state into the second TiN electrode. Fig. 5.40 depicts the simulated leakage currents for ZrO_2 . The current simulated using the sequential trap assisted tunneling, show no temperature dependence and are three to five orders of magnitude lower than the *Poole-Frenkel* currents. The contribution of the thermally emitted electrons is dominant for charge carrier transport.

The simulation of leakage currents in the ZAZ stack is depicted in Fig. 5.41. Fig. 5.41 a) shows that the *Poole-Frenkel* currents are one order of magnitude lower than those simulated for ZrO_2 . The I-V curves simulating the sequential tunneling process show some temperature dependence at low voltages and high temperatures.

In conclusion, the simulation shows some direct influence of the Al_2O_3 interlayer on the electron transport, due to the voltage drop in the Al_2O_3 . The lower dielectric fields in the ZrO_2 also explains lower leakage current and higher breakdown voltages and temperatures. It is also demonstrates that the influence of the simulated sequential tunneling process is almost negligible.

5.5 Discussion and Conclusion

In this chapter three types of ZrO_2 based dielectric thin-films were examined extensively. The first film is a $(\text{ZrO}_2)_{0.8}(\text{Al}_2\text{O}_3)_{0.2}$ -alloy deposited by MDB at 500°C , in order to induce crystallization. It was shown that the high deposition temperature leads to the formation of nanocrystallites within an amorphous matrix. These form during deposition and protrude the film surface. CAFM

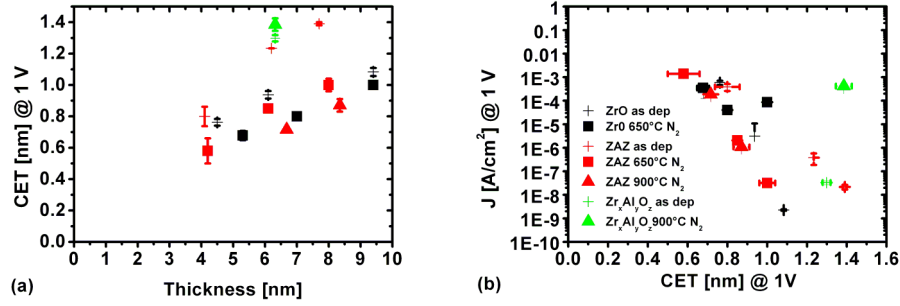


Figure 5.42: Comparison of macroscopic electrical properties of (a) ZrO₂ and (b) ZAZ before and after two different PDAs.

studies have shown these nanocrystallites to be responsible for the increased leakage currents. Local I-V spectroscopy elucidates the electronic transport properties of nanocrystallites to be similar to the ones of sites in the amorphous matrix which have been electrically stressed prior to measurement. Furthermore, a combined mechanism of trap assisted tunneling, charge trapping and thermo-chemical bond breakage was suggested to be the origin of this electrical behavior.

To further study the effects of Al incorporation into ZrO₂ two thickness series were studied: One was pure ZrO₂ the other was a ZrO₂/Al₂O₃/ZrO₂ nanolaminate, where 2 ALD cycles of Al were incorporated into the center of the stack. For reference a (ZrO₂)_{0.8}(Al₂O₃)_{0.2}-alloy was deposited. Due to the different deposition process, especially substrate temperature, this film exhibits different properties than the MDB deposited film. It showed no crystallization during deposition and crystallization temperature during RTP was significantly increased. This concurs with results reported by Zhao et al. who, among others, report on the stable and metastable immiscibility of ZrO₂ and Al₂O₃ [82–86] ZrO₂ and ZAZ films react with the TiN bottom electrode forming a TiNO interlayer during deposition. Structural analysis yields that ZrO₂ begins to form nanocrystallites when the film thickness exceeds 6 nm, the ZAZ-nanolaminates remain mainly amorphous. This effect is also visible in the electrical performance of these films as shown summarized in Fig. 5.42. The dielectric constant of ZrO₂ increases with film thickness whereas the dielectric constant of ZAZ is much more uniform for all film thicknesses. The leakage currents of all material systems are similar. Mesoscopic characterization by CAFM yields the thickest ZrO₂ to be significantly rougher than the thickest ZAZ film. In contrast to macroscopic leakage current measurement does this film exhibit large currents and more leakage current spots in CAFM measurement. This discrepancy is due to the highly local electric field under

the CAFM tip and the nanocrystallinity of the ZrO_2 film. These highly local and therefore extremely high fields induce local dielectric breakdowns preferably at defect rich locations like nanocrystallite grain boundaries. In contrast to macroscopic I-V measurement CAFM already prognosticates the films vulnerability to electrical stress after post deposition annealing. The corresponding ZAZ film exhibits very few leakage current spots. After a post deposition anneal at 900°C the very high leakage currents impede the determination of the thinner capacitor's capacitance made out of ZrO_2 . After subjecting the ZAZ films to this treatment the CET of the 6 nm and 8 nm thick films decreased significantly, but like with ZrO_2 at the cost of very high leakage currents.

To shed more light onto the the significant differences of these films that are induced by only two ALD cycles of Al an additional study of the 8 nm thick ZrO_2 and ZAZ films was conducted.

This intermediate film thickness was chosen because the electric properties of these layers range from the acceptable to the unacceptable, promising an explanation of the underlying degradation mechanisms. Variable temperature I-V hysteresis measurements were used to calculate the trap levels of ZrO_2 and ZAZ. These I-V curves exhibit a temperature dependent hysteresis. Polarization measurements were conducted confirming all films to be paraelectric. This excludes ferroelectricity as the origin for the hysteresis as in the case described by Schumacher and others [54, 98, 102, 105, 106]. The origin of the hysteresis lies in a change of transport mechanism. These mechanisms depend on the state (filled or empty), location and number of trap states. On one hand, progressive dielectric breakdown is indicated by hysteresis where the number of trap states increases. On the other hand a change of the type of transport mechanism can also be the origin of hysteresis. This can be the case when thermal emission is the more dominant mechanism on one branch of the I-V curve. Comparison of the measured trap levels can help to differentiate here. The extracted trap levels acquired at high temperatures are 0.80 eV below the conduction band edge for as-deposited ZrO_2 on the increasing branch of the I-V curve and 1.04 V on the decreasing branch. After annealing at 900°C the trap level are more shallow at 0.40 eV for the first and 0.65 eV for the second branch. The different trap levels for both branches of the I-V curve are an indicator of the detrapping of electrons by *Poole-Frenkel* emission as the bias voltage is decreased. This leads to higher leakage currents for the decreasing branch and a higher dependence on temperature. The significantly shallower trap level after the annealing step combined with the much larger leakage currents shows that tunneling is becoming more important for charge transport. The I-V results for ZAZ also exhibit temperature dependent hysteresis. For the as-deposited film the leakage currents are lower. The trap levels are 0.80 eV and 1.00 V below the conduction band, for the increasing and the decreasing branch. The film annealed at 900°C show trap levels that

are not as shallow as in ZrO_2 : 0.51 eV and 0.75 eV below the conduction band. Combined with the lower leakage current density this means that contribution of the temperature independent tunneling current to the overall leakage current is not as dominant as in ZrO_2 .

This is in agreement with the CAFM measurements, which combined with TEM and GI-XRD identify crystallite grain boundaries to be the origin of leakage currents. At these the defect density is known to be higher than in the amorphous matrix or the crystal lattice [34]. CAFM analysis also yields the leakage spot density of the as-deposited and annealed ZrO_2 and ZAZ thin-films to be $229 \mu\text{m}^{-2}$, $275 \mu\text{m}^{-2}$, $168 \mu\text{m}^{-2}$ and $213 \mu\text{m}^{-2}$, respectively. Moreover, the hysteresis analysis of local IV-curves also reveal an significant increase in large hysteresis after anneal for both materials. However, the number of leakage spots exhibiting large hysteresis is always larger for the ZrO_2 . This result is similar to macroscopic I-V curves where the hysteresis resulting from soft dielectric breakdown is also more dominant in the pure ZrO_2 films.

Recent work by Jegert et al. explains the effect of defect relaxation on leakage currents in ZAZ stacks by the use of *Monte-Carlo*-simulations [104]. Multistep inelastic phonon-assisted tunneling across oxygen vacancies are identified as the dominant conduction mechanism in $\text{TiN}/\text{ZAZ}/\text{TiN}$ stacks. Moreover, the authors formulate a model for the structural relaxation of oxygen vacancies involved where the unoccupied defect state relaxes to a energy 1.1 eV lower when being occupied. Transport occurs along such states through trap to trap tunneling. This model can also explain the temperature dependent hysteresis seen in the macroscopic I-V measurements on the 8 nm thick ZrO_2 and ZAZ films. This hysteresis is due to a larger contribution of trap-to-trap-tunneling at high temperatures. As bias voltage is decreased in the second branch of the spectra, the occupied deep trap states deliver a larger contribution of the leakage currents than in the first branch where bias voltage is increased. This effect is less pronounced for the annealed films where trap-to-trap-tunneling is the dominant transport mechanism.

To clarify the role of Al_2O_3 in the improved film stability during anneal and the increased electrical performance, a simple leakage current simulation was carried out. Here, a ZrO_2 -film and ZAZ-nanolaminate, similar to those examined experimentally, were compared. It was found that the lower dielectric constant of Al_2O_3 induced a potential drop within the film leading to lower leakage current density in ZAZ. Additionally, this potential drop is responsible for putting less electric strain on the ZrO_2 . This makes the film less prone to dielectric breakdown [78]. Nevertheless, the simulation underestimates the leakage currents in ZAZ. Especially the contribution of 2 step tunneling to the total current is grossly underestimated. It is doubtful whether the amount of Al put into the film is sufficiently large to form a closed layer of Al_2O_3 . EELS

does not confirm such a layer.

These results and the satellite peak, identified in the GI-XRD graphs, which can be associated with a strained monoclinic ZrO_2 phase lead to the conclusion that the origin of the film's improved electric properties is the interruption of crystallization during deposition and reduction of grain boundaries extending throughout the entire film. This stabilization persists even during post deposition annealing steps. Another, less aggressive, post deposition annealing step at 650°C was carried out. The 8 nm and 10 nm thick ZAZ films have a CET of 0.85 nm and 1 nm. The corresponding leakage currents are $2.1 \cdot 10^{-6} \frac{\text{A}}{\text{cm}^2}$ and $3.5 \cdot 10^{-8} \frac{\text{A}}{\text{cm}^2}$. This almost complies with the *ITRS*-requirements for 2011 of 0.8 nm CET and $1.1 \cdot 10^{-7} \frac{\text{A}}{\text{cm}^2}$.

6 Oxide Thin-films on 3D Structures

In the previous chapter CAFM was used to conduct a study of the local conductivity of planar oxide thin-films. In this chapter, a modified conductive atomic force microscopy, a scanning gate microscope, is used to study the effects of a highly local electric field being applied on an oxide thin-film covering a three dimensional semiconductor heterostructure, a silicon nanowire Schottky barrier field effect transistor (SiNWSBFET). Moreover, a proof of concept for a reprogrammable non-volatile memory device based on static band bending at the metal-semiconductor junctions will be shown. In this scheme the oxide gate dielectric of a SiNWSBFET is charged by a local top gate and the device is turned into a permanent on state. At first the role of the Schottky junction in the electronic transport of nanometer scale transistors will be elucidated. For this scanning gate microscopy is applied on a SiNWSBFET to examine the charge transport effects of a nanometer-scale local top gate during operation. The results prove experimentally that Schottky barriers control the charge carrier transport in these devices. In a second step this method is used to program the device in a non-volatile manner [107]¹.

6.1 Introduction

Complementary metal oxide semiconductor (CMOS) devices rely on the combination of n- and p-type field effect transistors (FET). These in turn rely on the n- and p- type doping of the different regions within the transistors. The exact control of the doping level becomes increasingly difficult as scaling progresses to smaller feature sizes. Moreover, semiconductor size and choice of surrounding materials have a significant influence on the activation of free charge carriers from dopant atoms in nanometer-scale semiconductors [108, 109]. Schottky field effect transistors (SBFET) were first proposed by Nishi and Sze, by replacing the heavily doped source and drain region of a conventional FET with metal electrodes, while remaining fully compliant with established CMOS processing technology [110, 111]. Over the last decade the investigation of the transport properties of nanometer scale Schottky transistors made of carbon nanotubes, graphene and semiconductor nanowires have attracted increasing

¹Copyright (2011) by the American Physical Society

attention [112–115]. The charge transport behavior strongly differs from that of conventional FETs, especially in the on- and sub-threshold regions [116]. In the on-state injection through the source Schottky junction becomes the limiting factor. In the transfer characteristics ($I_d - V_g$) the sub-threshold region can be generally sub-divided into two regions. Current injection dominated by thermionic emission over the energy barrier at low electric gate fields and currents dominated by tunneling at high fields (thin barriers) [117]. It has been shown, that scaling down the Schottky junction dimensions and semiconductor body thickness significantly enhances the tunneling current [118–120]. They are being studied extensively as building blocks for future electronic applications such as re-programmable devices and bio-sensors [115, 121]. The broad range of electronic properties unique to nanowires have recently lead to the development of nanowire based boolean logic devices [122–124]. Specifically, metal/semiconductor axial nanowire (NW) heterostructures exhibit an optimal geometry for enhancing tunneling at the Schottky electrodes [125]. Although these devices have been investigated for some time, direct experimental proof that carrier injection at the Schottky barrier limits the entire NW transport has been missing. In order to understand the working principle of SiNWSBFETs it is of immense interest to study the charge carrier transport at the Schottky junctions. In this respect Atomic Force Microscopy (AFM) and Scanning Gate Microscopy (SGM) are powerful and established tools to characterize the charge carrier transport in nanodevices [126–129]. Freitag et al. have already imaged Schottky barriers in carbon nanotube FETs by SGM.

6.2 Sample Preparation, mesoscopic and electrical Characterization

This experiment combines a working undoped SiNWSBFET with an electrical scanning probe technique to examine the effects of a nanoscale and mobile top gate on a back gated SiNWSBFET during operation.

The SiNWSBFET's core is composed of metal/Si/metal axial NW heterostructures. Such heterostructures were synthesized by a bottom-up approach. Undoped Si nanowires were grown epitaxially by chemical vapor deposition using the vapor liquid solid method, employing Au particles [121, 130, 131]. The metallic segments are chosen to be NiSi₂ and act as source and drain. These were fabricated by the thermally activated axial intrusion of nickel-silicides into the Si NW from prepatterned Ni reservoirs [131]. This creates two abrupt Schottky junctions within the NW [115, 131, 132]. Both Si and NiSi₂ parts of the NW are coated with a approximately 2 nm thick native SiO₂. These Schottky junctions can be probed individually by SGM using a conductive AFM tip to bend the conduction and valence bands locally at the metal-semiconductor junction. The SGM used in this work is an AFM operated in contact mode,

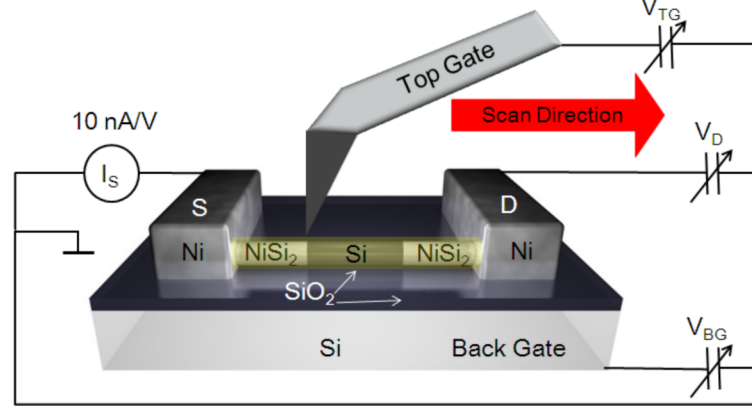


Figure 6.1: Schematic of the SGM setup. The NiSi_2 electrodes act as source and drain. The Si substrate is the back gate and the conductive AFM Tip is the scanning top gate [107].

where two probe tip micromanipulators are positioned under the AFM head along with the conductive AFM tip. One probe contacts the source, the other the drain electrode. The conductive tip also acts as a local top gate. Consequently the source current I_S is measured in dependence of the top gate position, by scanning across the nanowire surface at a fixed top gate V_{TG} and drain V_D bias. To simplify the upcoming discussion the electrode connected to the current amplifier is defined as source and the electrode set to potential is defined as drain. Figure 6.1 illustrates the I_S measurement relative to a common ground while V_D , V_{BG} and V_{TG} are set relative to this common ground. In this scheme the second probe acts as contact to the drain, the chuck is connected to the back gate while the conductive AFM tip is acting as a mobile nano-scaled top gate. The contact area of the highly doped full-diamond tip is estimated to be 100 nm^2 [107].

6.3 Results and Discussion

The position and orientation of the SiNWSBFET were acquired by scanning electron microscopy (SEM) and AFM. SEM analysis shows silicidation at both NW ends, resulting in abrupt interfaces and therefore sharp Schottky junctions. Moreover, a second SEM analysis in Fig. 6.2 a), done after SGM measurement, yields an intact NW, showing that SGM has not damaged the NW. The AFM topography map in Fig. 6.2 b) matches the SEM micrograph. The NW appears broader due to the fact that the AFM map is the convolution of the AFM tip shape and the sample surface. The difference between the Si and NiSi_2 segments is also visible. This is the result of the increased NW diameter depicted by the profiles in Fig. 6.2 c). Profiles 2 and 3 are taken of the Si NW

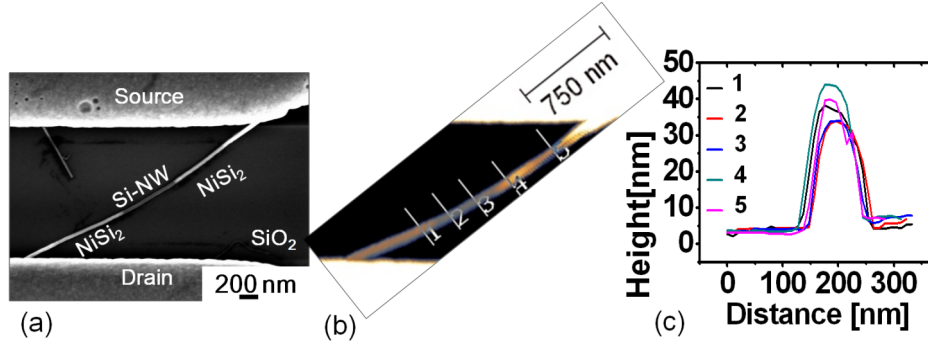


Figure 6.2: (a) SEM micrograph of the NW. Source and drain Ni-contacts are visible on top and bottom of the image. The NiSi₂ parts of the NW are brighter than the Si part. Another nanowire on the top left is not contacted to both electrodes and therefore not subject of this work. (b) AFM topography map of the same NW. (c) Profiles 1 - 5 correspond to the positions in (b) and show different diameters [107].

and 1, 4 and 5 are taken at the NiSi₂ source and drain. Based on this finding, it is possible to locate the exact position of the junction in AFM morphology maps.

The device was thereafter characterized electrically in a shielded probe station using a semiconductor characterization system. The transfer characteristics were measured by contacting source, drain and back gate. The latter via the probe station chuck. First, a drain bias of $V_D = -1.0$ V was applied and the back gate bias (V_{BG}) was swept between -3.0 V and 3.0 V while monitoring the drain current I_D . The transfer characteristics acquired in the probe station and shown in Fig. 6.3 a) exhibit a clear p-type transistor behavior [115]. This p-type behavior in an intrinsic Si NW is explained by the fact that holes are being injected more effectively through the Schottky junction than electrons [116]. Figure 6.3 b) depicts schematically how conduction and valence band are fixed at the metallurgical junction and bent by the electric field induced by back gate bias voltage. This enables electron injection at the left Schottky junction [113, 121, 133]. The on-off ratio is six orders of magnitude. To verify the similarity of the SGM setup and the conventional testing setup this experiment was repeated in the SGM. Here, V_D was set to -1.0 V. V_{BG} was swept between -3.0 V and 3.0 V. The transfer characteristics acquired in the SGM setup (Fig. 6.3 c)) without an active top gate comply with the ones acquired in the probe station, with respect to the different current measurement. The amplifier reaches its current limit at 10 nA. Fig. 6.3 d) shows the transfer characteristics measured after SGM measurements. The device still shows switching behavior. The shift in the curves might be due to measurement in ambient conditions

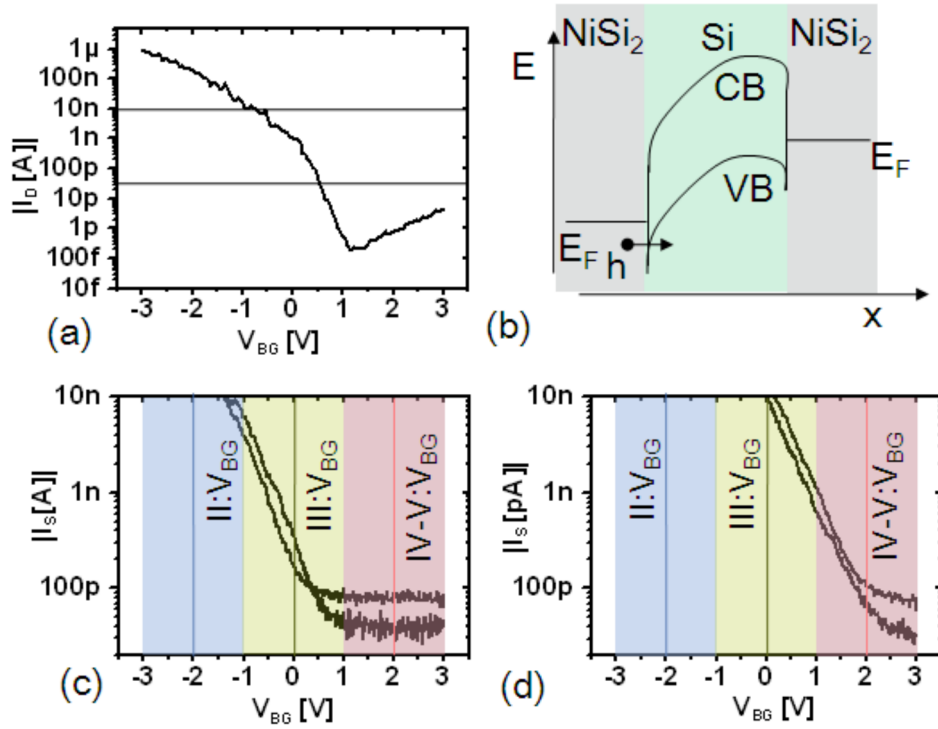


Figure 6.3: (a) Transfer characteristics of the SiNWSBFET with $V_D = -1$ V measured on a probe station. The horizontal lines mark the current range of the SGM setup. (b) Band diagram schematic of hole tunneling through the Schottky junction at an applied back gate bias. (c) and (d) The transfer characteristics measured in the SGM setup under the same conditions before and after SGM. The shaded areas mark the gate bias range affected by the top gate bias during the corresponding SGM-measurement (II - V) at the V_{BG} marked by the corresponding line [107].

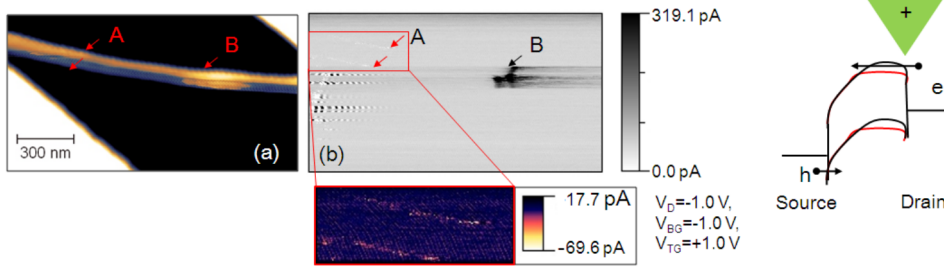


Figure 6.4: (a) Topography map of the Si NW. The slight distortion of the NW is caused by the NW being moved by the tip. (b) Current map of the same area. The area marked with a red rectangle was enlarged and contrast was adjusted to display negative currents. The band diagram schematically depicts local band bending with just the back gate in black and with the additional top gate over the right Schottky junction in red [107].

and slight surface manipulation by the biased tip. Afterwards the AFM tip was set on the sample surface and scanning began. The source current was constantly monitored during scanning. In this way, a rupture of the NW, caused by the scanning motion of the AFM tip, can be detected immediately. But more importantly, any perturbation of the on- or off-state of the device by the scanning top gate could be detected. The nanoscopic electrical properties of the NW were examined by repeatedly scanning the NW at different top and back gate biases. The scan-direction is always parallel to the NW to minimize mechanical stress. The first SGM current map was acquired at $V_D = -1.0$ V, $V_{BG} = -1.0$ V and $V_{TG} = 1.0$ V.

In Fig. 6.4 SGM morphology and current maps yield a correlation between the location of the source Schottky junction and an area of high positive current. Currents at the source Schottky junction cannot be observed. Only at some sites at the silicide segment's facets leakage currents can be observed (see inset). Here, the native oxide is penetrated due to the excessive force between tip and Ni or NiSi₂-NW edge during scanning. These leakage currents are significantly lower in absolute value compared to currents at the source Schottky junction and of opposite sign. Moreover, there are artifacts of high noisy currents when the AFM tip connects with the left(source) Ni electrode which is directly connected to the amplifier. The switching into the on-state of the device when the biased tip is above the right Schottky junction is caused by highly local band bending of the Si conduction and valence bands. The band diagram sketch next to the current map illustrates the role of localized band bending induced by the top gate in carrier transport. In case of a positively biased tip as in Fig. 6.4 b), where the tip is above the right Schottky junction, the electric field of the tip pushes the conduction and valence bands down locally at the Schottky junction. Electrons can now be injected through the right barrier and

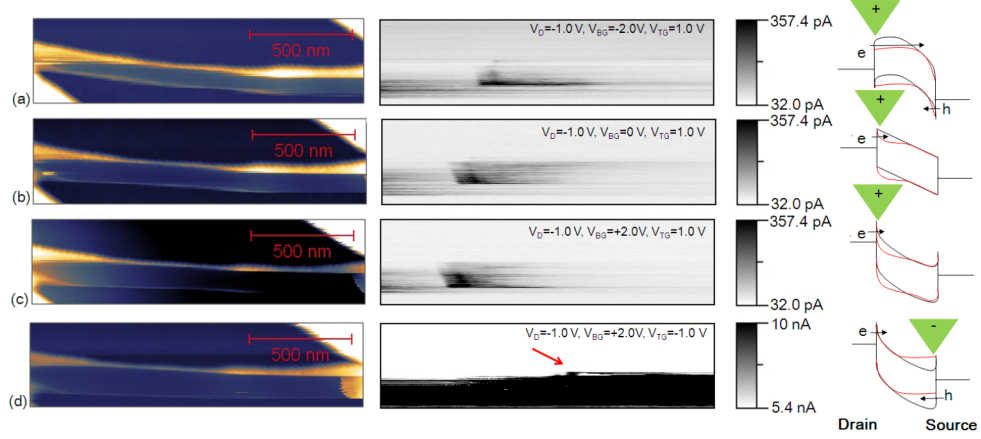


Figure 6.5: SGM maps after interchanging source and drain. Left: Topography map of the Si NW. Right: Current map of the corresponding area. The band diagrams schematically depict the band bending with just a BG (black) and with an additional TG (red) over the corresponding Schottky junction [107].

contribute to the current in addition to the holes tunneling through the left Schottky junction. Afterwards, source and drain contact were interchanged. Again a SGM current map was acquired at different V_D , V_{BG} and V_{TG} .

To verify the transistors symmetry, further SGM morphology and current maps, with interchanged source and drain, are shown in Fig. 6.5 a). Again the device is switched into the on-state when the tip is on top of the drain junction. In Fig. 6.5 b), at $V_{BG}=0$ V, the current is also increased when the AFM tip is just on top of the source Schottky junction, indicating that band bending is similar to Fig. 6.5 a). In Fig. 6.5 c) VI., at $V_{BG}=2.0$ V, the potential induced by the AFM tips also pushes down the bands at the source Schottky junction when the tip is directly on top of the junction, indicating that electrons are still the main contributor of current at the Schottky junction. These results show that electron injection via the top gated Schottky junction dominates and that the device is symmetric. In Fig. 6.5 d) the top gate bias is negative and the source Schottky junction is visible for a few scanlines (see red arrow), this on-state persists throughout the rest of this image acquisition. In fact it persists even for following images and is showing larger positive currents than the current maps (a-c). The drain Schottky junction is no longer visible. When the tip is positioned above the source Schottky barrier, conduction and valence band are pushed up and now the hole current is added to the electron current resulting in an increased total current. After a few scanlines the transistor switches to a permanent on-state. This effect lasts for the entire scan resulting in large currents for the remainder of the current map. Moreover, this behavior is persistent throughout the following current maps when image acquisition parameters remain unchanged. The neg-

Table 6.1: List of current maps, acquisition parameters used and the summarized results.

	V_{DS} [V]	V_{BG} [V]	V_{TG} [V]	I[nA]	Location
Fig. 6.4 b)	-1.0	-1.0	+1.0	-0.82	drain
Source and drain interchanged					
Fig. 6.5 a)	-1.0	-2.0	+1.0	0.43	drain
Fig. 6.5 b)	-1.0	0	+1.0	0.35	drain
Fig. 6.5 c)	-1.0	+2.0	+1.0	0.45	drain
Fig. 6.5 d)	-1.0	+2.0	-1.0	>10	source

active tip induces a negatively charged layer in the native oxide which has the same effect as the biased top gate. Accordingly, the transistor behavior can be programmed in a non-volatile manner by charging the SiO_2 above the Schottky junction. After changing image acquisition parameters the original p-type transistor behavior is achieved again as depicted in Fig. 6.3 d). This result is a proof of concept for a non-volatile memory device based on local band bending induced by charges trapped in a functionalized oxide layer above the Schottky junction. These results are summarized in Tab. 6.1. This proof-of-concept for nonvolatile programming gives way to a one-transistor (1T) non-volatile memory cell.

By proving that the Schottky junctions are the area most sensitive to a local electric field these results are of considerable insight into charge carrier transport mechanisms in metal-semiconductor junctions in general, for example in carbon nanotubes and graphene ribbons. These findings yield more specific implications on the optimization of biosensors based on SiNWSBFET. In these nanodevices, receptors are typically placed directly above the active region where they can bind charged target bio-molecules, shifting the threshold voltage [134]. The results show that the optimal placement of receptors in nanowire SBFET biosensors is in direct vicinity of the Schottky junctions due to their high sensitivity to electric fields.

6.4 Conclusion

Scanning gate microscopy was employed to prove that the Schottky junctions control the charge carrier transport in nanometer scale Schottky FETs. Moreover was it demonstrated that it is possible to program the conductance of a SiNWSBFET in a nonvolatile manner by charging the oxide directly at the Schottky junction.

7 Summary and Outlook

In the course of the extreme downscaling of device dimensions in semiconductor industry the continuing demand for novel dielectric materials has arisen. As HfO_2 is replaced by materials yielding higher dielectric constants more constraints for these novel materials appear. These dielectric thin-films do not have a sufficiently high dielectric constant when remaining amorphous. The obvious alternative, single crystalline, epitaxial films are possible but not practical in the established CMOS production processes. This is due to the fact that the epitaxial deposition of strain free dielectric thin-films on three dimensional structures is not yet established in the CMOS production. The compromise are nanocrystalline dielectric thin films. In these however the increased capacitance is bought at the cost of high leakage currents.

At the same time new methods of materials deposition, processing and characterization are developed or adapted for advanced materials design. CAFM is such a valuable characterization tool. By combining leakage current measurements with the high spatial resolution of contact mode AFM, this tool is suitable to aid in developing a nanocrystalline material with a sufficiently high dielectric constant while at the same time maintaining reasonably low leakage currents. This optimization process is the core of this work.

In this work CAFM was established as a tool for leakage current characterization with a high spatial resolution. In the course of this process a method of acquiring highly local I-V spectra through current extraction from series of current maps was developed. This was used to characterize dielectric thin films on the nanometer scale. Additionally, the advantages and limitations of CAFM in comparison to macroscopic electric characterization were elucidated. This revealed not only that the spatial information given by CAFM cannot be obtained by macroscopic I-V curves. But it was also demonstrated that by using CAFM it is possible to study the influence of bottom electrode properties, conduction band offset and material composition on leakage currents and charge trapping behavior: A high CB offset can only be of value when the BE is sufficiently smooth. The influence of a lower CB offset is elucidated by CAFM even when macroscopic measurements do not yield this information. These results imply that multiple functionalities of oxides can be tuned by the choice of electrode material and Ti intermixture in the dielectric. This study also demonstrates that electronic trap states play different roles in different material stacks. When the CB offset is low, as in the case of a $\text{TiN}/\text{HfTiO}_3$ interface, the trap states generated by electrical stress

act as traps and effectively lower conductivity. When the CB offset is higher, as in the case of the Ru/HfTiO₃ interface, they effectively act as stepping stones for charge carrier transport and increase conductivity in regions where they were previously generated by electrical stress.

In a further step these findings were used in an integrated effort to elucidate the influence of Al₂O₃-incorporation on the physical and electrical properties of ZrO₂. One way to induce the required crystallization in dielectric thin-films is to deposit them at high temperatures. In this case this was done using MBD. Here the deposited material was co-evaporated from solid sources using e-beam evaporators.

By incorporating 20% of Al₂O₃ into ZrO₂ at a deposition temperature of 500°C nanocrystallites form. These are embedded in an amorphous matrix, some of these nanocrystallites extend from the bottom electrode to the top of the dielectric film. These crystallites are the origin of leakage currents which occur along their grain boundaries. In-depth CAFM studies have shown these crystallites to have similar electrical properties as locations in the amorphous matrix which have been subject to soft dielectric breakdown.

A different approach was followed with the thin-films deposited by ALD. Here the layers were supposed to remain amorphous during deposition at 270°C. The crystallization was intended to be induced by a post deposition annealing step. However, films thicker than 5 nm did not remain amorphous, they formed crystallites during deposition. This resulted in increased capacitance for thicker layer. Macroscopic I-V measurements show no significant effect of the crystallization on the leakage current density. Mesoscopic current analysis by CAFM however, reveals increased currents for thicker, more crystalline films. These currents are induced by a cascade of soft dielectric breakdowns along existing trap states. After a one minute PDA at 900°C in N₂, the crystallization progress leads to a complete electrical degradation of the film. A later analogous more conservative post deposition anneal at 650°C also induced crystallization which leads to a dielectric constant of 47. But the leakage currents are also increased, especially for the thickest film.

The atomic layer deposition of ZrO₂ and Al₂O₃ with a cycle ratio of 5:1 lead to the suppression of crystallization during deposition and to a significant increase of the crystallization temperature during post deposition annealing. Prior to rapid thermal annealing this leads to a the suppression of leakage currents compared to pure ZrO₂. However, the dielectric constant is lower. A post deposition rapid thermal annealing process at 900°C induced crystallization and increase leakage currents but no improved dielectric constant was achieved. In a different approach a sublayer of Al₂O₃ was deposited in the center of the ZrO₂ film. In this nanolaminate the formation of crystallites

during deposition was suppressed effectively in comparison to ZrO_2 . The incorporation of only 2 ALD-cycles of Al also leads to a structural stabilization of the ZAZ stack during rapid thermal annealing at 900°C . The CET is effectively reduced but the leakage currents are still high. A leakage current analysis on the mesoscopic scale by CAFM yields crystallite grain boundaries to be responsible for these high leakage currents. In CAFM current maps obtained on ZrO_2 and ZAZ, these grain boundaries exhibit higher currents. Local I-V curves show ZrO_2 to be more vulnerable to soft dielectric breakdown than ZAZ.

Variable temperature I-V hysteresis measurements were used to calculate the trap levels of ZrO_2 and ZAZ. These I-V curves exhibit a temperature dependent hysteresis. Polarization measurements were conducted confirming all films to be paraelectric. This excludes ferroelectricity as the origin for the hysteresis as in the case described by Schumacher and others [54, 98, 106]. The origin of the hysteresis lies in a change of conduction mechanism. These mechanisms depend on the state (filled or empty), location and number of trap states. On one hand, progressive dielectric breakdown is indicated by hysteresis where current jumps. The number of trap states increases. On the other hand can a change of the type of transport mechanism also be the origin of hysteresis. This can be the case when thermal emission is the more dominant mechanism on one branch of the I-V curve. Comparison of the measured trap levels can help to differentiate here. The trap levels acquired for high temperatures extracted are 0.80 eV with below the conduction band edge for as-deposited ZrO_2 on the increasing branch of the I-V curve and 1.04 V on the decreasing branch. After annealing at 900°C the trap levels are more shallow at 0.40 eV for the first and 0.65 eV for the second branch. The different trap levels for both branches of the I-V curve is an indicator of the detrapping of electrons as the bias voltage is decreased. This leads to higher leakage currents for the decreasing branch and a higher dependence on temperature. The significantly shallower trap level after the annealing step combined with the much larger leakage currents shows that tunneling is becoming more important for charge transport. This complies with the increased leakage spot density obtained by CAFM. Which, combined with TEM identify crystallite grain boundaries to be the origin of leakage currents. In the 8 nm ZAZ films the trap levels are 0.80 eV and 1.00 V below the conduction band, for the increasing and the decreasing branch. The film annealed at 900°C shows trap levels that are not as shallow as in ZrO_2 : 0.51 eV and 0.75 eV below the conduction band. This means that the temperature independent tunneling is not as important for charge transport. This is in agreement with the CAFM measurements which confirm a much lower leakage spot density for ZAZ. Moreover, it is important to mention that the density of leakage spots with large hysteresis in their local I-V curves also concur with these deductions. The results can be partially

explained by structural relaxation of defect states suggested by Jegert et al. which identifies trap-to-trap-tunneling as the dominant transport mechanism in nano-crystalline ZAZ thin-films [104]. The mesoscopic leakage current analysis through local I-V hysteresis loops show leakage spot densities of the as-deposited and annealed ZrO_2 and ZAZ thin-films to be $229 \mu\text{m}^{-2}$, $275 \mu\text{m}^{-2}$, $168 \mu\text{m}^{-2}$ and $213 \mu\text{m}^{-2}$, respectively. The hysteresis analysis of local IV-curves also reveal an significant increase in large hysteresis after anneal for both materials. The number of leakage spots exhibiting large hysteresis is always larger for the ZrO_2 . This result is similar to macroscopic I-V curves where the hysteresis resulting from soft dielectric breakdown is also more dominant in the pure ZrO_2 films. In an alternative RTP experiment the anneal temperature was reduced to 650°C . This reduced the CET in ZAZ films. The 8 nm and 10 nm thick ZAZ films have a CET of 0.85 nm and 1 nm. The corresponding leakage currents are $2.1 \cdot 10^{-6} \frac{\text{A}}{\text{cm}^2}$ and $3.5 \cdot 10^{-8} \frac{\text{A}}{\text{cm}^2}$.

Simulations were undertaken to clarify the role of Al_2O_3 in the improved film stability during anneal and the increased electrical performance. A ZrO_2 -film and a ZAZ-nanolaminate, similar to those examined experimentally, were compared. The lower dielectric constant of Al_2O_3 induced a potential drop within the film leading to lower leakage current density in ZAZ. Additionally, this potential drop is responsible for putting less electric strain of the ZrO_2 . This makes the film less prone to dielectric breakdown. But the simulation underestimates the leakage currents in ZAZ and it is doubtful whether the amount of Al put into the film is sufficiently large to form a closed layer of Al_2O_3 . EELS does not confirm such a layer. Comparison of leakage current simulations and variable temperature I-V spectroscopy shows that the contribution of sequential trap assisted tunneling to the total leakage current is larger in annealed ZrO_2 than in annealed ZAZ.

These results demonstrate that the inclusion of only two ALD cycles into the center of the ZrO_2 thin-film destabilizes the cubic/tetragonal phases. This effectively reduces the formation of crystallite grain boundaries during deposition which in turn leads to less leakage currents. At the same time, the crystallization of the thin-films is sufficient to maintain a high dielectric constant.

In summary, CAFM was validated as novel and powerful method for leakage current measurement with a high spatial resolution and was successfully introduced into an industrially relevant materials characterization and optimization scheme. Using this scheme it was possible to gain substantial insight on the materials properties of ZrO_2 and to modify ZAZ thin-films to significantly improve their suitability for the application in the DRAM capacitor.

The materials studied in this work are already in production as an insulating dielectric layer in DRAM capacitors of the sub 50 nm technology nodes, especially the ZAZ nano-laminates. The findings of this work however have

implications that exceed the properties of Zr based oxides and nano-laminates based on these materials. The thermal stability of dielectric thin film laminates, and the suppression of leakage currents in them can be conveyed to the other oxides as well. These can be Ti based perovskites like SrTiO_3 and CaTiO_3 with an even higher dielectric constant exceeding 100. These materials are also subject to crystallization during deposition [45, 135–137]. The possibility to suppress this by depositing a nano-laminate is another promising approach towards the industrial application of higher k dielectrics. The fact that the inclusion of only a sub-layer of Al already has significant implications on the leakage current becomes even more important as film thicknesses approach 4.5 nm for <20 nm technology nodes. In these films there is no more room for a closed Al_2O_3 -interlayer. The inclusion of only a few Al atoms, just enough to interrupt crystallization might already improve leakage current behavior. Another possible application is the examination of resistive switching materials like Nb_2O_5 where highly local conductive filaments can be used to establish discrete levels of conductivity in a novel type of device called memristor [138, 139].

The most powerful asset of CAFM is, as with any SPM method, the high spatial resolution. In this work the highly local morphological information of AFM is supplemented by the ability performing of highly local electrical characterization of planar thin films. This method can also be applied to three dimensional nanostructures like nanowires or even nanowire field effect transistors. Here a different variant of CAFM is used named Scanning Gate Microscopy (SGM) [126–129]. With this setup it was possible to identify metal/semiconductor junctions as the parts of the nanowire which are most sensitive to external electric fields. The back gate is biased at -1 V inducing hole injection into the nanowire. When the positively biased tip is positioned above the right Schottky junction the electric field of the tip pushes the conduction and valence bands down locally at the Schottky junction. Electrons can now be injected through the right barrier and contribute to the current in addition to the holes injected through the left Schottky junction. It is also possible to charge the oxide surrounding the nanowire exactly above the metal semiconductor junction rendering the transistor in a permanent ON-state [107]. Moreover, given more current transducers in the experimental setup it would be possible to measure the top gate leakage currents as well. This allows the complete nanoscaled electrical characterization of an Silicon nanowire Schottky barrier transistor including the characterization of its insulating shell. The characterization of alternative dielectrics such as HfO_2 or ZrO_2 can increase the charge trapping capability and eventually improve non-volatile programming. Additionally, the ferroelectric properties of doped HfO_2 thin-films, discovered only recently, can be studied on the device in operation [98, 105, 140, 141]. A ferroelectric triple gate Silicon nanowire Schottky barrier transistor is a very interesting approach towards a 1T non-volatile memory cell. Since this

device is programmed not by relatively slow charge trapping but by polarization switching the programming times for this device is in the nanosecond regime [141–144].

8 Appendix

Appendix A

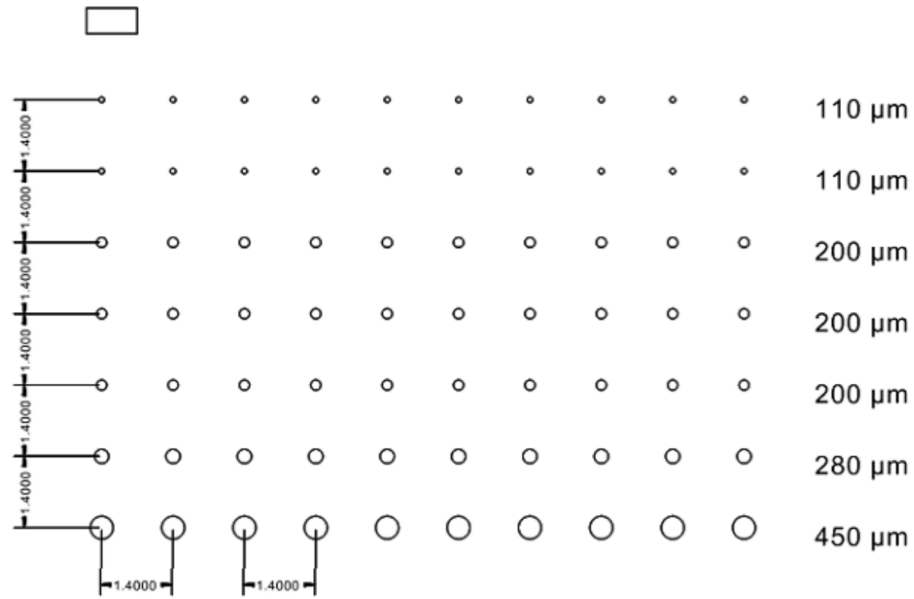


Figure 8.1: Schematic of the shadow mask including the hole diameter (right). And the inter hole distance in x and y direction (bottom and left).

Appendix B

Evaluation of non-linear *Arrhenius* plots:

Consider two competing processes A and B , with the corresponding activation energies E_A and E_B .

$$A = A_0 e^{\frac{-E_A}{k_b T}} \quad (8.1)$$

$$B = B_0 e^{\frac{-E_B}{k_b T}} \quad (8.2)$$

Both contribute to C as competitors:

$$C = A + B = A_0 e^{\frac{-E_A}{k_b T}} + B_0 e^{\frac{-E_B}{k_b T}} \quad (8.3)$$

$$\text{where } B_0 = 1 - A_0 \text{ and } 0 \leq A_0 \leq 1 \quad (8.4)$$

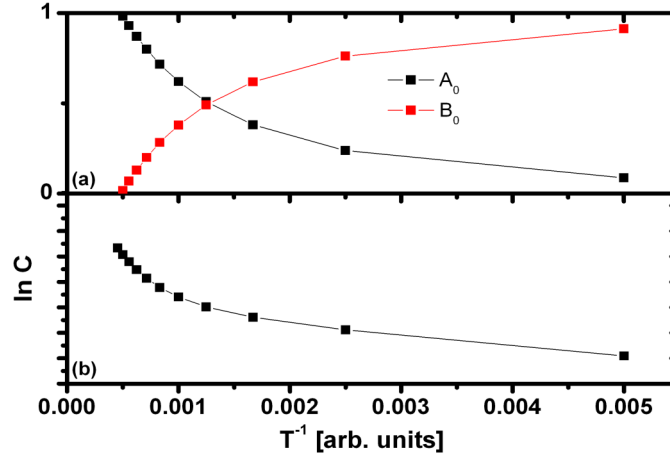


Figure 8.2: (a) Fraction of each process plotted over temperature. (b) *Arrhenius* plot of C.

The *Arrhenius* plot of C is depicted in Fig: 8.2. It demonstrates how the *Arrhenius* plot of the sum of two competing processes, with different activation energies, is curved in the temperature regime where the two processes compete [101].

Bibliography

- [1] R. Waser (ed.). *Nanoelectronics and Information Technology*. Wiley (2005).
- [2] T. Schloesser, F. Jakubowski, J. v. Kluge, A. Graham, S. Slesazeck, M. Popp, P. Baars, K. Muemmler, P. Moll, K. Wilson, A. Buerke, D. Koehler, J. Radecker, E. Erben, U. Zimmermann, T. Vorrath, B. Fischer, G. Aichmayr, R. Agaiby, W. Pamler, T. Schuster, W. Bergner, and W. Mueller. *Proc. IEEE Int. Electron Devices Meeting IEDM 2008*, 1–4 (2008).
- [3] S. K. Kim, S. W. Lee, J. H. Han, B. Lee, S. Han, and C. S. Hwang. *Advanced Functional Materials*, **20** (2010) 2989.
- [4] G. E. Moore. *Electronics*, **38** (1965) 114.
- [5] J. Lutzen, A. Birner, M. Goldbach, M. Gutsche, T. Hecht, S. Jakschik, A. Orth, A. Sanger, U. Schroder, H. Seidl, B. Sell, and D. Schumann. *Proc. Digest of Technical Papers VLSI Technology 2002 Symp*, 178–179 (2002).
- [6] D.-S. Kil, H.-S. Song, K.-J. Lee, K. Hong, J.-H. Kim, K.-S. Park, S.-J. Yeom, J.-S. Roh, N.-J. Kwak, H.-C. Sohn, J.-W. Kim, and S.-W. Park. *Proc. Digest of Technical Papers VLSI Technology 2006 Symp*, 38–39 (2006).
- [7] M. Bohr, R. Chau, T. Ghani, and K. Mistry. *Spectrum, IEEE*, **44** (2007) 29 .
- [8] *International Technology Roadmap for Semiconductors*, <http://www.itrs.net>.
- [9] J. Kittl, K. Opsomer, M. Popovici, N. Menou, B. Kaczer, X. Wang, C. Adelman, M. Pawlak, K. Tomida, A. Rothschild, B. Govoreanu, R. Degraeve, M. Schaekers, M. Zahid, A. Delabie, J. Meersschaut, W. Polspoel, S. Clima, G. Pourtois, W. Knaepen, C. Detavernier, V. Afanas'ev, T. Blomberg, D. Pierreux, J. Swerts, P. Fischer, J. Maes, D. Manger, W. Vandervorst, T. Conard, A. Franquet, P. Favia, H. Bender, B. Brijs, S. V. Elshocht, J. V. H. M. Jurczak, and, and D. Wouters. *Microelectronic Engineering*, **86** (2009) 1789.

- [10] M. Pawlak, M. Popovici, J. Swerts, K. Tomida, M.-S. Kim, B. Kaczer, K. Opsomer, M. Schaekers, P. Favia, H. Bender, C. Vrancken, B. Govoreanu, C. Demeurisse, W.-C. Wang, V. Afanas'ev, I. Debusschere, L. Altimime, and J. Kittl. *Electron Devices Meeting (IEDM), 2010 IEEE International*, 11.7.1 –11.7.3 (2010).
- [11] X. Zhao and D. Vanderbilt. *Physical Review B*, **65** (2002) 075105.
- [12] G.-M. Rignanese, F. Detraux, X. Gonze, and A. Pasquarello. *Physical Review B*, **64** (2001) 134301.
- [13] P. D. Wolf, E. Brazel, and A. Erickson. *Materials Science in Semiconductor Processing*, **4** (2001) 71 .
- [14] O. Bierwagen, L. Geelhaar, X. Gay, M. Piešins, H. Riechert, B. Jobst, and A. Rucki. *Applied Physics Letters*, **90** (2007) 232901.
- [15] V. Yanev, M. Rommel, M. Lemberger, S. Petersen, B. Amon, T. Erlbacher, A. J. Bauer, H. Ryssel, A. Paskaleva, W. Weinreich, C. Fachmann, J. Heitmann, and U. Schroeder. *Applied Physics Letters*, **92** (2008) 252910.
- [16] K. McKenna, A. Shluger, V. Iglesias, M. Porti, M. Nafria, M. Lanza, and G. Bersuker. *Microelectronic Engineering*, **88** (2011) 1272 . Proceedings of the 17th Biennial International Insulating Films on Semiconductor Conference, 17th Biennial International Insulating Films on Semiconductor Conference.
- [17] W. Besling, E. Young, T. Conard, C. Zhao, R. Carter, W. Vanderhorst, M. Caymax, S. D. Gendt, M. Heyns, J. Maes, M. Tuominen, and S. Haukka. *Journal of Non-Crystalline Solids*, **303** (2002) 123 .
- [18] K. H. Kuesters, M. F. Beug, U. Schroeder, N. Nagel, U. Bewersdorff, G. Dallmann, S. Jakschik, R. Knoefler, S. Kudelka, C. Ludwig, D. Manger, W. Mueller, and A. Tilke. *Advanced Engineering Materials*, **11** (2009) 241.
- [19] M.-S. Kim, M. Popovici, J. Swerts, M. A. Pawlak, K. Tomida, B. Kaczer, K. Opsomer, M. Schaekers, H. Tielens, C. Vrancken, S. Van Elshocht, I. Debusschere, L. Altimime, and J. A. Kittl. *Proc. 3rd IEEE Int. Memory Workshop (IMW)*, 1–4 (2011).
- [20] M. A. Pawlak, M. Popovici, J. Swerts, K. Tomida, M.-S. Kim, B. Kaczer, K. Opsomer, M. Schaekers, P. Favia, H. Bender, C. Vrancken, B. Govoreanu, C. Demeurisse, W.-C. Wang, V. V. Afanas'ev, I. Debusschere, L. Altimime, and J. A. Kittl. *Proc. IEEE Int. Electron Devices Meeting (IEDM)* (2010).

- [21] N. Menou, X. P. Wang, B. Kaczer, W. Polspoel, M. Popovici, K. Opsomer, M. A. Pawlak, W. Knaepen, C. Detavernier, T. Blomberg, D. Pierreux, J. Swerts, J. W. Maes, P. Favia, H. Bender, B. Brijs, W. Vandervorst, S. Van Elshocht, D. J. Wouters, S. Biesemans, and J. A. Kittl. *Proc. IEEE Int. Electron Devices Meeting IEDM 2008*, 1–4 (2008).
- [22] H. J. Cho, Y. D. Kim, D. S. Park, E. Lee, C. H. Park, J. S. Jang, K. B. Lee, H. W. Kim, Y. J. Ki, I. K. Han, and Y. W. Song. *Solid-State Electronics*, **51** (2007) 1529 . Special Issue: Papers Selected from the 36th European Solid-State Device Research Conference - ESSDERC'06.
- [23] H. R. Huff and D. C. Gilmer (eds.). *High Dielectric Constant Materials*. Springer (2005).
- [24] S. M. Sze. *Semiconductor Devices: Physics an Technology*. John Wiley (2002).
- [25] S. M. Sze. *Physics of Semicondor Devices*. Wiley and Sons Inc. (1981).
- [26] W. Pies and A. Weiss. *Landolt-Börnstein - Group III Condensed Matter*, vol. 7b1, –.
- [27] W. Pies and A. Weiss. *Landolt-Börnstein - Group III Condensed Matter*, vol. 7b1, –.
- [28] R. P. Feynman. *The Feynman Lectures on physics 'Mainly Electromagnetism and Matter'*. Addison-Wesley (1989).
- [29] R. Schumacher and R. Waser. *Integrated Ferroelectrics*, **22** (1998) 109.
- [30] L. A. Dissado and R. Hill. *Nature*, **279** (1979) 685.
- [31] J. Robertson. *Reports on Progress in Physics*, **69** (2006) 327.
- [32] R. H. French, S. J. Glass, F. S. Ohuchi, Y. N. Xu, and W. Y. Ching. *Physical Review B*, **49** (1994) 5133.
- [33] J. Robertson, K. Xiong, and B. Falabretti. *Device and Materials Reliability, IEEE Transactions on*, **5** (2005) 84 .
- [34] G. Lucovsky, C. Hinkle, C. Fulton, N. Stoute, H. Seo, and J. Lüning. *Radiation Physics and Chemistry*, **75** (2006) 2097 . Proceedings of the 20th International Conference on X-ray and Inner-Shell Processes - 4-8 July 2005, Melbourne, Australia, Proceedings of the 20th International Conference on X-ray and Inner-Shell Processes.

- [35] O. Blank. *Charakterisierung und Modellierung der Leckstrommechanismen in modernen DRAM high-k Materialien*. Ph.D. thesis, Universität der Bundeswehr München (2006).
- [36] G. Jegert. *Modelling of leakage currents in high-k dielectrics*. Ph.D. thesis, Technischer Universität München (2011).
- [37] J. Bardeen. *Physical Review Letters*, **6** (1961) 57.
- [38] C. Cohen-Tannoudji. *Quantenmechanik*, vol. 2. Walter de Gruyter, 2nd edn. (1999).
- [39] E. Suzuki, D. K. Schroder, and Y. Hayashi. *Journal of Applied Physics*, **60** (1986) 3616.
- [40] M. Specht, M. Stadele, S. Jakschik, and U. Schroder. *Applied Physics Letters*, **84** (2004) 3076.
- [41] M. Fanciulli and G. Scarel (eds.). *Rare Earth Oxide Thin Films*. Springer (2007).
- [42] S.-W. Nam, J.-H. Yoo, H.-Y. Kim, S.-K. Kang, D.-H. Ko, C.-W. Yang, H.-J. Lee, M.-H. Cho, and J.-H. Ku. *Journal of Vacuum Science & Technology A*, **19** (2001) 1720.
- [43] M. Grube, D. Martin, W. M. Weber, T. Mikolajick, O. Bierwagen, L. Geelhaar, and H. Riechert. *Journal of Vacuum Science & Technology B*, **29** (2011) 01AC05.
- [44] M. Grube, D. Martin, W. Weber, T. Mikolajick, and H. Riechert. *Microelectronic Engineering*, **88** (2011) 1326 . Proceedings of the 17th Biennial International Insulating Films on Semiconductor Conference, 17th Biennial International Insulating Films on Semiconductor Conference.
- [45] A. Krause, W. M. Weber, U. Schroder, D. Pohl, B. Rellinghaus, J. Heitmann, and T. Mikolajick. *Applied Physics Letters*, **99** (2011) 222905.
- [46] M. Ritala and M. Leskala. *Handbook of Thin Film Materials*. Academic Press, San Diego (2001), 103 .
- [47] H. Park, M. Jo, H. Choi, M. Hasan, R. Choi, P. Kirsch, C. Y. Kang, B. H. Lee, T.-W. Kim, T. Lee, and H. Hwang. *Electron Device Letters, IEEE*, **29** (2008) 54 .
- [48] D. Martin, M. Grube, W. Weinreich, J. Müller, L. Wilde, E. Erben, W. M. Weber, J. Heitmann, U. Schröder, T. Mikolajick, and H. Riechert. *Journal of Vacuum Science & Technology B*, **29** (2011) 01AC02.

- [49] M. Grube, D. Martin, W. Weber, O. Bierwagen, L. Geelhaar, and H. Riechert. *Signals, Circuits and Systems (SCS), 2009 3rd International Conference on*, 1–5 (2009).
- [50] D. K. Schroder. *Semiconductor and Device Characterization*. John Wiley and Sons, Inc., New York, Chichester, Weinheim, Brisbane, Singapore, Toronto (1998).
- [51] C. Kittel. *Einführung in die Festkörperphysik*. Oldenbourg, München, 13th edn. (2002).
- [52] *Model 4200-SCS Semiconductor Characterization System, Reference Manual*.
- [53] *aixACCT TF 1000 Hysteresis Software Manual*.
- [54] M. Schumacher. *Relaxationsphänomene in keramischen Dünnschichten für zukünftige hochintegrierte Halbleiterspeicher*. Phd-thesis, RWTH-Aachen (1998).
- [55] G. Binnig, C. F. Quate, and C. Gerber. Physical Review Letters, **56** (1986) 930.
- [56] G. Binnig, H. Rohrer, C. Gerber, and E. Weibel. Physical Review Letters, **49** (1982) 57.
- [57] G. Binnig and H. Rohrer. Helvetica physica acta, **52** (1982) 726.
- [58] R. Young, J. Ward, and F. Scire. Review of Scientific Instruments, **43** (1972) 999 .
- [59] D. A. Kindlein. *Perovskitische Keramiken und dünne Filme: Untersuchungen mit oberflächenanalytischen Methoden*. Ph.D. thesis, Mathematisch-Naturwissenschaftliche-Technischen Fakultät (mathematisch-naturwissenschaftlicher Bereich) der Martin-Luther-Universität Halle Wittenberg (2005).
- [60] M. Porti, M. Nafria, X. Aymerich, A. Olbrich, and B. Ebersberger. Applied Physics Letters, **78** (2001) 4181.
- [61] A. Olbrich, B. Ebersberger, and C. Boit. Applied Physics Letters, **73** (1998) 3114.
- [62] S. Kremmer, H. Wurmbauer, C. Teichert, G. Tallarida, S. Spiga, C. Wiemer, and M. Fanciulli. Journal of Applied Physics, **97** (2005) 074315.
- [63] W. W. Mullins. Journal of Applied Physics, **28** (1957) 333.

- [64] Y.-R. Ma, C. Yu, Y.-D. Yao, Y. Liou, and S.-F. Lee. Physical Review B, **64** (2001) 195324.
- [65] D. Martin, M. Grube, W. M. Weber, J. Rüstig, O. Bierwagen, L. Geelhaar, and H. Riechert. Applied Physics Letters, **95** (2009) 142906.
- [66] A. Seko, T. Sago, M. Sakashita, A. Sakai, M. Ogawa, and S. Zaima. Japanese Journal of Applied Physics, **45** (2006) 2954.
- [67] M. N. Nikiforov, M. J. Brukman, and D. A. Bonnell. Applied Physics Letters, **93** (2008) 182101.
- [68] G. Bersuker, J. Yum, L. Vandelli, A. Padovani, L. Larcher, V. Iglesias, M. Porti, M. M. Nafria, K. McKenna, A. Shluger, P. Kirsch, and R. Jammy. Solid-State Electronics, **65-66** (2011) 146 . Selected Papers from the ESSDERC 2010 Conference.
- [69] D. Martin, M. Grube, P. Reinig, L. Oberbeck, J. Heitmann, W. M. Weber, T. Mikolajick, and H. Riechert. Applied Physics Letters, **98** (2011) 012901.
- [70] V. Mikhelashvili, G. Eisenstein, and A. Lahav. Applied Physics Letters, **90** (2007) 013506.
- [71] V. Mikhelashvili, A. Lahav, R. Brenner, and G. Eisenstein. Microelectronic Engineering, **85** (2008) 1545 .
- [72] M. Li, Z. Zhang, S. A. Campbell, W. L. Gladfelter, M. P. Agustin, D. O. Klenov, and S. Stemmer. Journal of Applied Physics, **98** (2005) 054506.
- [73] M. Liu, L. D. Zhang, G. He, X. J. Wang, and M. Fang. Journal of Applied Physics, **108** (2010) 024102.
- [74] V. V. Afanas'ev, A. Stesmans, F. Chen, and a. S. A. C. M. Li. Journal of Applied Physics, **95** (2004) 7936.
- [75] S. Rangan, E. Bersch, R. A. Bartynski, E. Garfunkel, and E. Vescovo. Physical Review B, **79** (2009) 075106.
- [76] G. Jegert. *Personal communications*.
- [77] *Gwyddion project website: <http://gwyddion.net>*.
- [78] J. McPherson, J.-Y. Kim, A. Shanware, and H. Mogul. Applied Physics Letters, **82** (2003) 2121.

- [79] K.-R. Yoon, K.-V. Im, J.-H. Yeo, E.-A. Chung, Y.-S. Kim, C.-Y. Yoo, S.-T. Kim, U.-I. Chung, , and J.-T. Moon. *Extended Abstracts of the 2005 International Conference on Solid State Devices and Materials, Kobe* (2005).
- [80] Y. Park, S. Lee, J. Lee, J. Lee, S. Han, E. Lee, S. Kim, J. Han, J. Sung, Y. Cho, J. Jun, D. Lee, K. Kim, D. Kim, S. Yang, B. Song, Y. Sung, H. Byun, W. Yang, K. Lee, S. Park, C. Hwang, T. Chung, and W. Lee. *VLSI Technology, 2007 IEEE Symposium on*, 190 –191 (2007).
- [81] D. Zhou, U. Schroeder, J. Xu, J. Heitmann, G. Jegert, W. Weinreich, M. Kerber, S. Knebel, E. Erben, and T. Mikolajick. *Journal of Applied Physics*, **108** (2010) 124104.
- [82] C. Zhao, O. Richard, H. Bender, M. Caymax, S. D. Gendt, M. Heyns, E. Young, G. Roebben, O. V. D. Biest, and S. Haukka. *Applied Physics Letters*, **80** (2002) 2374.
- [83] H. v. Wartenberg, H. Linde, and R. Jung. *Zeitschrift für anorganische und allgemeine Chemie*, **176** (1928) 349.
- [84] G. R. Fischer, L. J. Manfredo, R. N. McNally, and R. C. Doman. *Journal of Materials Science*, **16** (1981) 3447. 10.1007/BF00586307.
- [85] S. M. Lakiza and L. M. Lopato. *Journal of the American Ceramic Society*, **80** (1997) 893.
- [86] H. H. X. Yang, D. Dubiel and W. Riehemann. *Proc. 13th X-Ray Absorption Fine Structure XAFS13* (2006).
- [87] W. Weinreich, L. Wilde, P. Kücher, M. Lemberger, V. Yanev, M. Rommel, A. J. Bauer, E. Erben, J. Heitmann, U. Schröder, and L. Oberbeck. *Journal of Vacuum Science & Technology B*, **27** (2008) 364.
- [88] A. Paskaleva, M. Lemberger, A. J. Bauer, W. Weinreich, J. Heitmann, E. Erben, U. Schroder, and L. Oberbeck. *Journal of Applied Physics*, **106** (2009) 054107 .
- [89] R. Agaiyby, P. Hofmann, D. Zhou, M. Kerber, J. Heitmann, U. Schroeder, E. Erben, and L. Oberbeck. *Electron Device Letters, IEEE*, **30** (2009) 340 .
- [90] J. Pétry, W. Vandervorst, L. Pantisano, and R. Degraeve. *Microelectronics and Reliability*, **45** (2005) 815 . 13th Workshop on Dielectrics in Microelectronics.

- [91] L. Aguilera, M. Porti, M. Nafria, and X. Aymerich. Electron Device Letters, IEEE, **27** (2006) 157 .
- [92] G. Lucovsky, C. Fulton, Y. Zhang, Y. Zou, J. Luning, L. Edge, J. Whitten, R. Nemanich, H. Ade, D. Schlom, V. Afanase'v, A. Stesmans, S. Zollner, D. Triyoso, and B. Rogers. Device and Materials Reliability, IEEE Transactions on, **5** (2005) 65 .
- [93] G. Lucovsky, D. M. Fleetwood, S. Lee, H. Seo, R. D. Schrimpf, J. A. Felix, J. Lning, L. B. Fleming, M. Ulrich, and D. E. Aspnes. Nuclear Science, IEEE Transactions on, **53** (2006) 3644 .
- [94] S. Lombardo, J. H. Stathis, B. P. Linder, K. L. Pey, F. Palumbo, and C. H. Tung. Journal of Applied Physics, **98** (2005) 121301.
- [95] X. Li, C. H. Tung, and K. L. Pey. Applied Physics Letters, **93** (2008) 262902.
- [96] W. Weinreich, R. Reiche, M. Lemberger, G. Jegert, J. Müller, L. Wilde, S. Teichert, J. Heitmann, E. Erben, L. Oberbeck, U. Schröder, A. Bauer, and H. Ryssel. Microelectronic Engineering, **86** (2009) 1826 .
- [97] W. Weinreich, V. A. Ignatova, L. Wilde, S. Teichert, M. Lemberger, A. J. Bauer, R. Reiche, E. Erben, J. Heitmann, L. Oberbeck, and U. Schröder. Journal of Applied Physics, **106** (2009) 034107.
- [98] J. Müller, T. S. Böске, D. Bräuhäus, U. Schröder, U. Böttger, J. Sundqvist, P. Kücher, T. Mikolajick, and L. Frey. Applied Physics Letters, **99** (2011) 112901.
- [99] J. Müller, T. S. Böске, U. Schröder, S. Müller, D. Bräuhäus, U. Böttger, L. Frey, and T. Mikolajick. submitted to Nanoletters, (2012).
- [100] D. Martin, M. Grube, W. Weinreich, J. Muller, W. M. Weber, U. Schroder, H. Riechert, and T. Mikolajick. Journal of Applied Physics, **113** (2013) 194103.
- [101] M. Celina, K. Gillen, and R. Assink. Polymer Degradation and Stability, **90** (2005) 395 .
- [102] C.-H. Yang, J. Seidel, S. Y. Kim, P. B. Rossen, P. Yu, M. Gajek, Y. H. Chu, L. W. Martin, M. B. Holcomb, Q. He, P. Maksymovych, N. Balke, S. V. Kalinin, A. P. Baddorf, S. R. Basu, M. L. Scullin, and R. Ramesh. Nature Mater, **8** (2009) 485.
- [103] G. Jegert, A. Kersch, W. Weinreich, U. Schröder, and P. Lugli. Applied Physics Letters, **96** (2010) 062113.

- [104] G. Jegert, D. Popescu, P. Lugli, M. J. Häufel, W. Weinreich, and A. Kersch. *Physical Review B*, **85** (2012) 045303.
- [105] T. S. Böske, J. Müller, D. Bräuhäus, U. Schröder, and U. Böttger. *Applied Physics Letters*, **99** (2011) 102903.
- [106] J. Muller, U. Schroder, T. S. Boscke, I. Muller, U. Bottger, L. Wilde, J. Sundqvist, M. Lemberger, P. Kucher, T. Mikolajick, and L. Frey. *Journal of Applied Physics*, **110** (2011) 114113.
- [107] D. Martin, A. Heinzig, M. Grube, L. Geelhaar, T. Mikolajick, H. Riechert, and W. M. Weber. *Physical Review Letters*, **107** (2011) 216807.
- [108] M. Diarra, Y.-M. Niquet, C. Delerue, and G. Allan. *Physical Review B*, **75** (2007) 045301.
- [109] J. K. H. R. M. Björk, H. Schmid and W. Riess. *Nature Nanotechnology*, **4** (2009) 103.
- [110] Y. Nishi (1970).
- [111] M. P. Lepselter and S. M. Sze. *Proceedings of the IEEE*, **56** (8) 1400.
- [112] S. J. Tans, A. R. M. Verschueren, and C. Dekker. *Nature*, **393** (1998) 49.
- [113] J. Appenzeller, M. Radosavljević, J. Knoch, and P. Avouris. *Physical Review Letters*, **92** (2004) 048301.
- [114] X. Wang, Y. Ouyang, X. Li, H. Wang, J. Guo, and H. Dai. *Physical Review Letters*, **100** (2008) 206803.
- [115] Y. Cui, X. Duan, J. Hu, and C. M. Lieber. *The Journal of Physical Chemistry B*, **104** (2000) 5213.
- [116] J. M. Larson and J. P. Snyder. *IEEE Transactions on Electron Devices*, **53** (2006) 1048.
- [117] J. Kedzierski, P. Xuan, E. H. Anderson, J. Bokor, T.-J. King, and C. Hu. *IEDM Technical Digest International Electron Devices Meeting*, (2000) 57.
- [118] F. m. c. Léonard and A. A. Talin. *Physical Review Letters*, **97** (2006) 026804.
- [119] F. m. c. Léonard, A. A. Talin, B. S. Swartzentruber, and S. T. Picraux. *Physical Review Letters*, **102** (2009) 106805.

- [120] J. Knoch and J. Appenzeller. Applied Physics Letters, **81** (2002) 3082.
- [121] W. M. Weber, L. Geelhaar, F. Kreupl, H. Riechert, L. Lamagna, M. Fanciulli, G. Scarpa, and P. Lugli. NANO '08 8th IEEE Conference on Nanotechnology,, **244** (2008) 580.
- [122] H. Yan, H. S. Choe, S. W. Nam, Y. Hu, S. Das, J. F. Klemic, J. C. Ellenbogen, and C. M. Lieber. Nature, **470** (2011) 240.
- [123] S. Zhang, H. Wei, K. Bao, U. Håkanson, N. J. Halas, P. Nordlander, and H. Xu. Physical Review Letters, **107** (2011) 096801.
- [124] H. Wei, Z. Li, X. Tian, Z. Wang, F. Cong, N. Liu, S. Zhang, P. Nordlander, N. J. Halas, and H. Xu. Nano Letters, **11** (2011) 471.
- [125] J. Hu, Y. Liu, C. Z. Ning, R. Dutton, and S.-M. Kang. Applied Physics Letters, **92** (2008) 083503.
- [126] M. Freitag, M. Radosavljevic, Y. Zhou, A. T. Johnson, and W. F. Smith. Applied Physics Letters, **79** (2001) 3326.
- [127] B. Tian, P. Xie, T. J. Kempa, D. C. Bell, and C. M. Lieber. Nature Nanotechnology, **4** (2009) 824.
- [128] M. S. Gudiksen, L. J. Lauhon, J. Wang, D. C. Smith, and C. M. Lieber. Nature, **415** (2002) 617.
- [129] Y. Wu, J. Xiang, C. Yang, W. Lu, and C. M. Lieber. Nature, **430** (2004) 61.
- [130] R. S. Wagner and W. C. Ellis. Applied Physics Letters, **4** (1964) 89.
- [131] W. M. Weber, L. Geelhaar, A. P. Graham, E. Unger, G. S. Duesberg, M. Liebau, W. Pamler, C. Cheze, H. Riechert, P. Lugli, and F. Kreupl. Nano Letters, **6** (2006) 2660. PMID: 17163684.
- [132] K.-C. Lu, W.-W. Wu, H.-W. Wu, C. M. Tanner, J. P. Chang, L. J. Chen, and K. N. Tu. Nano Letters, **7** (2007) 2389.
- [133] J. Knoch, M. Zhang, J. Appenzeller, and S. Mantl. Applied Physics A: Materials Science & Processing, **87** (2007) 351.
- [134] K.-I. Chen, B.-R. Li, and Y.-T. Chen. Nano Today, **6** (2011) 131 .
- [135] A. Krause, W. Weber, A. Jahn, K. Richter, D. Pohl, B. Rellinghaus, U. Schröder, J. Heitmann, and T. Mikolajick. Journal of Vacuum Science & Technology B, **29** (2011) 01AC07.

- [136] N. Menou, X. Wang, B. Kaczer, W. Polspoel, M. Popovici, K. Opsomer, M. Pawlak, W. Knaepen, C. Detavernier, T. Blomberg, D. Pierreux, J. Swerts, J. Maes, P. Favia, H. Bender, B. Brijs, W. Vandervorst, S. Van Elshocht, D. Wouters, S. Biesemans, and J. Kittl. *Electron Devices Meeting, 2008. IEDM 2008. IEEE International*, 1–4 (2008).
- [137] S. Riedel, J. Neidhardt, S. Jansen, L. Wilde, J. Sundqvist, E. Erben, S. Teichert, and A. Michaelis. *Journal of Applied Physics*, **109** (2011) 094101.
- [138] R. Waser and M. Aonu. *Nature Materials*, **6** (2007) 833.
- [139] H. Mähne, L. Berger, D. Martin, V. Klemm, S. Slesazeck, S. Jakschik, D. Rafaja, and T. Mikolajick. *Solid-State Electronics*, **72** (2012) 73 .
- [140] S. Mueller, J. Mueller, A. Singh, S. Riedel, J. Sundqvist, U. Schroeder, and T. Mikolajick. *Advanced Functional Materials*, (2012) DOI: 10.1002/adfm.201103119.
- [141] D. Martin, E. Yurchuk, S. Müller, J. Müller, J. Paul, J. Sundquist, S. Slesazeck, T. Schloesser, R. van Bentum, M. Trentzsch, U. Schroeder, and T. Mikojaick. *Proc. Ultimate Integration on Silicon 2012 ,Grenoble*, DOI: 10.1109/ULIS.2012.6193391 (2012).
- [142] J. Müller, E. Yurchuk, T. Schlösser, J. Paul, R. Hoffmann, S. Muller, D. Martin, S. Slesazeck, P. Polakowski, J. Sundqvist, M. Czernohorsky, K. Seidel, P. Kücher, R. Boschke, M. Trentzsch, K. Gebauer, U. Schroeder, and T. Mikolajick. *VLSI Technology, 2012 IEEE Symposium on*. IEEE (2012).
- [143] E. Yurchuk, J. Müller, R. Hoffmann, J. Paul, D. Martin, R. Boschke, T. Schlösser, S. Müller, S. Slesazeck, R. van Bentum, M. Trentzsch, U. Schroeder, and T. Mikolajick. *Proc. IEEE 4th International Memory Workshop 2012* (2012).
- [144] D. Martin, E. Yurchuk, S. Müller, J. Müller, J. Paul, J. Sundquist, S. Slesazeck, T. Schloesser, R. van Bentum, M. Trentzsch, U. Schroeder, and T. Mikojaick. submitted to *Solid State Electronics*, (2012).

Table of Acronyms

3D	Three dimensional
AC	Alternating current
BC	Bit line capacitance
BE	Bottom electrode
CB	Conduction band
CET	Capacitance equivalent thickness
CVD	Chemical vapor deposition
CVU	Capacitance voltage unit
DC	Direct current
DT	Deep-trench
DUT	Device under test
EELS	Electron energy loss spectroscopy
EFTEM	Energy filtered transmission electron microscopy
El. aff.	Electron affinity
FIB	Focused ion beam
GI-XRD	Grazing incidence X-ray diffraction
HV	High vacuum
ITRS	International technology roadmap for semiconductors
MBE	Molecular beam epitaxy
MIM	Metal-insulator-metal
MIS	Metal-insulator-semiconductor
MOSFET	Metal oxide field effect transistor
namlab	Nanoelectronic Materials Laboratory
PDA	Post deposition annealing
PVD	Physical vapor deposition
RMS	Raw mean square
RTA	Rapid thermal annealing
SC	Storage capacitor
SEM	Scanning electron microscope
SILC	Stress induced leakage currents
SiNWSBFET ...	Silicon nanowire Schottky barrier field effect transistor
SMU	Source measure unit
SPM	Scanning probe microscope
STM	Scanning tunneling microscope
TE	Top electrode
TEM	Transmission electron microscope

TEMAZ	Tetrakis[ethylmethlamino]zirconium
UHV	Ultra high vacuum
WKB	Wigner-Kramers-Brillouin
XPS	X-ray photoelectron spectroscopy
XRD	X-ray diffraction
XRR	X-ray reflectivity

List of Publications

Journal Articles:

Local charge transport in nanoscale amorphous and crystalline regions of high-k $(\text{ZrO}_2)_{0.8}(\text{Al}_2\text{O}_3)_{0.2}$ thin films

D. Martin, M. Grube, W. M. Weber, J. Rüstig, O. Bierwagen, L. Geelhaar and H. Riechert, Applied Physics Letters, **95** 142906 (2009).

Investigation of zirconium oxide based high-k dielectrics for future memory applications

M. Grube, D. Martin, W. M. Weber, O. Bierwagen, L. Geelhaar and H. Riechert, Proc. IEEE 2009 3rd International Conference on Signals, Circuits and Systems(SCS), (2009).

Influence of composition and bottom electrode properties on the local conductivity of TiN/HfTiO₂ and TiN/Ru/HfTiO₂ stacks

D. Martin, M. Grube, P. Reinig, L. Oberbeck, J. Heitmann, W. M. Weber, T. Mikolajick and H. Riechert, Applied Physics Letters, **98** 012901 (2011).

Macroscopic and microscopic electrical characterizations of high-k ZrO_2 and $\text{ZrO}_2/\text{Al}_2\text{O}_3/\text{ZrO}_2$ metal-insulator-metal structures

D. Martin, M. Grube, W. Weinreich, J. Müller, L. Wilde, E. Erben, W. M. Weber, J. Heitmann, U. Schröder, T. Mikolajick and H. Riechert, Journal of Vacuum Science and Technology B, **29** 01AC02 (2011).

Applicability of molecular beam deposition for the growth of high-k oxides

M. Grube, D. Martin, W. M. Weber, T. Mikolajick, O. Bierwagen, L. Geelhaar, and H. Riechert, Journal of Vac. Sci. and Technol., **29** 01AC05 (2011).

Phase stabilization of sputtered strontium zirconate

M. Grube, D. Martin, W. M. Weber, T. Mikolajick, and H. Riechert, Microelectronic Engineering **88** 1326 (2011).

Direct probing of Schottky Barriers in Si Nanowire Schottky Barrier Field Effect Transistors

D. Martin, A. Heinzig, M. Grube, L. Geelhaar, T. Mikolajick, H. Riechert,

and Walter M. Weber, Physical Review Letters **107** 216807 (2011).

Filamentary resistive switching in amorphous and polycrystalline Nb₂O₅ thin films

H. Mähne, L. Berger, D. Martin, V. Klemm, S. Slesazeck, S. Jakschik, D. Rafaja and T. Mikolajick Solid State Electronics **72** 73 (2012).

Mesoscopic analysis of leakage current suppression in ZrO₂/Al₂O₃/ZrO₂ nano-laminates

D. Martin, M. Grube, W. Weinreich, J. Müller, W. M. Weber, U. Schröder, H. Riechert, and T. Mikolajick, accepted by Journal of Applied Physics **113** 194103 (2013).

Conference Contributions:

MBD of high-k dielectrics for DRAM application L. Geelhaar, O. Bierwagen, M. Grube, D. Martin, H. Riechert Deutscher MBE-Workshop in Jülich, Germany 2007.

Leakage spot evolution in thin (ZrO₂)_{0.8}(Al₂O₃)_{0.2} -films observed by conductive atomic force microscopy (CAFM) D. Martin, O. Bierwagen, M. Grube, L. Geelhaar, H. Riechert DPG Spring Meeting in Berlin, Germany 2008.

Investigation of (SrO)_x(ZrO₂)_(1-x) high-k dielectrics deposited by molecular beam deposition M. Grube, O. Bierwagen, D. Martin, L. Geelhaar, H. Riechert DPG Spring Meeting in Berlin, Germany 2008.

ZrO₂ and (SrO)_x(ZrO₂)_(1-x) thin films deposited by MBD for use in metal insulator metal capacitors M. Grube, O. Bierwagen, D. Martin, L. Geelhaar, H. Riechert MRS Spring Meeting in San Francisco, USA 2008.

CAFM studies of leakage spot evolution in thin (ZrO₂)_{0.8}(Al₂O₃)_{0.2} -films D. Martin, O. Bierwagen, M. Grube, L. Geelhaar, H. Riechert MRS Spring Meeting in San Francisco, USA 2008.

Growth and characterization of (SrO)_x(ZrO₂)_(1-x) thin films as high-k dielectric for memory application M. Grube, O. Bierwagen, D. Martin, L. Geelhaar, H. Riechert Workshop of dielectrics in microelectronics in Bad Saarow, Germany 2008.

Conductive atomic force microscopy studies of leakage spot evolution in thin

(ZrO₂)_{0.8}(Al₂O₃)_{0.2}-films D. Martin, O. Bierwagen, M. Grube, L. Geelhaar, H. Riechert in Bad Saarow, Germany 2008.

Molecular growth of extremely thin dielectric BaHfO₃ films on TiN G. Lippert, J. Dabrowski, G. Lupina, G. Kozlowski, G. Weidner, P. Zaumseil, D. Martin, L. Oberbeck, U. Schroeder and H.-J. Muessig MBE in Vancouver, Canada 2008.

Characterization of (SrO)_x(ZrO₂)_(1-x) thin films for use in metal insulator metal capacitors M. Grube, O. Bierwagen, D. Martin, L. Geelhaar, H. Riechert DPG Spring Meeting Dresden, Germany 2009.

Conductive atomic force microscopy studies of leakage spot evolution in thin (ZrO₂)_{0.8}(Al₂O₃)_{0.2}-films D. Martin, O. Bierwagen, M. Grube, L. Geelhaar, H. Riechert DPG Spring Meeting in Dresden, Germany 2009.

Direct comparison of the local conductance at crystallites in (ZrO₂)_{0.8}(Al₂O₃)_{0.2} high-k films observed by conductive atomic force microscopy D. Martin, M. Grube, O. Bierwagen, W. M. Weber, L. Geelhaar, and H. Riechert EMRS Spring Meeting in Strasbourg, France 2009.

Growth and, physical and electrical investigation of (SrO)_x(ZrO₂)_(1-x) as high-k dielectric for future memory application M. Grube, D. Martin, O. Bierwagen, W. M. Weber, L. Geelhaar, and H. Riechert EMRS Spring Meeting, Strasbourg in France 2009.

Influence of composition and bottom electrodes on the local conduction of amorphous (HfO₂)_{1-x}(TiO₂)_x and nanocrystalline (ZrO₂)_{0.8}(Al₂O₃)_{0.2} investigated by conductive atomic force microscopy D. Martin, M. Grube, W. M. Weber, P. Reinig, L. Geelhaar, and H. Riechert 16. Intl. Workshop on Oxide Electronics in Tarragona, Spain 2009.

Molecular beam deposition of Sr_xZr_(1-x)O_y as a potential high-k dielectric for future metal-insulator-metal capacitor applications M. Grube, D. Martin, W. Weber, L. Geelhaar, H. Riechert 16. Intl. Workshop on Oxide Electronics in Tarragona, Spain 2009.

Investigation of Zirconium Oxide Based High-k Dielectrics for Future Memory Applications D. Martin, M. Grube, W. M. Weber, O. Bierwagen, L. Geelhaar, H. Riechert IEEE 2009 3rd International Conference on Signals, Circuits and Systems(SCS) in Djerba, Tunisia 2009.

A comparison of Sr_xZr_(1-x)O_y and ZrO₂ as potential high-k dielectric for future

memory applications M. Grube, D. Martin, W. M. Weber, T. Mikolajick, L. Geelhaar and H. Riechert, DPG Spring Meeting in Regensburg, Germany 2010.

Nanoscale analysis of the electric properties of ultra thin ZrO_2 -, $(\text{ZrO}_2)_{0.8}(\text{Al}_2\text{O}_3)_{0.2}$ -ZAZ-films D. Martin, M. Grube, E. Erben, W. Weinreich, U. Schroeder, L. Geelhaar, W. M. Weber, H. Riechert, and T. Mikolajick, DPG Spring Meeting in Regensburg, Germany 2010.

Macroscopic and microscopic electrical characterization of high-k ZrO_2 and $\text{ZrO}_2/\text{Al}_2\text{O}_3/\text{ZrO}_2$ metal insulator-metal structures D. Martin, M. Grube, W. Weinreich, J. Müller, L. Wilde, E. Erben, W. M. Weber, U. Schroeder, T. Mikolajick, and H. Riechert, Workshop of dielectrics in microelectronics in Bratislava, Slovakia 2010.

Improvement of dielectric properties of $\text{Sr}_x\text{Zr}_{(1-x)}\text{O}_y$ grown by Molecular Beam Deposition and Sputtering M. Grube, D. Martin, W. M. Weber, T. Mikolajick, L. Geelhaar and H. Riechert, Workshop of dielectrics in microelectronics in Bratislava, Slovakia 2010.

Local I-V characteristics of high-k ultra-thin ZrO_2 and $\text{ZrO}_2/\text{Al}_2\text{O}_3/\text{ZrO}_2$ -films D. Martin, M. Grube, E. Erben, J. Müller, W. Weinreich, U. Schröder, L. Geelhaar, W. M. Weber, T. Mikolajick, and H. Riechert DPG Spring Meeting 2011 in Dresden, Germany 2011.

Improvement of dielectric properties of $\text{Sr}_x\text{Zr}_{(1-x)}\text{O}_y$ -grown by Molecular Beam Deposition and Sputtering M. Grube, D. Martin, W. M. Weber, T. Mikolajick, L. Geelhaar and H. Riechert, DPG Spring Meeting in Dresden, Germany 2011.

Direct Imaging of Nanowire Schottky Junctions by Scanning Gate Microscopy D. Martin, A. Heinzig, M. Grube, W. M. Weber, L. Geelhaar, T. Mikolajick, and H. Riechert, MRS Spring Meeting in San Francisco, USA 2011.

Reconfigurable Nanowire Electronics W. M. Weber, A. Heinzig, D. Martin, S. Slesazeck, and T. Mikolajick, ECS Meeting, Montreal, Canada 2011

Phase stabilization of sputtered strontion zirconate, M. Grube, D. Martin, W. M. Weber, T. Mikolajick, and H. Riechert, INFOS2011 in Grenoble, France 2011.

Spatially Resolved Studies of Leakage Currents in High-k Dielectric Thin-Films for DRAM Application, D. Martin, M. Grube, W. M. Weber, W. Weinreich, J. Müller, H. Riechert, and T. Mikolajick, NanoZeit SEMICON Europa in Dresden Germany 2012.

Adoption of amorphous and crystalline Nb₂O₅ for scaled resistive switching devices H. Mähne, L. Berger, D. Martin, V. Klemm, S. Slesazeck, D. Rafaja, and T. Mikolajick, EMRS Spring Meeting in Strasbourg, France 2012.

Acknowledgement

My deep gratitude goes to everybody who supported my work on this thesis. In particular my advisors Prof. Dr. Henning Riechert, Prof. Dr. Thomas Mikolajick, Dr. Lutz Geelhaar and Dr. Walter M. Weber for their support, patience, encouragement and occasional challenges in the course of this project. A special thanks goes to Dr. Jürgen Rüstig and Dr. Karlheinz Horninger for taking a strong position and keeping up on their promises, even under great personal risk, to keep the Nanoelectronic Materials Laboratory (namlab) going. I am also grateful to Prof. Dr. Recardo Manzke and Prof. Dr. Saskia F. Fischer for agreeing to review this thesis.

Additional gratitude goes to Dr. Uwe Schröder for fruitful discussions and for sharing his substantial knowledge about ZrO_2 MIM capacitors. For the thorough introduction to CAFM Dr. Oliver Bierwagen is thankfully acknowledged. My deep professional and personal gratitude also goes to my colleagues and friends, Dr. Caroline Cheze, Dipl.-Phys. Matthias Grube, Dipl.-Ing.(FH) Heiko Sambale, Danielle Schönfeld, Petra Böhme, Terry Jay, Ulrike Meier, Dipl.-Ing. Andre Heinzig, Dipl.-Phys. Andreas Krause and Dipl.-Nat. Guntrade Roll, who always gave work in the lab a feeling of pleasure and sense even in the most hopeless of times. Their honest devotion, competence and reliability were a valuable contribution to this work and to my personal well-being.

Vivien Voßebürger is thankfully acknowledged for sharing her insights and profound knowledge of TEM and for TEM image acquisition.

Dipl.-Phys. Gunther Jegert is thankfully acknowledged for the simulation of electric fields in dielectrics on various electrodes and Dr. Jesper Wittborn for access to the AFM facilities at Infineon Munich.

I am grateful to Dr. Lars Oberbeck and Dr. Peter Reinig for fruitful discussions and for providing HfTiO_2 samples.

Dr. Lutz Hillmann and Dr. Lutz Wilde are acknowledged for TEM and X-ray analysis.

My deep gratitude also goes to Dipl.-Nat. Wenke Weinreich and Dipl.-Nat. Johannes Müller for the deposition of ZrO_2 by ALD.

Additionally, I feel deeply indebted to all my colleagues at namlab and Qimonda for valuable advice and assistance. I feel deeply indebted to my parents Ursula Martin and Dr. Jochen Martin for their patient and ongoing support. Last but not least my deep personal gratitude goes to StRef. Dorothea Hesenmöller for love, companionship, emotional support and a lot of patience.

Selbständigkeitserklärung

Hiermit erkläre ich, die vorliegende Arbeit „Spatially resolved Studies of the Leakage Current Behavior of Oxide Thin-films“ selbständig und nur unter Verwendung der gemäß §6 Absatz (3) angegebenen Hilfen und Hilfsmittel angefertigt zu haben.

Ich habe mich an keiner anderen Universität um einen Doktorgrad beworben und besitze auch keinen entsprechenden Doktorgrad.

Ich erkläre die Kenntnis der dem Verfahren zugrunde liegenden Promotionsordnung der Mathematisch-Naturwissenschaftlichen Fakultät I der Humboldt-Universität zu Berlin.

Dresden, den 12. Juni 2012

Christian Dominik Martin